INTERACTIONS OF SELF-TRAPPED BEAMS GENERATED WITH A MINIATURE GREEN LASER IN A PHOTOPOLYMERIZABLE MEDIUM

INTERACTIONS OF SELF-TRAPPED BEAMS GENERATED WITH A MINIATURE GREEN LASER IN A PHOTOPOLYMERIZABLE MEDIUM

By

TONG WANG, B.E.

A Thesis

Submitted to the School of Graduate Studies

In Partial Fulfillment of the Requirements

for the Degree

Master of Applied Science

McMaster University

Master of Applied Science (2012) McMaster University

(Engineering Physics) Hamilton, Ontario

TITLE: Interactions of Self-Trapped Beams Generated with a Miniature Green Laser in a Photopolymerizable Medium

AUTHOR: Tong Wang

B.E. (Southeast University)

Supervisor: Dr. Chang-qing Xu

Dr. Kalaichelvi Saravanamutuu

NUMBER OF PAGES: xii, 113

ABSTRACT

This study examined the self-trapping of light emitted by a miniature green laser in a photopolymerizable medium and the interactions between two parallel-propagating self-trapped beams. The work included the design and fabrication of an Intra-Cavity Frequency-Doubling (IC-FD) Nd: YVO_4/MgO: PPLN miniature green laser with a stable and tunable output intensity. Emission from this laser enabled a systematic examination of self-trapping phenomena at incident intensities spanning 8 orders of magnitude (3.2×10^{-5} W cm^{-2} to 6368 W cm^{-2}). When launched into a photopolymerizable medium, light emitted by the miniature green laser self-trapped by initiating polymerization and corresponding changes in refractive index along its propagation path. The evolution and dynamics of the self-trapped beam corresponded to the behaviour of self-trapped beams of coherent light. Interactions between a pair of parallel-propagating self-trapped beams were also characterised at a range of intensities. This study shows that the miniature green laser is an efficient, coherent source with a large range of output intensities for the excitation of self-trapped beams. This opens opportunities for its incorporation into small-scale optical systems designed to operate based on the generation and interactions of self-trapped beams.

Acknowledgement

I would like to express my gratitude to my supervisors, Dr. Chang-Qing Xu and Dr. Kalaichelvi Saravanamuttu, for their guidance and support throughout the course of my graduate studies. They are both always accessible and willing to help with my research.

I would also like to thank my defense committee member, Dr. Andrew P Knights, for his valuable suggestions.

I thank Dr. Xu's group members: Dr. Yang Lu, Dr. Qingyang Xu, Jian Sun, Yi Gan, Tianyi Guo for their expertise and guidance in photonic devices. We had innumerable discussion within the group that helped me to design and fabricate the green laser that is required for the experiments. Many thanks to Dr. Saravanamuttu's group as well: Dr. Ian D. Hosein, Dr. Liqun Qiu, Mattew Ponte, Chris Gendy, Alex Hudson and Kumar Dinesh, for their advice on the optical assembly and nonlinear experiments. Having two research groups made my graduate studies not only efficient but also interesting.

Finally I thank all my friends from Hamilton, my family from China, for their constant prayer and support.

Table of Contents

List of Figures

List of Tables

Chapter 1 INTRODUCTION

The laser (light amplification by stimulated emission of radiation) industry has been developing rapidly since the invention of the first Ruby laser in 1960 (1). Over the past half century, lasers have become ubiquitous utilities in thousands of highly varied applications due to their large range of power levels, wavelengths, and operation modes.

Self-action phenomena take place when optical beams propagate in a nonlinear medium. Various types of self-action can be induced by high intensity laser beams in different types of media, such as Kerr media, saturable media, photorefractive media, and quadratic media. There are different mechanisms for different types of media, and the discovery of dynamics and effects of nonlinear propagation can be made both theoretically and experimentally.

Among various types of nonlinear media, photopolymer has a different nonlinear mechanism from other materials since the nonlinear propagation of the light is induced by the refractive index change that is caused by the permanent photochemical reactions. By employing the miniaturized green laser, a systematic study has been performed on the self-action phenomena including the evolution of the refractive index change, the excitation of the high order modes and the

filamentation of the beams. Thanks to the small size of the Intra-cavity Frequency-doubling (IC-FD) green laser, preliminary studies on the interactions of two parallel coherent beams were conducted with a simple design of optical set-up.

Some unique features of the Intra-Cavity Frequency-Doubling Neodymium doped Yttrium Orthovanadate/Magnesium Oxide doped Periodically Poled Lithium Niobate (IC-FD Nd: YVO_4/MgO: PPLN) green laser include the high-range of output intensity, stability of the output power, high efficiency in the operating range, small size and low cost. The tunability and stability of the output intensity enables the systematic study of the self-action in the medium of photopolymer over a broad range of the beam intensities over eight orders of magnitude. The miniaturized green laser simplifies the design of the optical set up, especially for the two-beam interaction experiments, by eliminating unnecessary optical components. Its small size also makes possible the application of "self-guided" light along the high refractive-index region as a self-written waveguide forms as the beam travels through the medium. In addition, the low cost to manufacture and maintain the IC-FD Nd: YVO_4/MgO: PPLN laser further reduces the overall cost of the experiments, making a significant contribution to the current and future study of the nonlinear phenomena within different types of media.

This thesis focuses on the design and fabrication of a miniaturized IC-FD green laser. By employing this laser, the experimental study of self-trapping light within photopolymerizable organosiloxane was conducted. In this chapter, a review

of different approaches to generate green light, a comprehensive comparison of these technologies, and a review of optical nonlinearity in various materials will be presented.

1.1 Different Types of Green Lasers

1.1.1 GaN Green Laser Diodes

Since the 1960s, there has been significant study and research toward semiconductor laser materials (2, 3). A promising material, GaN/AlN/InN is a wide band gap semiconductor material system, which covers a wide wavelength range (200 nm-650 nm). GaN is used to make blue laser diodes. In 1992 it was reported that by increasing the indium content of the InGaN, it was possible to prepare green laser diodes (4). However, there are some major challenges in fabricating green laser diodes, such as the choice of substrate. Researchers have been using GaN single crystal, though it is challenging to grow high-quality single crystal GaN since slight lattice mismatch can induce misfit dislocations at the interface. GaN crystals can also develop cracks and ultimately degrade the performance of the devices. Another major challenge is material growth. In order to have green laser emission, increased indium content is required in the InGaN quantum well. However, the material growth is challenging with the method of Metal Organic Chemical Vapor Deposition (MOCVD) (4-8).

Recent publications show the rapid development of green laser diodes (LD). In 2012 Sony and Sumitomo introduced the world's first green laser diode capable of delivering over 100mW power at 530nm (9). Sony and Sumitomo have an extremely high standard of semiconductor processing technique. The LD was grown by the MOCVD method with a complicated design which has an n-type GaN layer grown on the GaN substrate. On top of this layer, there's an n-type InAlGaN cladding layer, an n-type InGaN waveguide layer, an InGaN multiple QW active region, a p-type InGaN waveguide layer, a p-type InGaN cladding layer and a p-type GaN contact layer. The InGaN QW has a thickness of less than 3 nm, and the ridge waveguide has a width of 2 μm, which was fabricated with the techniques of dry etching and photolithography. With this design, 100 mW of output power was achieved with a wavelength at 530 nm and wall plug efficiency of 7.0 - 8.9%.

1.1.2 Green Lasers by Means of Frequency Doubling

1.1.2.1 Solid State Laser

Semiconductor laser materials can not generate light falls into the range of green. However, an indirect way was introduced by using the nonlinear optical technology. In 1961, Franken first reported the observation of the nonlinear optical phenomenon with crystalline quartz (10). There are two main ways of converting frequency by means of frequency doubling: by insertion of the nonlinear optical

crystal into the laser cavity or by isolation of the frequency doubling crystal outside of the cavity. Due to the low optical frequency conversion efficiency resulting from the second or higher order nonlinear effect, the intra-cavity design is more efficient as compared to the method of extra-cavity frequency conversion (11, 12).

An infrared laser emitting light at a wavelength of 1064 nm is required to generate green light by means of either the intra-cavity frequency doubling or the single pass frequency doubling. The common crystals used for frequency doubling are $KTiOPO_4$(KTP), LiB_3O_5(LBO) and periodically poled lithium niobate (PPLN), which convert the 1064-nm output from Nd:YAG or Nd:YVO_4 laser crystals. (13-18)

	MgO:PPLN	KTP	LBO
Phase-matching type	QPM e+e→e	XY plane, $\theta=90^0$, $\phi=23.5^0$ o+e→e(type II)	XY plane, $\theta=90^0$, $\phi=11.4^0$ o+o→e (type I)
Effective nonlinear coefficient	16-22 pm/V	3.2 pm/V	0.96 pm/V
Photorefractive damage threshold	>2 MW/cm^2	Not clear	No
Optical absorption	0.004 cm^{-1}@1064 0.02 cm^{-1}@532	<0.006 cm^{-1}@1064 <0.02@532	0.0035 cm^{-1}
Thermal conductivity	4.6 W/m/K	3 W/m/K	3.5 W/m/K
Temperature tolerance	2.1 °C/cm	25 °C/cm	6.2 °C/cm
Transparency wavelength range	0.34~4.5 μm	0.35~4.5 μm	0.155~3.2 μm
phase matching range	Full transparent range	0.994~3.4 μm	0.551 ~ 3.23 μm
Walk-off angle	No	4.5	7
Green induced infrared absorption	Yes	Yes	No
Output Polarization	High	Change with T	High

Table 1.1Specifications of widely used nonlinear optical crystals. (23)

Thanks to the progress made in fabricating the periodically poled lithium niobate (PPLN), a 12W green light solid-state laser was achieved with an Nd: YVO_4 planar waveguide laser array intra-cavity frequency doubled by MgO doped PPLN (19). A 6W green light was also obtained with a 20W fiber pigtailed pump LD module (20), and a 1.5W green laser with bulk intra cavity frequency doubled Nd: YVO_4/MgO: PPLN crystals pumped by a 3W 808-nm LD (21).

1.1.2.2 Edge Emitting Semiconductor Lasers with Single-Pass FD

High power semiconductor lasers and high efficiency nonlinear crystals are required in order to attain high efficiency single-pass frequency doubling green lasers, with either bulk crystals or waveguide nonlinear optical crystals. The single-pass frequency doubling technology makes blue-green laser light (450 nm to 550 nm) converting from lower frequency light generated by the high power InGaAs/GaAs laser (900 nm to 1100 nm) (22). Fig 1.1 displays an experimental configuration showing a single-pass frequency doubled green laser with a Distributed Bragg Reflector Laser Diode (DBR-LD) amplified by a taper section, frequency doubled by a bulk PPLN as nonlinear crystal.

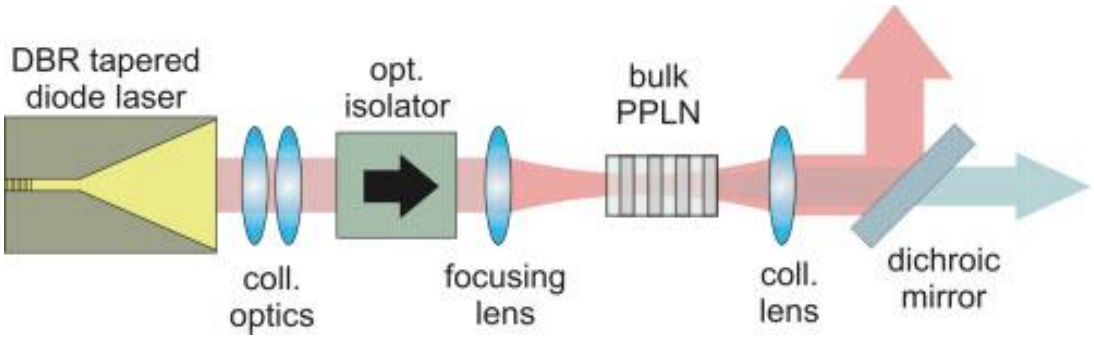

Figure 1.1 Single-pass frequency doubling of DBR/MOPA with a bulk PPLN crystal (22). Reproduced with permission.

In recent years there has been great development in single pass frequency doubling edge emitted semiconductor lasers by MgO-doped PPLN (24, 25). More than 1.5 W of green light at 531 nm is generated by single pass second harmonic generation (SHG) in periodically poled MgO: $LiNbO_3$ with the conversion efficiency over 18.5% by the Distributed Feedback/Master-Oscillator-Power-Amplifier (DFB/MOPA) technology (24). Corning Inc. reported 304 mW green light emission generated by frequency doubling (FD) by using a 1060 nm DBR semiconductor laser as the pump and MgO-doped PPLN waveguide in a single-pass configuration corresponding to a conversion efficiency of 72.9% in the waveguide (26).

However, single-pass frequency doubling semiconductor lasers suffer from design difficulties: lowing coupling efficiency from the semiconductor lasers to the nonlinear crystal, relatively big nonlinear crystals, mechanical instability, and narrow temperature tolerance.

1.1.2.3 Vertical Extended Cavity Semiconductor Emitting Laser (VECSEL)

The semiconductor laser technology, optically pumped semiconductor vertical external cavity surface-emitting lasers (OPS-VECSEL) is a growing technology to generate green light (27-31).

OPS-VECSEL combines the approaches of diode-pumped solid-state lasers, and semiconductor quantum-well (QW) vertical-cavity surface-emitting lasers (VCSEL) (27). Optically Pumped Semiconductor (OPS) gain medium offers a number of advantages over other solid-state gain media. Bandgap engineering of semiconductor structures allows the design of laser media with desirable properties, such as low threshold, high-power, wide potential tuning range, operating wavelength chosen by design, wide-pumping bandwidth, and efficient pump absorption within a few micrometers depth. Due to the rapid development of OPS, the technology has generated 7.3 W in blue (using LBO) (29), 7 W in green (using BBO) (30), and 5 W in yellow (using LBO) (31).

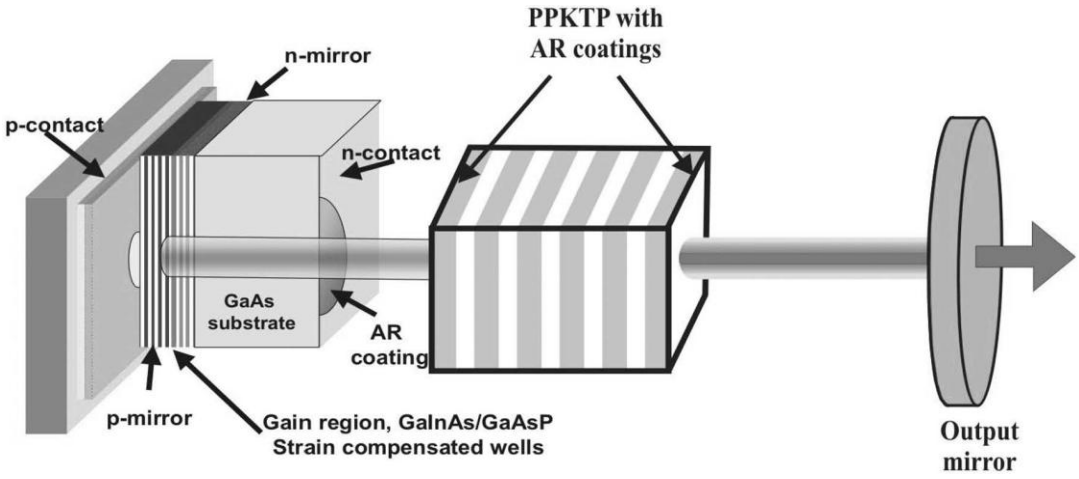

Figure 1.2 Scheme of electrically pumped VECSEL (32). Reproduced with permission.

In comparison with other diode-pumped solid-state lasers, OPS offers a number of distinct advantages. First, mature systems of semiconductor material are available for various wavelength requirements. Second, parameters of the laser can be controlled by bandgap engineering of the multi-Quantum Well structures. Third, there is a broad range of wavelength selection from infrared to ultraviolet (28).

However, challenges of VECSEL structure include complicated Periodically Resonant Gain (PRG) design and fabrication, growth of DBR mirror with extremely high reflectivity, and heat dissipation in the active region (29).

1.1.2.4 IC-FD of Edge Emitting Semiconductor Lasers

Another method to generate green laser light is to introduce the intra-cavity frequency doubling technology into the high power semiconductor lasers. This method is also a combination of semiconductor gain medium and intra-cavity frequency doubling nonlinear optical waveguides. Historically, little work has been done by this method in generating green light, partially because of the absence of laser diode emitting at 1060 nm. 1.35 mW of blue light was generated with FD technology within a KTP waveguide with a very small fluctuation of the output light (33). By introducing the fan-structured PP LiTaO3, researchers demonstrated tunability from 480.4 to 490.6 nm with output powers of the order of 50 nW (34). The first demonstration of the IC-FD of multi-edge-emitters laser bar was made by Li et al in 2009. A compact green laser of 1.3 W output at 534.7 nm was generated by IC-FD of a 49 edge-emitter laser bar using an MgO-doped (PPLN) bulk crystal (35).

A challenging task for building compact and integrated SHG devices is the combined thermal management of a diode laser and a periodically poled crystal. The crystals are usually operated at elevated temperatures which are unfavorable for diode lasers that are operated around room temperature. Reliable operation of QPM devices at high intensities at room temperature is demanded here. Some new materials like magnesium doped near-stoichiometric lithium tantalate ($LiTaO_3$) may solve this issue. (22)

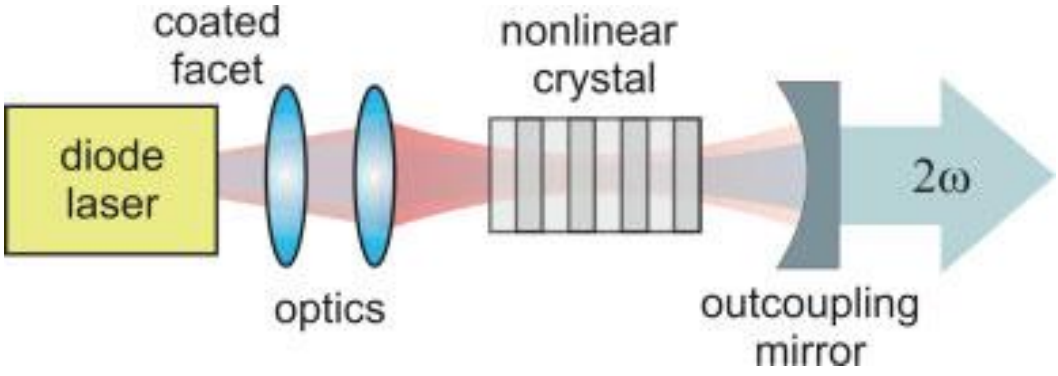

Figure 1.3 Principle of IC-FD of semiconductor lasers (22). Reproduced with permission.

1.2 Introduction to Lithium Niobate

Lithium niobate is widely used in achieving quasi-phase matching (QPM). Since its discovery in 1949 as a ferroelectric (36), lithium niobate has been under great development and usage as a very popular kind of nonlinear material. Lithium niobate does not exist in nature. It is a synthesized material first studied in the 1960s at Bell Laboratories in the form of single crystal (37). This ferroelectric material belongs to trigonal system. Figure 1.4 shows the positions of lithium atoms and niobium atoms in +c polarization.

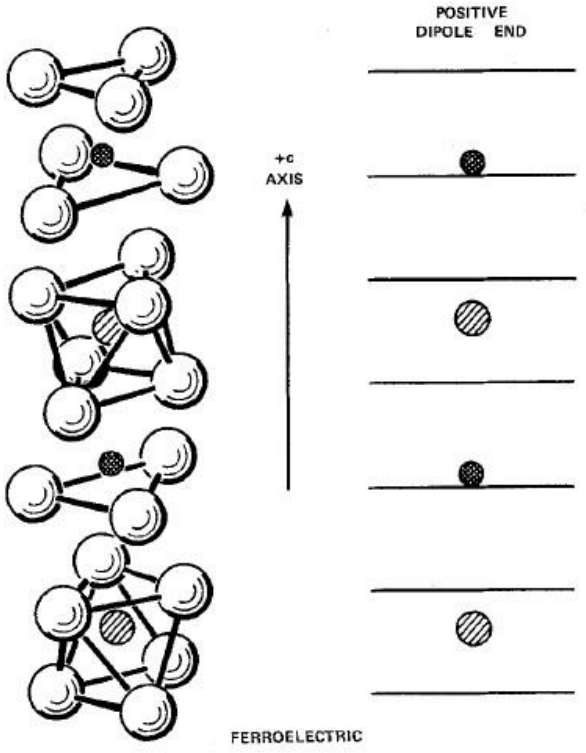

Figure 1.4 Positions of the lithium atoms (double cross hatched circles) and the niobium atoms (single cross-hatched circles) with respect to the oxygen octahedral in the ferroelectric phase of lithium niobate (38). Reproduced with permission.

The characteristics of lithium niobate are shown in Table 1.2.

Characteristic	Description
optical nonlinear	Light → Frequency conversion or mixing
electro optic	E field → Change of refractive index
photorefractive	Light → Change of refractive index
ferroelectric	E field → Change of spontaneous polarization
piezoelectric	Force → Electrical voltage
pyroelectric	Heating → Electrical fields
birefringent	Polarized light → Change of light polarization
acousto-optic	Acoustic waves → Index changes

Table1.2 Characteristics of Lithium Niobate (39)

Rather than stoichiometric composition of Li and Nb, the commonly used lithium niobate crystal is composed of the congruent composition around 48.5-48.6 mole% of Li_2O and 51.5-51.4 mole% of Nb_2O_5, usually grown by the Czochralski method (40). The photorefractive damage caused by this non-stoichiometric composition of lithium niobate can be greatly diminished by the doping of MgO (4.5 mole% or more) that causes the vastly improved photoconductivity (41).

1.3 Introduction to Nonlinear Light Propagation in Various Materials

Optical nonlinearity is the study of the phenomenon that light beams alter their own propagation in a medium as they modify the optical properties of the material system. Typically, laser light is involved in glasses or more generally Kerr media in the study of nonlinear optics. However, more kinds of media are introduced in the research of optical nonlinearity such as photopolymers and liquid crystals.

1.3.1 Different mechanisms in nonlinear light propagation

Since the first invention of maser in 1958 by Schwlow and Townes (42), the subject of nonlinear optics has been studied in great details and many new discoveries have been made within the field. Different kinds of mechanisms have been investigated as traditional types of materials have been studied, such as glasses (43), liquid crystals (44) and semiconductors (45), and newer materials such as photopolymers.

Nonlinear optical materials can be generally categorized into two mechanisms: the response of electrons within the media to the electric fields as it is

exposed to the light (typically laser light), and photochemical reactions that change the refractive index that usually takes place in photopolymers. Most of the nonlinear optical media rely on the response of the electrons and can be described by the relationship (46):

$$P=\varepsilon_0(\chi^{(1)}E+ \chi^{(2)}EE+ \chi^{(3)}|E2|E+\ldots) \quad (1.1)$$

Where ε_0 is the permittivity in vacuum, E is the amplitude of the electric field and $\chi^{(n)}$ is the order of susceptibility with n=1, 2, 3…

While the linear optics follows this form:

$$P=\varepsilon_0\chi^{(1)}E \quad (1.2)$$

As a result, the first term in Equation 1.1 corresponds to the linear response of the material and the second, third or higher order of susceptibility correspond to the nonlinear response of the electrons to the electric field E. Different types of nonlinearity include Kerr, photorefractive and quadratic nonlinearity.

1.3.2 Optical self-trapping

Self-trapping waves were first observed in 1834 (47) by John Scott Russell. He observed the water propagation in a canal which he called the "Wave of Translation". Since then, phenomenon of self-trapping of waves has been widely

studied in the form of charge density waves (48), sound waves (49), and electromagnetic waves (50).

Light has a natural tendency to broaden when it propagates in general media in time and space. However, when the refractive index of the medium changes as the light shines through it, it is possible to cancel the effect of diffraction and self-focus by having the light travel though with no change of its shape. As a result, the light guides itself to form a waveguide along the propagation direction (51).

The behavior of the optical wave is governed by the Maxwell's equations (Equations 1.3-1.6) where $\vec{E}$ is the electric field (V m^{-1}), $\vec{B}$ is the magnetic flux density (Wb m^{-2}), $\vec{H}$ is the magnetic field (A m^{-1}), $\vec{J}$ is the free current density (A m^{-2}), $\vec{D}$ is the electric displacement, and ρ is the free charge density (C m^{-3}).

$$\nabla \times \vec{E}(\vec{r},t) = -\frac{\partial \vec{B}(\vec{r},t)}{\partial t}, \tag{1.3}$$

$$\nabla \times \vec{H}(\vec{r},t) = \vec{J}(\vec{r},t) + \frac{\partial \vec{D}(\vec{r},t)}{\partial t}, \tag{1.4}$$

$$\nabla \cdot \vec{D}(\vec{r},t) = \rho(\vec{r},t), \tag{1.5}$$

$$\nabla \cdot \vec{B}(\vec{r},t) = 0, \tag{1.6}$$

From these equations, the propagation of the light characterized by electric field $\vec{E}$ can be described as in Equ 1.7:

$$\nabla^2 E - \frac{1}{c^2}\frac{\partial^2 E}{\partial t^2} = \frac{1}{\varepsilon_0 c^2}\frac{\partial^2 P}{\partial t^2} \tag{1.7}$$

While the polarization P consists of the linear part P_L and P_{NL}

$$P(r,t) = P_L(r,t) + P_{NL}(r,t) \tag{1.8}$$

$$P_L(r,t) = \varepsilon_0 \int_{-\infty}^{\infty} \chi^{(1)}(t-t') \cdot E(r,t')dt' \tag{1.9}$$

$$P_{NL}(r,t) =$$

$$\varepsilon_0 \iiint_{-\infty}^{\infty} \chi^{(3)}(t-t_1, t-t_2, t-t_3) \times E(r,t_1)E(r,t_2)E(r,t_3)dt_1 dt_2 dt_3 \tag{1.10}$$

For the complexity of the of this equation, it can be simplified if the nonlinear response is instantaneous so that the dependence of $\chi^{(3)}$is given by the product of three delta functions of the form $\delta(t-t_1)$, so the equation can be reduced to:

$$P_{NL}(r,t) = \varepsilon_0 \chi^{(3)} E(r,t)E(r,t)E(r,t) \tag{1.11}$$

The assumption of instantaneous nonlinear response amounts to neglecting the contribution of nonlinear vibrations to $\chi^{(3)}$(the Raman Effect).

The intensity dependence of the refractive index affects the electromagnetic wave as it travels through the media. In the context of spatial solitons, the analysis

is focused on the case of continuous wave (CW) beam. The general solution of equation (1.7) is

$$E(r,t) = A(r)\exp(i\beta_0 z) \tag{1.12}$$

Where $\beta_0 = k_0 n_0 \equiv 2\pi n_0/\lambda$ is the propagation constant as $\lambda = 2\pi c/\omega_0$. Assume the beam propagates along the Z direction and diffracts or self-focuses along direction X and Y, where X, Y and Z are the spatial coordinates associated with r. The function A(X, Y, Z) describes the evolution of the beam envelop. The nonlinear parabolic equation is in the following form:

$$2i\beta_0 \frac{\partial A}{\partial Z} + \left(\frac{\partial^2 A}{\partial X^2} + \frac{\partial^2 A}{\partial Y^2}\right) + 2\beta_0 k_0 n_{nl}(I)A = 0 \tag{1.13}$$

The scaled dimensionless variables are:

$$x = X/\omega_0 \tag{1.14}$$

$$y = Y/\omega_0 \tag{1.15}$$

$$z = Z/L_d \tag{1.16}$$

$$u = (k_0|n_2|L_d)esp(1/2)A \tag{1.17}$$

Where $\omega_0$is the transverse scaling parameter related to the input beam width and $L_d = \beta_0 {\omega_0}^2$ is the diffraction length or the Rayleigh range. By taking the dimensionless variables, the equation 1.13 becomes:

$$i\frac{\partial \mathrm{u}}{\partial \mathrm{z}}+\frac{1}{2}\left(\frac{\partial^{2} u}{\partial x^{2}}+\frac{\partial^{2} u}{\partial y^{2}}\right)\pm 2|u|^{2}u=0 \tag{1.18}$$

Where the choice of the sign is dependent on the sign of the nonlinear parameter n_2 ; when n_2 is negative, namely in the case of self-defocusing, the minus sign is adopted.

Optical spatial solitons have been observed in a variety of nonlinear media. The following is a survey on some of the most commonly studied types:

1.3.2.1 Kerr-type solitons

The first observation of self-trapping effect was made in 1964 by Hercher in glass through the Kerr effect (52). The mathematical solution to the nonlinear Schrodinger (NLS) equations gave the theoretical foundation for the study of Kerr effect (53). Several years later, Zakharov et al solved the full (1+1)D problem by using the method of inverse-scattering (54). Over time the uniqueness of the properties of the Kerr-type solutions was noted. One property is that Kerr solutions only propagate stably with only one transverse dimension, namely (1+1)D; with the introduction of another transverse dimension (2+1)D, it will cause the instability of the propagation that the beam suffers catastrophic self-focusing and eventually breaks up (55). Taking this into account, Barthelemey et al observed the true (1+1)

D Kerr soliton in liquid CS_2 with an interference grating to "arrest" the transverse instability (56). Later in 1990, Aitchison observed the true (1+1) D Kerr soliton in a single-mode glass waveguide (57). For a very long time, it seemed as if Kerr-type solitons were well understood while almost no study was done in other types of self-trapping beams (especially (2+1)D solitons).

1.3.2.2 Solitons in saturable media

Different from the (1+1)D solitons traveling in Kerr material, the first observation of (2+1)D self-trapping of a circular laser beam in sodium vapor was made by Bjorkholm and Ashkin of Bell Laboratories (58). They were able to control the frequency, intensity and beam diameter to make the beam self-trap for a finite propagation distance. They attributed the phenomena to the saturable nature of the optical nonlinearity. In 1991, theoretical explanation of the spatial solitons in saturable media was presented by Snyder's group (59). They introduced the idea that the "pulse" modifies the potential as a soliton comes into being that the pulse itself is a bound solution of that potential, so that it is explainable that circular beams can be stable in saturable media as there exists a maximum value for the optically induced refractive index change.

1.3.2.3 Photorefractive solitons

Photorefractive materials have been under study for over 40 years until now (60). Typically, photorefractive materials are dielectric single crystals that are non-centrosymmetric. They are generally semi-insulating with $\chi^{(2)}$ nonlinearities. Photorefractive materials always have dopants in the forms of donor and acceptors hosted within the crystal that have energy levels deep inside the forbidden gap. With an incident beam that excites charges from the deep dopant level into the conduction band, that causes the electrons free to move. If the incident beam is not uniform in space, after the dielectric relaxation time, the electrons are relocated because of the acceptors and the donors move to different spatial locations that results the charge separation which establishes electric fields within the material. This internal electric fields give rise to the refractive index change based on the electro-optic effect.

Photorefractive solitons were first predicted at Caltech in 1992 by Segev et al (61). The first observation of photorefractive solitons was made by Duree et al at the University of Arkansas in 1993 (62). One of the first and mostly studied kinds of photorefractive solitons will be described in detail, namely the photorefractive screening soliton. Assume a narrow beam travels through the center of a photorefractive crystal across which a voltage is applied. The density of electrons increases in the illuminated region where the conductivity increases. As a result, a

"voltage-divider" is formed because of the uniformity of the conductivity within the crystal, and the partial screening of the applied field in the region of the optical beam is attained. Based on the positive or negative of the change of refractive index, the beam will be either anti-guided or guided within the crystal.

1.3.2.4 Quadratic solitons

Quadratic solitons are a special kind of soliton that the optical fields do not change the properties of the medium such as refractive index, while the solutions rely solely on $\chi^{(2)}$. Typically the quadratic solitons are generated in non-centrosymmetric materials in which phase matching is possible, under a certain amount of power and over a narrow range of directions. Quadratic solitons have been primarily studied for second harmonic generation.

Quadratic solitons' stability issue was first reported by Kivshar's group in 1995 (63). In the same year, experimental verification was made by Torruellas et al for the existence of (2+1)D solitons(64), and a year later, Schiek et al at CREOL verified the existence of (1+1)D quadratic solitons (65). The quadratic solitons consist of both the fundamental and harmonic beams. The above experiments indicated that the second harmonic beam generates within the crystal and later forms the soliton. After the discovery of the quadratic solitons, they have been

under significant study in different areas, including: quadratically nonlinear resonators (66), beam pointing control in quadratic media (67), and angle steering in quadratic media (68)

1.3.3 Soliton interactions

One of the subjects that attract the interest of researchers is the interaction of solitons. Because of the unique property of solitons, the interactions of solitons are under study as particles, divided into two types: coherent and incoherent interactions. Both types are illustrated in Fig 1.5:

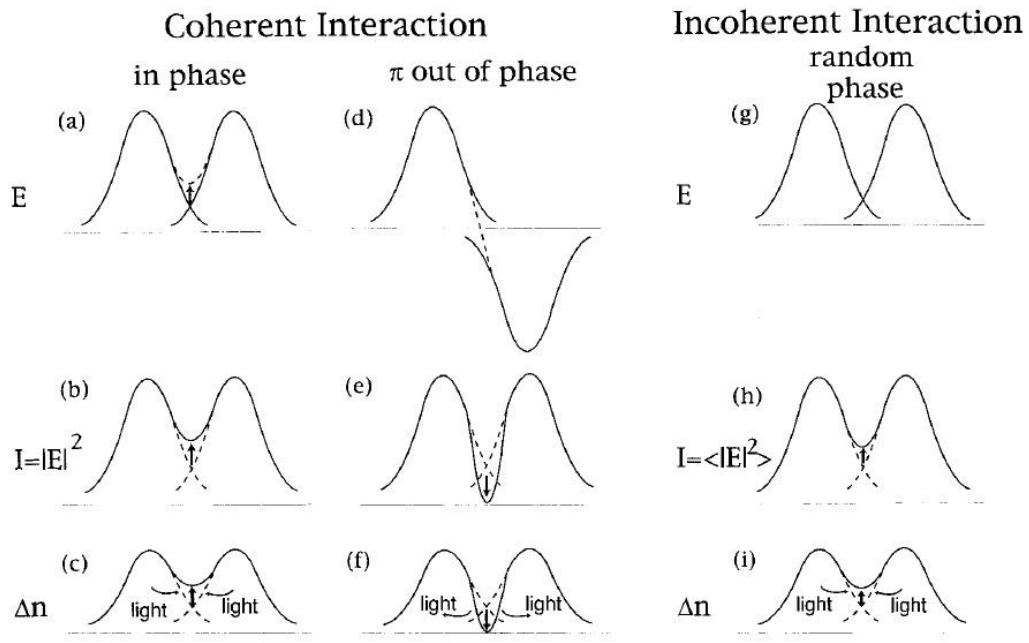

Figure 1.5 Illustration of coherent and incoherent soliton interactions (69). Reproduced with permission.

1.3.3.1 Coherent Interactions

Coherent soliton interactions occur when the nonlinear medium responds to interference effects between the overlapping beams since the response time of the material is extremely fast (such as the quadratic nonlinearity and the optical Kerr effect), is near-instantaneous. In this case, assuming the beams are in-phase (with

zero relative phase), they interfere constructively, and as a result the light intensity of the central region increases. If it is a self-focusing medium which the beams are propagating through, the refractive index of the region will increase and more light will be attracted to the central region, therefore the solitons appear to be self-attracting. Assuming the beams are out of phase (with π relative phase), they interfere destructively, and as a result the light intensity of central region decreases. For a self-focusing medium, the refractive index of the central region decreases and light beams will be repulsed away from each other, therefore the solitons appear to be self-repulsing.

1.3.3.2 Incoherent Interactions

Incoherent soliton interactions occur when the nonlinear medium responds to interference effects between the overlapping beams since the response time of the material is slower than the variations of the beams. In this case, the medium responds to the average intensity over time, while the intensity is of the same amount of the superposition of the intensities. Therefore, irrelevant to the phase difference, the intensity is the sum of the beam intensities, and the intensity in the central region increases. Assume the beam propagates in a self-focusing material,

the refractive index increases in the central region as the beam travels through it. As a result, the incoherent soliton interactions always appear to be self-attracting.

1.3.3.3 Collisions in Kerr Media

In Kerr materials, the solitons are always (1+1) D so the collisions occur in one single plane. Since all the collisions are fully elastic, the number of solitons is constantly conserved. When the attractive collision occurs between the solitons, the solitons propagate forward as they combine and separate periodically.

1.3.3.4 Collisions in Saturable Media

Since the saturable nonlinear media support the (2+1) D solitons, the collisions of solitons in saturable media is much richer than the one plane interaction of Kerr media. More than one mode is supported within the media, and therefore, new phenomena such as soliton fusion, fission and annihilation have been observed (70). DNA-like structure of soliton spiraling was demonstrated in photorefractive screening solitons in 1997. (71)

In the (2+1) D mode of soliton interaction in saturable media, if the solitons are separately launched, they propagate in their initial individual trajectories. If the solitons are launched simultaneously, they attract or repel each other as they propagate though. As shown in Fig 1.6, the solitons spiral and orbit one another when the soliton attraction perfectly balances the "centrifugal force" as they rotate.

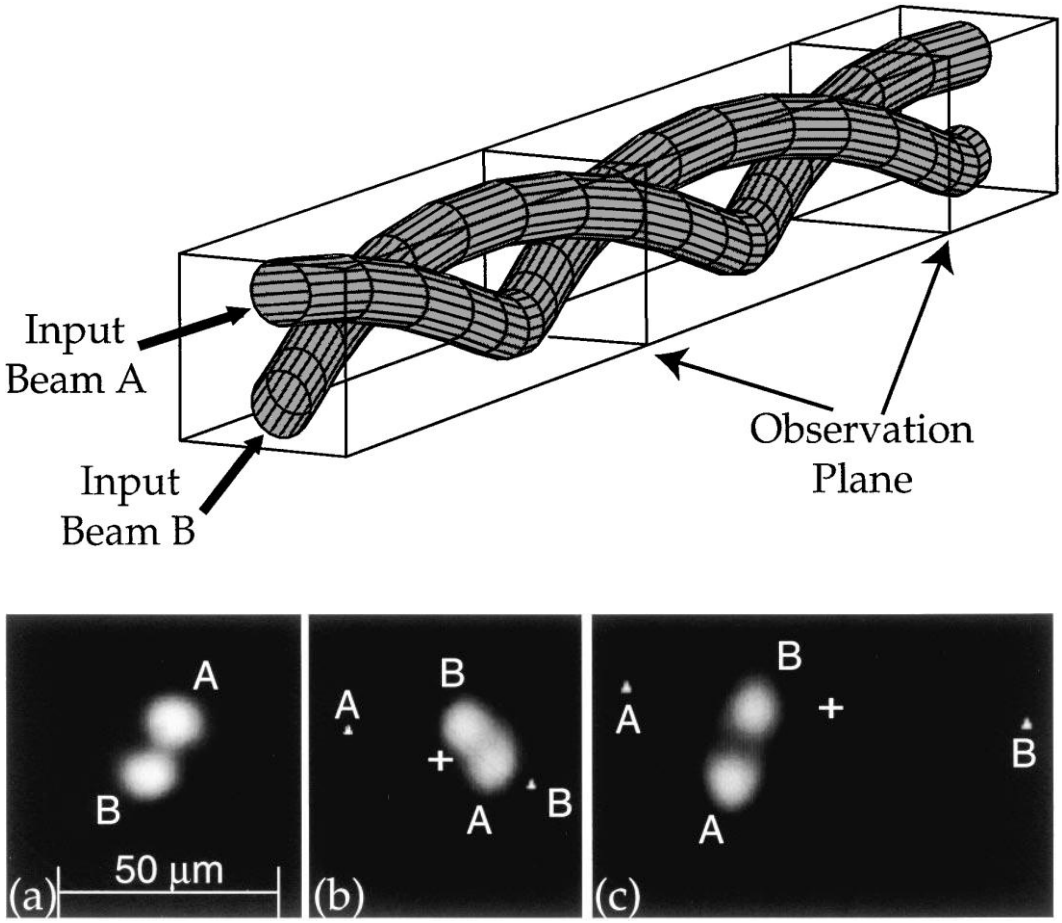

Figure 1.6 Illustration of solitons orbit about each other in a DNA-like structure in saturable nonlinear media. a) Beam A and beam B at the input face of the crystal, b)

the spiraling soliton pair after 6.5mm of propagation, c) the spiraling soliton pair after 13mm of propagation (72). Reproduced with permission.

1.4 Introduction to self-trapping systems

An optical beam suppresses its own diffraction as it travels through the medium by changing the refractive index of the medium through which it propagates, leading to a variety of self-action phenomena. When the self-trap phenomenon occurs, a typical Gaussian beam propagates within a self-induced waveguide without broadening over distance. The self-trapping beams are essentially the solutions of the nonlinear Schrodinger equation as introduced earlier in this chapter. The phenomena of optical self-trapping have been studied since the 1960s (99) in different kinds of materials such as photorefractive media (69), Kerr materials (53).

The dynamics of the self-trapping beams are determined by the mechanisms of the refractive index changes within materials that the beams are propagating through. Due to the difference of the cause of the refractive index change in photorefractive material and Kerr materials, the optical self-trapping in these two materials is strikingly different. Since the refractive index change of Kerr material is caused by the third-order susceptibility tensor, self-trapping only happens with high intensity (GW cm^{-2} to TW cm^{-2}), short pulse(10^{-15} s) light, and only the

(1+1)D beam can stably propagate in the Kerr material while the (2+1)D beams will suffer from catastrophic self-focusing and eventually beak up (55). Much different from the Kerr material, the refractive index change in photorefractive material is originated from the electro-optic effect, and as a result the (1+1)D and (2+1)D self-trapping beams can propagate through stably with relatively low intensity. Due to the unique features of photorefractive material, even white light can self-trap when traveling through this material (100).

The self-trap phenomenon within the organosiloxane media is different from the self-trap within other nonlinear optical (Kerr, refractive) media. Self-trapping in organosiloxane is originated from a photo-initiated free-radical polymerization reaction as the beam travels through (101). The differences between the organosiloxane nonlinear dynamics and other nonlinear materials dynamics are attributed to some fundamental difference in the nature of the materials. The photo-polymerization-induced refractive index changes are permanent while the refractive index changes in Kerr material or photorefractive material is temporary, namely, the refractive index modifies only with the light on, and the change decays immediately as the removal of the light field. The refractive index change in the photosensitive material is at least an order of magnitude greater than that in Kerr material with the same intensity of light field. The beam attenuation in the photosensitive material can be negligible since the photopolymerization can happen with a very few amount of light-absorbing photoinitiator molecules. Based on the wavelength and the quantum yield of photoinitiation (102), the photopolymerization

can take place at a very low intensity of light with a large range of wavelengths. However, as discussed above, the refractive index change happens within the Kerr material only with extremely high intensity short pulse light. There also exists a remarkable difference in the photoresponse time within different materials: the photoresponse time ranges from milliseconds to minutes within photosensitive material since the photopolymerization happens as the photochemical reactions take place; the photoresponse time ranges from nanoseconds to minutes within photorefractive materials since the photoresponse time is determined by the dielectric relaxation times of the material; and the photoresponse time within Kerr material is instantaneous as it is determined by the instantaneous electronic response which is in the order of 10^{-15}seconds.

1.5 Research Objectives and Thesis Outline

The obvious advantages of the Intra-cavity Frequency-Doubling (IC-FD) design of continuous wave (CW) green laser of 532 nm wavelength, using MgO: PPLN as the frequency doubling crystal, are described briefly in the previous sections. Therefore, designing the green laser with higher efficiency, improved beam quality and smaller size is one of the objectives of this thesis, and is the prerequisite for the following experiment on the different self-actions in photopolymerizable organosiloxane induced by the green laser.

With the green laser as the light that can induce the self-actions in photopolymer, a detailed study on the experimental investigation is the main objective of this thesis. This includes two parts: the single beam self-trapping in the photopolymer and the two-beam interaction in the photopolymer.

The outcome of the self-trap in the photopolymerizable medium is the refractive index change of the material. Under certain conditions, a Gaussian beam propagating in the nonlinear medium can be achieved that the refractive index change causes the curve wave front having the shape of the convex lens. By altering the intensity of the incident beam, the self-focusing effect of the medium functions as a convex lens. Because of the small size and low manufacturing cost of the miniaturized laser, this laser is the ideal candidate for the "light-guide-light" experiment light source. This can be easily implemented into a simple experimental set-up, and much lower cost for large numbers of repetitive experiments, as well as future commercial applications.

For the single beam experiment, the study on the evolution of the modes, the excitation of high-order modes is reviewed in the low intensity regime of the incident light. Intensity dependent study is also performed so that the formation of the diffraction rings caused by the difference in the refractive index change, and the examination of the dynamics of different phenomena can be observed.

For the two-beam interaction experiment, detailed results are provided with three sets of pinhole arrays that split the light into two coherent parallel lights with different distance between the beams.

Further comparison, theoretical simulation, and the design of the IC-FD is reviewed in Chapter 2 and Chapter 3. With a IC-FD MgO: PPLN/Nd:YVO_4 laser employed as the light source, a variety of self-actions have been observed in the photopolymerizable organosiloxane. Theoretical studies are reviewed in Chapter 2 and Chapter 3, and experimental results are presented in Chapter 4 and Chapter 5.

Chapter 2 THEORETICAL BACKGROUND OF INTRA-CAVITY FREQUENCY DOUBLING GREEN LASER

2.1 Introduction

This chapter provides a theoretical background for the design and fabrication of Intra-Cavity Frequency Doubling (IC-FD) lasers. Section 2.2 describes the derivation of the governing equations of the traveling wave propagation in gain media. This is followed by the introduction of the quasi-frequency-matching (QPM) within the nonlinear medium, with an emphasis on the characteristic and fabrication of periodically poled lithium niobate (PPLN). Sections 2.4-2.5 of this chapter is a brief description of the IC-FD green laser based on the outlined theoretical analysis.

2.2 Maxwell's Equations and Governing Equations (46)

To consider the form of wave equation for the propagation of light through a nonlinear optical medium, we start with the Maxwell equations that generally describe the behavior of optical waves.

$$\nabla \times \vec{E}(\vec{r},t) = -\frac{\partial \vec{B}(\vec{r},t)}{\partial t} \quad , \tag{2.1}$$

$$\nabla \times \vec{H}(\vec{r},t) = \vec{J}(\vec{r},t) + \frac{\partial \vec{D}(\vec{r},t)}{\partial t} \quad , \tag{2.2}$$

$$\nabla \cdot \vec{D}(\vec{r},t) = \rho(\vec{r},t), \tag{2.3}$$

$$\nabla \cdot \vec{B}(\vec{r},t) = 0, \tag{2.4}$$

Where $\vec{E}$ is the electric field (V m^{-1}), $\vec{B}$ is the magnetic flux density (Wb m^{-2}), $\vec{r}$ and t represent the space coordinate vector and time variable respectively, $\vec{H}$ is the magnetic field (A m^{-1}), $\vec{J}$ is the free current density (A m^{-2}), $\vec{D}$ is the electric displacement, and ρ is the free charge density (C m^{-3}).

There is no free charge in dielectric materials, and there is no free current, and as a result

$$\rho = 0 \tag{2.5}$$

$$\vec{J} = 0 \tag{2.6}$$

In nonmagnetic ($\mu_r = 1$) materials, the constitutive relations are

$$\vec{B}(\vec{r},t) = \mu_0 \vec{H}(\vec{r},t), \tag{2.7}$$

$$\vec{D}(\vec{r},t) = \varepsilon_0 \vec{E}(\vec{r},t) + \vec{P}(\vec{r},t). \tag{2.8}$$

By taking the curl of Eq. (2.1), and using Eqs. (2.2), (2.6) and (2.7):

$$\nabla \times \nabla \times \vec{E} + \mu_0 \frac{\partial^2 \vec{D}}{\partial^2 t} = 0. \tag{2.9}$$

In order to eliminate $\vec{D}$, we take Eq.(2.8) into Eq.(2.9)

$$\nabla \times \nabla \times \vec{E} + \frac{1}{c^2}\frac{\partial^2 \vec{E}}{\partial t^2} = -\mu_0 \frac{\partial^2 \vec{P}}{\partial t^2} . \tag{2.10}$$

By taking use of vector calculus identity $\nabla \times \nabla \times \vec{E} = \nabla\left(\nabla \cdot \vec{E}\right) - \nabla^2 \vec{E}$, we get

$$\nabla^2 \vec{E} - \frac{1}{c^2}\frac{\partial^2 \vec{E}}{\partial t^2} = \mu_0 \frac{\partial^2 \vec{P}}{\partial t^2} . \tag{2.11}$$

Most of the nonlinear optical media rely on the response of the electrons and can be described by the relationship

$$\vec{P} = \varepsilon_0\left(\chi^{(1)}\vec{E} + \chi^{(2)}\vec{E}\vec{E} + \chi^{(3)}\left|\vec{E}\right|^2 \vec{E} + \cdots\right). \tag{2.12}$$

Where ε_0 is the permittivity in vacuum, E is the amplitude of the electric field and $\chi^{(n)}$ is the order of susceptibility with n=1, 2, 3…

The polarization and displacement of field can be split into its linear and nonlinear parts as

$$\vec{P} = \vec{P}^{(1)} + \vec{P}^{NL} . \tag{2.13}$$

$$\vec{D} = \vec{D}^{(1)} + \vec{P}^{NL} , \tag{2.14}$$

Taking Eqs (2.12), (2.13) and (2.14) into Eq (2.11), we get the wave equations in linear and nonlinear media respectively:

$$\nabla^2 \vec{E} - \mu_0 \frac{\partial^2 \vec{D}^{(1)}}{\partial t^2} = 0 . \tag{2.15}$$

$$\nabla^2\vec{E}-\mu_0\frac{\partial^2\vec{D}^{(1)}}{\partial t^2}=\mu_0\frac{\partial^2\vec{P}^{NL}}{\partial t^2}\quad. \tag{2.16}$$

Since the liner susceptibility $\chi^{(1)}$ can be written in the form of $\chi^{(1)}=\chi'-i\chi''$ in solid state media, and then the wave equation Eq. (2.15) for an isotropic gain medium becomes:

$$\nabla^2\vec{E}=\frac{1}{c^2}(1+\chi'-i\chi'')\frac{\partial^2\vec{E}}{\partial t^2}\quad. \tag{2.17}$$

2.3 Quasi-Phase-Matching

The idea of quasi-phase-matching can be illustrated with Fig 2.1. Fig. 2.1(a) describes a homogeneous single crystal and (b) describes a periodically poled material where Λ is the period. For a periodically poled material, the orientation of the crystalline axes is inverted within the material, the inversion of the orientation gives rise to the changing of the sign of nonlinear coupling coefficient d_{eff}. Compared to perfect phase-matching and phase-mismatching, the spatial variation of the field amplitude is shown in Fig 2.2, in which the curve (a) is the perfect phase-matching situation that the field amplitude grows linearly with distance. Curve (b) describes the quasi-phase-matching condition that the field amplitude grows periodically with the distance of propagation due to the periodic inversion of

the orientation of the crystalline axes, in which case, the crystalline inversion period Λ is twice the coherent buildup length L_{coh} . Curve (c) is the illustration of the phase-mismatch condition where there is no growth of the field amplitude. With the perfect phase-matching condition, the interacting fundamental and Second Harmonic (SH) waves always have a fixed phase relationship as the light propagate through the nonlinear crystal, and as a result, the power of SH increases along with the propagation distance. However, with a phase mismatch condition, the generated SH power is converted back to the fundamental power. The Quasi-phase matching (QPM) condition is that the reversal of the sign of d_{33} enables the growth of the field amplitude as the SH is about to decrease because of the mismatch of the wave vector.

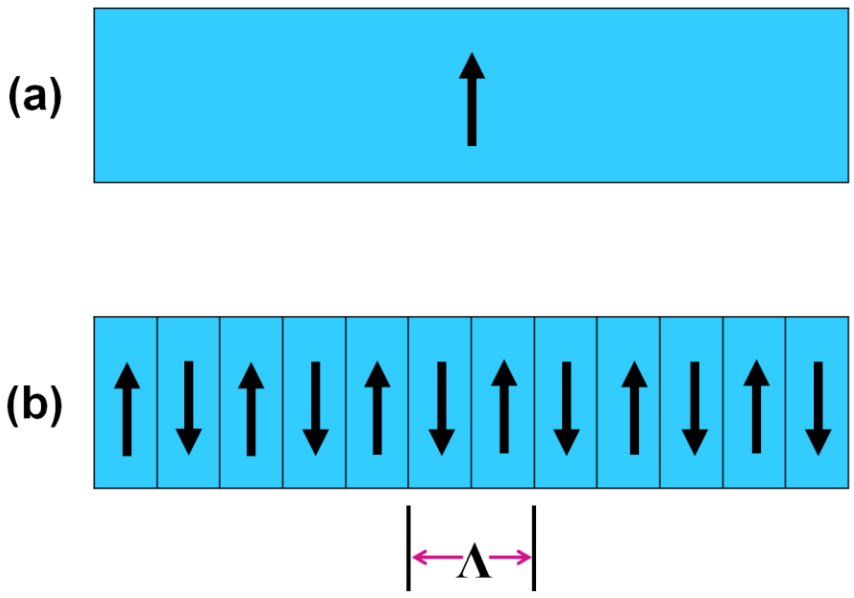

Figure 2.1Illustration of the nonlinear optical material in a) a single crystal and in b) the periodically poled material with the period of Λ. (46)

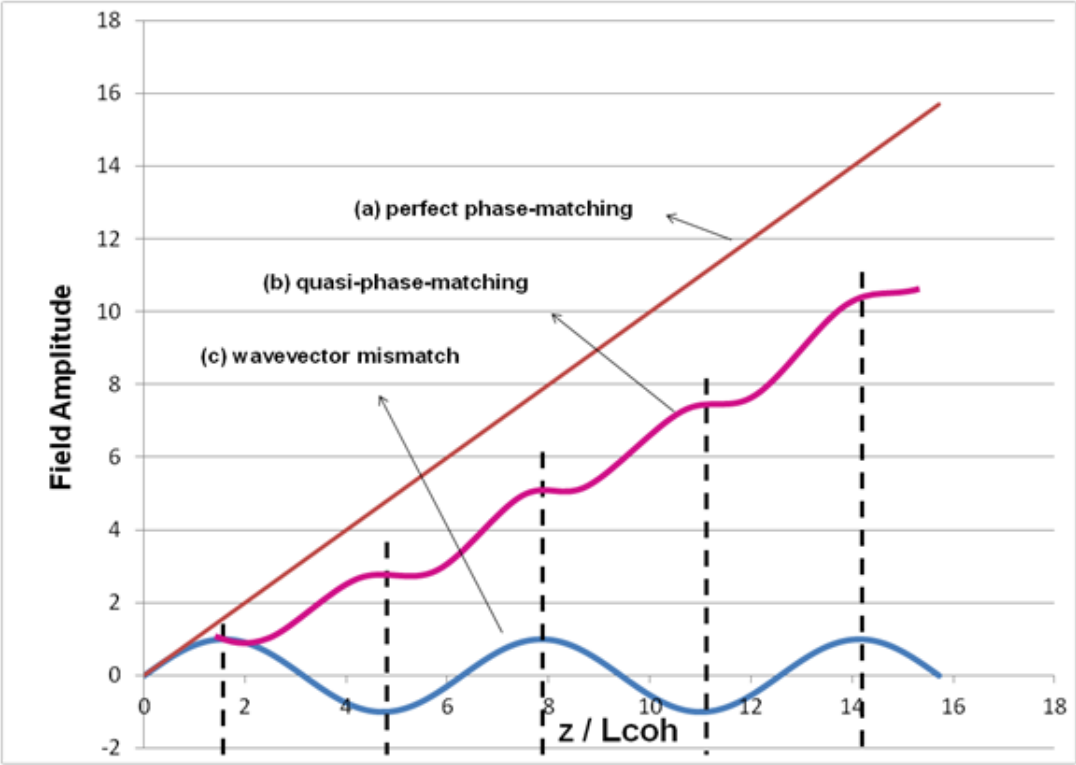

Figure 2.2 Comparison of the field amplitude among perfect phase-matching, quasi-phase-matching and phase-mismatching.

QPM is superior over the traditional phase-matching techniques in several ways: QPM makes use of the largest nonlinear coefficient of the nonlinear material; QPM does not have the "walk-off" effects as the birefringence phase-matching crystals.

Different methods of the fabrication of the quasi-phase-matching structures have been proposed over the last half century. The first idea was given by Armstrong et al in 1962 (73). In this paper, Armstrong suggested to slice the nonlinear medium into segments and align them together by 180 ° rotation. Due to

the difficulty of the slicing of the thinness of the segments required, this method is replaced by some recent innovations. One of the method was proposed by Ito et al in 1991 (74). Using direct electron beam writing, the periodically poled bulk lithium niobate was used to generate SHG green and blue light. Five years later, Harada et al (75) developed the method of fabrication of periodically poled MgO-$LiNbO_3$ by corona discharge, and a 6.7 mW blue light of 490 nm was demonstrated with the PPLN crystal. The most commonly used method is by applying a high voltage that generates the uniform grating (76); (77); (78). As illustrated in Fig.2.3, this is the method of voltage electric field application. In order to periodically pole lithium niobate, the periodical electrode must be fabricated first. The fabrication involves the deposition of metal on the +z surface by electron beam evaporation, the lithography on the surface of the metal-deposited photo-mask, and finally selective etching (77). As indicated in Fig 2.3, the periodical metal electrode has the metal grid width W and grid period Λ.

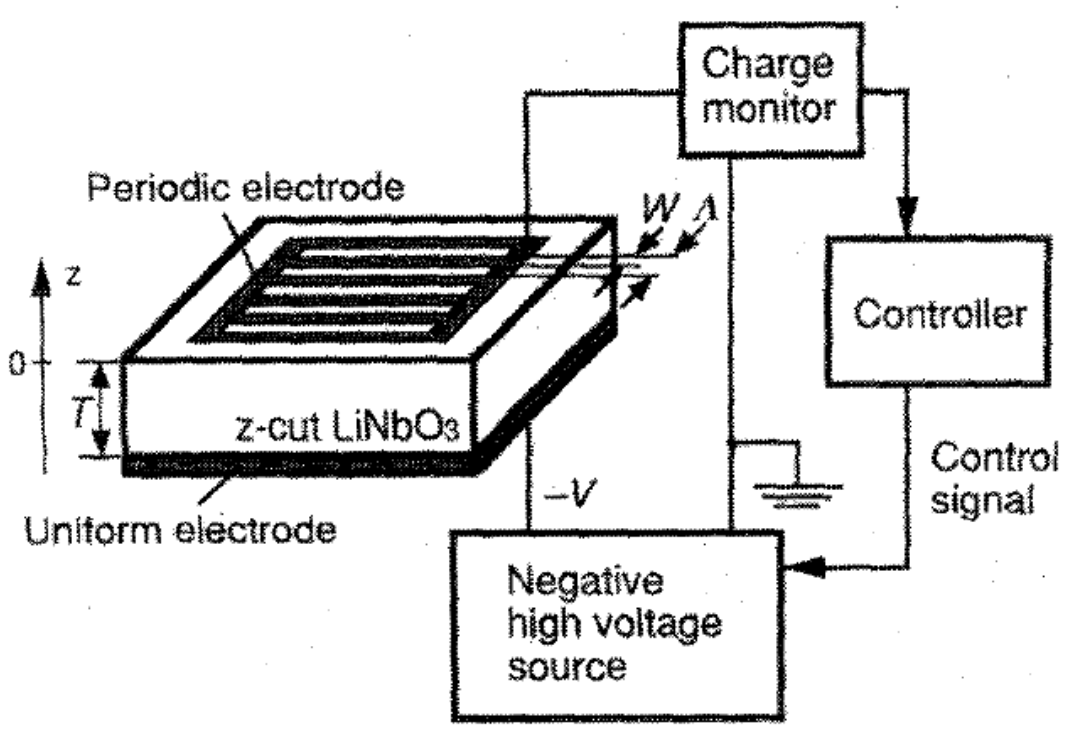

Figure 2.3 Fabrication of periodically poled lithium niobate by high voltage method (78). Reproduced with permission.

2.4 Intra-Cavity Frequency-Doubling

As discussed in Section 1.1, the method of Intra-Cavity Frequency-Doubling (IC-FD) or Intra-Cavity Second-Harmonic-Generation (IC-SHG) has higher efficiency compared to the single-pass SHG method. As the FD crystal is included within the cavity which has a mirror of very high refractivity in the end, the conversion efficiency can be improved drastically compared to a single pass

process. The first demonstration of IC-FD laser was made within the Bell Laboratories in 1968 by Geusic et al with a 1064 nm YAlG:Nd Laser and frequency doubled by $Ba_2NaNb_5O1_5$ nonlinear material, with 1.1 W of coherent green laser output of 532 nm (79). Two years later, the theoretical analysis was provided in great details (80).

2.5 The Superiority of the IC-FD green laser

Efficient and high power continuous wave (CW) green lasers have a wide variety of applications such as laser display, underwater communications and bio-photonics. Many attempts have been made to improve the efficiency of the laser system. Because of the special requirements for a systematic study on the self-action phenomena in photopolymerizable medium, it is required that the light source to be stable and tunable in the output power. It must also be high in efficiency, small in size (so that it can be easily incorporated into the optical set-up) and low in cost to allow repetitive experiments over more than eight orders of magnitude of beam intensities.

Direct InGaN green laser diodes have been under intensive development though they are still far from mature. The electricity-to-optical (EO) efficiency of the InGaN green laser is reported as low as 1% at 531 nm, and 3-5% at around 521 nm (7); (8); (81), and 7.0-8.9% at 530 nm (9). Another well-developed method is

the intra-cavity frequency doubling (IC-FD) (or intra-cavity second harmonic generation (IC-SHG)) of the diode pumped solid state (DPSS) green lasers. So far the EO efficiency of this type of laser can be as high as 20% in the high power regime (15); (16); (17), and up to 15% with optical contact Nd: YVO_4/MgO: PPLN design (82); (83). A more straightforward method that attracts much interest is the single-pass frequency doubling of semiconductor laser using bulk or waveguide nonlinear crystals. This method has less number of conversion steps than IC-FD DPSS lasers. Instead of conversion from electricity to 808 nm, 808 nm to 1064 nm, and 1064 nm to 532 nm, the single pass design converts the 1064 nm light emitted from the semiconductor laser diodes directly to 532 nm green light. As a result, at low pump power range, the EO efficiency of the single pass can be potentially as high as 30% when the pump is less than 1 W, as reported in a series of studies by Nguyen et al at Corning Inc (26); (84); (85); (86); (87); (88). It has been reported by the same group that the average wall-plug efficiency of 10% achieved green light generation with the method of single-pass frequency-doubling of semiconductor lasers with PPLN. Such device performance sets a benchmark for other types of green laser designs. Single-pass FD green laser has its own advantages and disadvantages. Some advantages include low noise, high frequency modulation capacity and potential low cost that make it an ideal candidate for the micro-mirror-based laser projection systems (89). However, some disadvantages include narrow temperature tolerance, the necessity for a long nonlinear crystal, and apart from

these, a portion of the fundamental power is unavoidably wasted due to the single-pass design.

The problems of the single-pass frequency-doubling green lasers are solved by a superior design of intra-cavity frequency-doubling (IC-FD) of semiconductor lasers both theoretically (80); (90); (91) and experimentally (35). With the pump current of 700 mA and coupling efficiency of 70%, the green light emission power vs. injection current was compared among the single-pass FD laser with 12 mm MgO: PPLN crystal and IC-FD lasers with 6 mm and 12 mm MgO: PPLN crystals as illustrated in Fig. 2.4. Fig.2.5 shows the calculated green light emission power with different MgO: PPLN crystal lengths for IC-FD and single-pass FD lasers, with coupling efficiency of 70% and pump current of 700 mA. It is clearly evident from the simulated results that the IC-FD design is superior to single-pass FD design with higher efficiency.

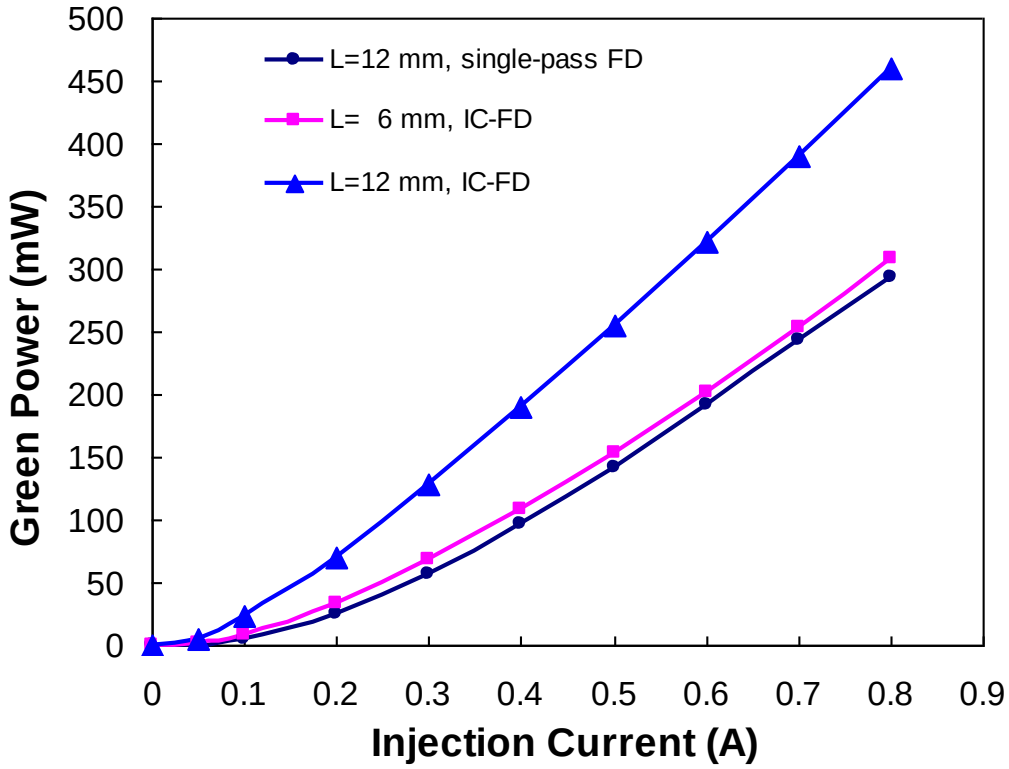

Figure 2.4 Comparison of green power vs. injection current among IC-FD laser with two MgO: PPLN lengths and a single-pass FD laser with the same parameters. The coupling efficiency is 70% (91). Reproduced with permission.

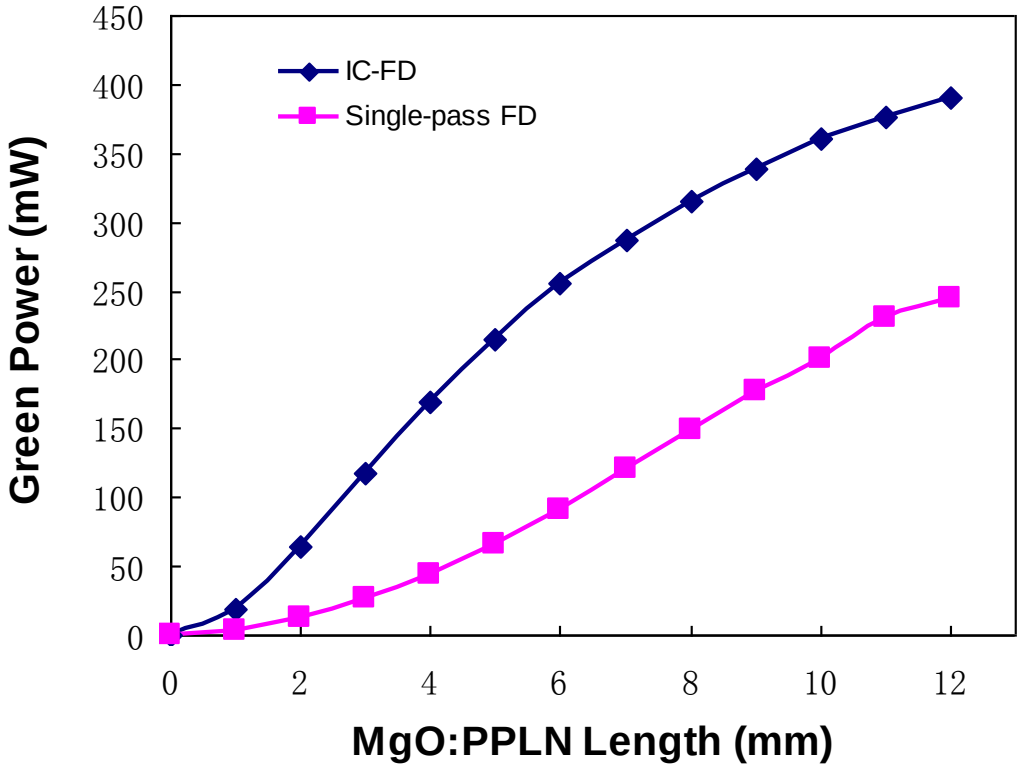

Figure 2.5 Comparison of green power vs. MgO: PPLN crystal length between IC-FD laser and single-pass FD laser. The coupling efficiency is 70% and pump current is 700 mA (91). Reproduced with permission.

In addition to higher efficiency, it has been reported that the IC-FD design also possesses better temperature tolerance and coupling efficiency than the single-pass design, according to Xu et al in 2011 (91). Fig 2.6 shows the temperature tuning curves for the IC-FD laser with 6 mm MgO: PPLN crystal and single-pass FD laser with 12 mm MgO: PPLN crystal with 700 mA pump current and 70% coupling efficiency. Fig 2.7 indicates the comparison between output power with different coupling efficiency when the pump current is 700 mA between the IC-FD

design and the single-pass FD design. It is evident that green light output power of IC-FD design is much higher than the power of single-pass FD design at low coupling efficiency. Since high coupling efficiency is quite difficult to achieve in practice (>80% for the 6 mm crystal and >90% for the 3 mm crystal), the conclusion is the IC-FD design is superior to single-pass FD design.

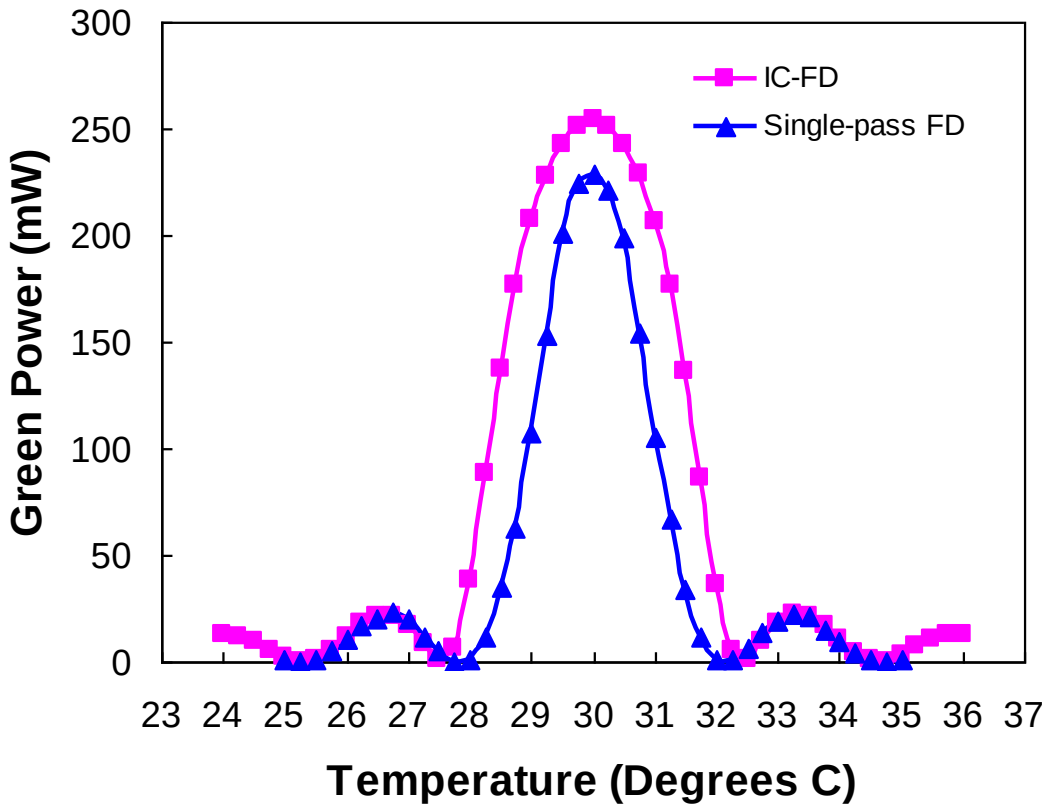

Figure 2.6 Temperature tuning curves for the IC-FD laser with 6 mm MgO: PPLN crystal and single-pass FD laser with 12 mm MgO: PPLN crystal with pump current of 700 mA and coupling efficiency of 70% (91). Reproduced with permission.

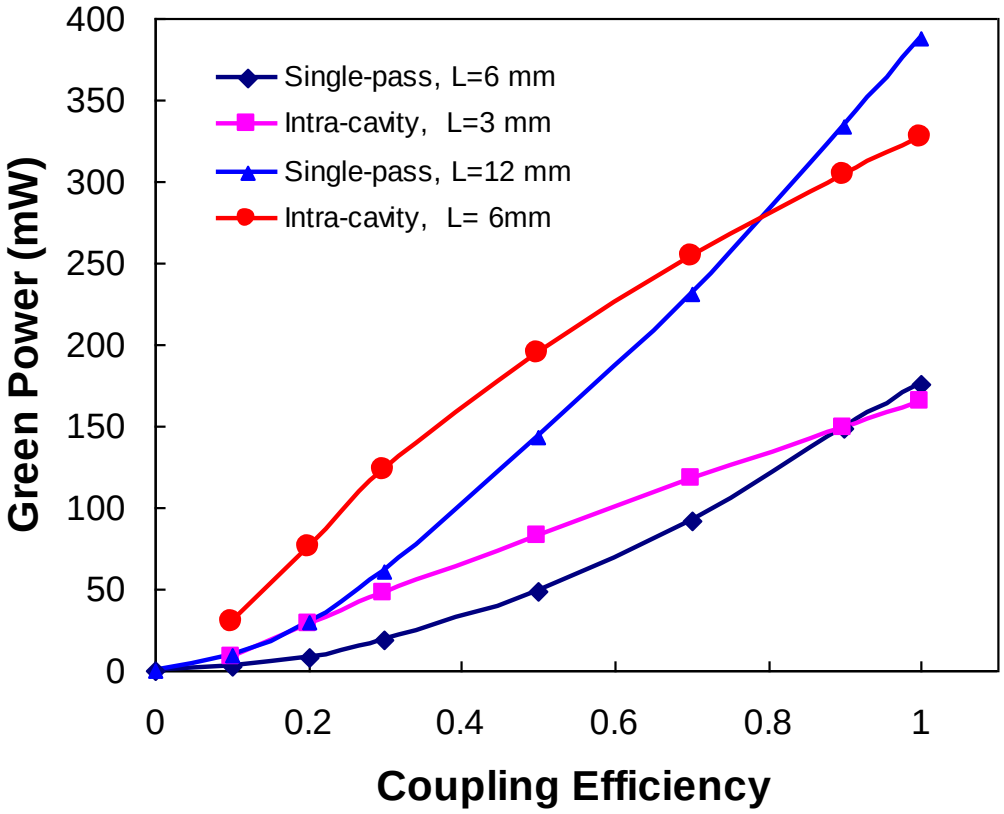

Figure 2.7 The output power for single-pass FD and IC-FD lasers with different coupling efficiency between semiconductor LD and MgO: PPLN crystal, when the pump current is 700 mA (91). Reproduced with permission.

Because of the advantages such as high efficiency, simplicity in designing and smallness in size, Nd/YVO_4/MgO:PPLN green laser with optical contact crystals attracts lots of interest among researcher these years. Due to the small size of the crystals and the simple design of the optical contact, this kind of green laser is sometimes called microchip green laser (82-83); (92-97). In 2010, over 500 mW

of green laser at the wavelength of 532nm was demonstrated with the electrical-to-optical efficiency of 9.3% (93).

Chapter 3 EXPERIMENT DESIGN AND MATERIALS

3.1 Introduction

In this chapter, the design of the Nd: YVO_4/ MgO: PPLN green laser with the method of intra-cavity frequency doubling (IC-FD) is described. A detailed description of the preparation of the photosensitive organosiloxane is given in Section 3.2. Finally, the optical set-up and the characterization techniques were introduced in detail.

3.2 Design and Performance of Nd: YVO_4/MgO: PPLN Green Laser

The design of the optical contact Diode Pumped Solid State (DPSS) laser involves some crucial issues: the design of the plano-parallel cavity structure, and the control of the operation temperature. The structure of the optical contact crystals is shown in Fig 3.1, and the construction of the microchip and the C-mount 808-nm is shown in Fig 3.2.

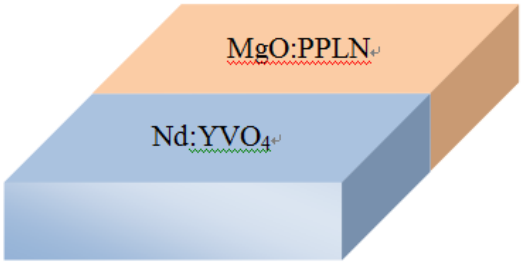

Figure 3.1 3-D structure of the microchip consist of Nd:YVO_4 and MgO: PPLN (98). Reproduced with permission.

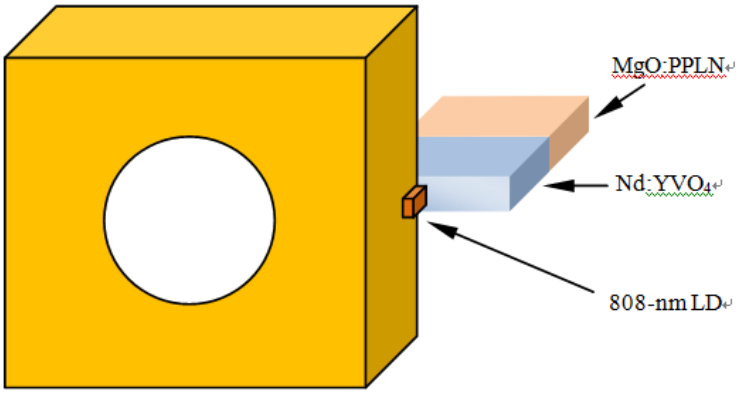

Figure 3.2 Schematic of the construction of a green laser using an 808-nm LD and a PPLN microchip (98). Reproduced with permission.

According to the PPLN crystal provider C2C Link Corporation, in order to achieve higher conversion efficiency of the laser, the 808 nm LD should be rotated by 90 ° as shown in Fig 3.2. The specification of the microchip is also available from the company manual as shown in Table 3.1.

Material	Nd:YVO_4/MgO:PPLN
Pumping Wavelength (nm)	808 nm
Operating Temperature	~25 ℃
Facets	Input: HT at 808nm, HR at 1064nm & at 532nm, Output: HR at 1064nm, AR at 532nm
Optical to optical efficiency	≥ 13%
Dimension	1.5 mm(L)×2.2 mm(W)×0.5 mm (T)

Table 3.1 Specification of the Nd: YVO_4/MgO: PPLN microchip (98). Reproduced with permission.

A Laser Diode of 808 nm wavelength emits 50 mW of power and the light is collimated into a Gradient-index (GRIN) lens. The focused beam has a very small 70 μm size on Nd: YVO_4 crystal. The crystals set is composed of 3% doped Nd: YVO_4 of 0.5 mm in length and MgO: PPLN of 1 mm in length. The MgO: PPLN with an effective nonlinear coefficient (d_{eff}) of 17 pm/V was provided by the C2C Link Corporation (http://c2clink.com/). The input facet of Nd: YVO_4 has Anti-Refractive (AR) coating at 808 nm (R < 10%) and High-Refractive (HR) coating at 1064 nm and 532 nm (R > 99.85%). The output facet of MgO: PPLN has HR coating at 1064 nm (R > 99.85%) and AR coating at 532 nm (R < 5%). The reflection coefficient is extremely small at the contact interface of Nd: YVO_4 crystal and MgO: PPLN crystal because of the refractive index difference between the crystals is very small. Theoretically, the reflection coefficient is as small as

0.002%. A set of TEC is adopted to control the thermal stability of the Nd: YVO_4/PPMgLN chips as well as the temperature of the whole system. In Fig 3.3 the design of the Nd: YVO_4/PPMgLN green laser is illustrated. In Fig 3.4 the real green laser manufactured with such design is illustrated, emitting green light.

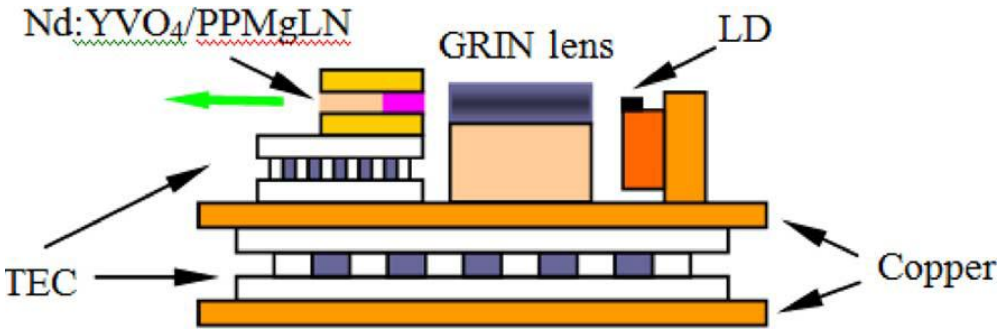

Figure 3.3 Schematic structure of the optical contact Nd: YVO_4/PPMgLN green laser on a side view (82). Reproduced with permission.

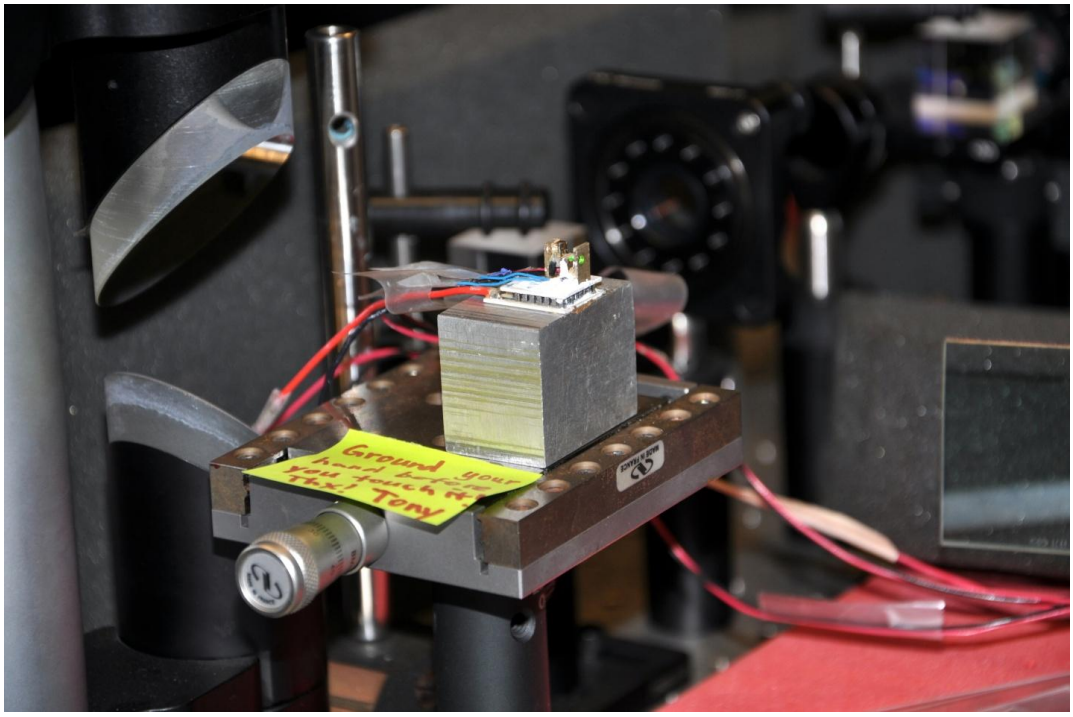

Figure 3.4 Picture of the real laser emitting green light

The experimental results of the output power of the IC-FD Nd: YVO_4/PPMgLN green laser is shown in Fig 3.5, with the electrical-to-optical efficiency close to 10%. Since there is no need for the extremely high power green laser for the self-trapping experiments, we adopted the 500 mW 808 nm LD as the pump, with the highest green output of 47 mW, which is sufficient for the high intensity regime of photopolymerization study. The TEC was set to 22 °C for the duration of the experiments.

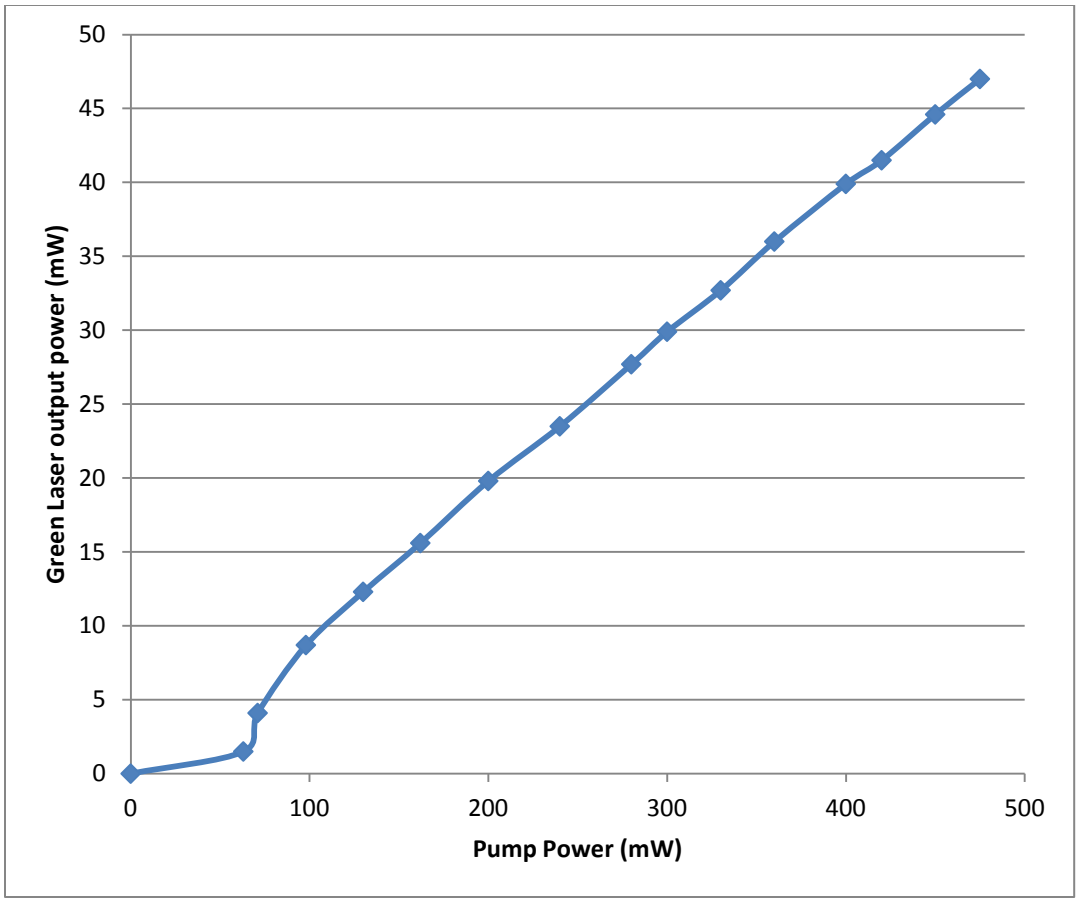

Figure 3.5 Power of green laser output verses pump power of 808 nm Laser Diode

3.3 Preparation of Photosensitive Organosiloxane

The photosensitive organosiloxane is prepared by condensation of 3-(trimethoxysilyl) propyl methacrylate (MAPTMS) and hydrochloric acid. MAPTMS was obtained from Gelest Inc. (PA, USA) and 0.1 N standard HCl aqueous solution was obtained from Sigma-Aldrich, Canada. A solution of hydrochloric acid (0.55g of 0.05 N diluted from 0.1 N standard) was added to MAPTMS (8.8 g). A homogenized transparent fluid was obtained after stirring the

mixture for 2 minutes. After the addition of free-radical photo-initiator (0.048 g ,Ciba Specialty Chemicals Inc., Canada), the sol becomes photosensitive to visible light. Wrapped with aluminum foil, the sol was stirred for 5 days then filtered through a polytetrafluoroethylene (PTFE) membrane (0.2 μm pore size, Pall Corporation, USA) before used.

A custom-made cylindrical cell was prepared from a commercially available plastic ring (Delrin) and microscope cover slips. One cover slip (25 × 25 mm) was glued to each end of the plastic ring (length 6 mm, external diameter 16 mm). The two microscope cover slips create parallel transparent windows with a fixed separation of 6 mm.

For the process of pre-polymerization of the self-trapping experiment, the photosensitive organosiloxane sol (*ca.* 1.8mL) was injected into the cylindrical cell. By use of a quartz-tungsten-halogen lamp (Cole-Parmer ,j09790-series, IL, USA) operating at 3 mW, the organosiloxane sol was uniformly irradiated through the glass windows for 2 minutes in each direction. Through this process, the sol became partially polymerized, which transformed the sol into an orange gel that was unable to flow.

3.4 Optical Set-up

In order to observe the non-linear phenomena in the photopolymerizable material, the 2-D spatial intensity images of the exit beam are to be collected at the

exit face of the sample cell. A schematic of the optical set-up for the one-beam self-trapping in the organosiloxane is given in Fig 3.6, and a photograph of the set-up is given in Fig 3.7. The light source used was a miniature green laser emitting TEM_{00} mode continuous wave at 532 nm. The output beam power could be increased up to 40 mW. By adjusting the intensity to the desired amount, the beam could be focused with a planoconvex lens (L1, F.L. = 75.6 mm) onto the entrance face of the organosiloxane sample cell (S) with a diameter *ca.* 20 μm. The sample cell was mounted on a custom-made sample holder which could be finely adjusted along the beam direction with a resolution of 0.5 μm. The cross-sectional intensity profile of the beam at the exit face of the sample cell was focused onto a high-resolution CCD camera (738(H) × 484(V) pixels, pixel size 4.80 μm(H) × 5.58 μm(V); LaserCam IIID ¼", Coherent Inc., CA, USA). Before entering the camera, the beam was focused with a set of planoconvex lenses (L2, F.L.= 100 mm, and L3, F.L.= 300 mm) and reduced in intensity by a set of neutral density filters (F) that are mounted on three separate rotatable wheels (VARM, Coherent Inc., CA, USA). The CCD camera was operated using BeamView Analyzer software (version 3.2) that provided the specification of the beam: the beam diameter (Full Width at Half Maximum (FWHM), $1/e^2$), the relative peak intensity. BeamView Analyzer was able to generate 2D and 3D intensity profiles and compensate for the magnification caused by the planoconvex lenses L2 and L3. All the optical components were mounted on carriers to ensure their alignment.

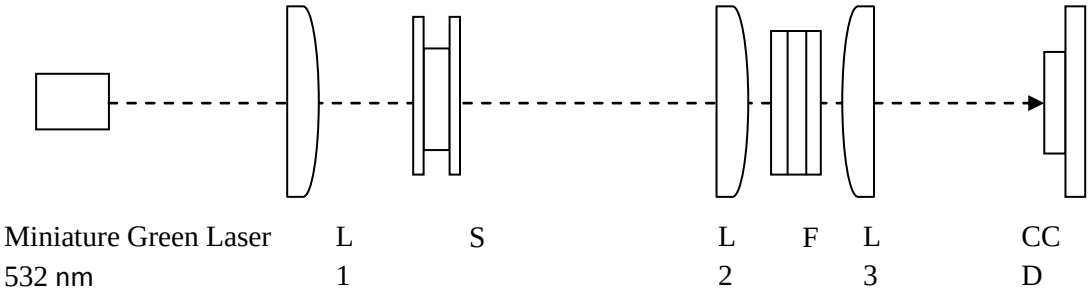

Figure 3.6 Optical Set-up of the self-trap study on one beam in the organosiloxane.

The miniature green laser emitted 532 nm beam was focused with a lens (L1) onto the organosiloxane sample (S) and imaged at the exit face into a CCD camera with two planoconvex lens (L2 and L3) and a set of neutral density filters (F) which is positioned in between them.

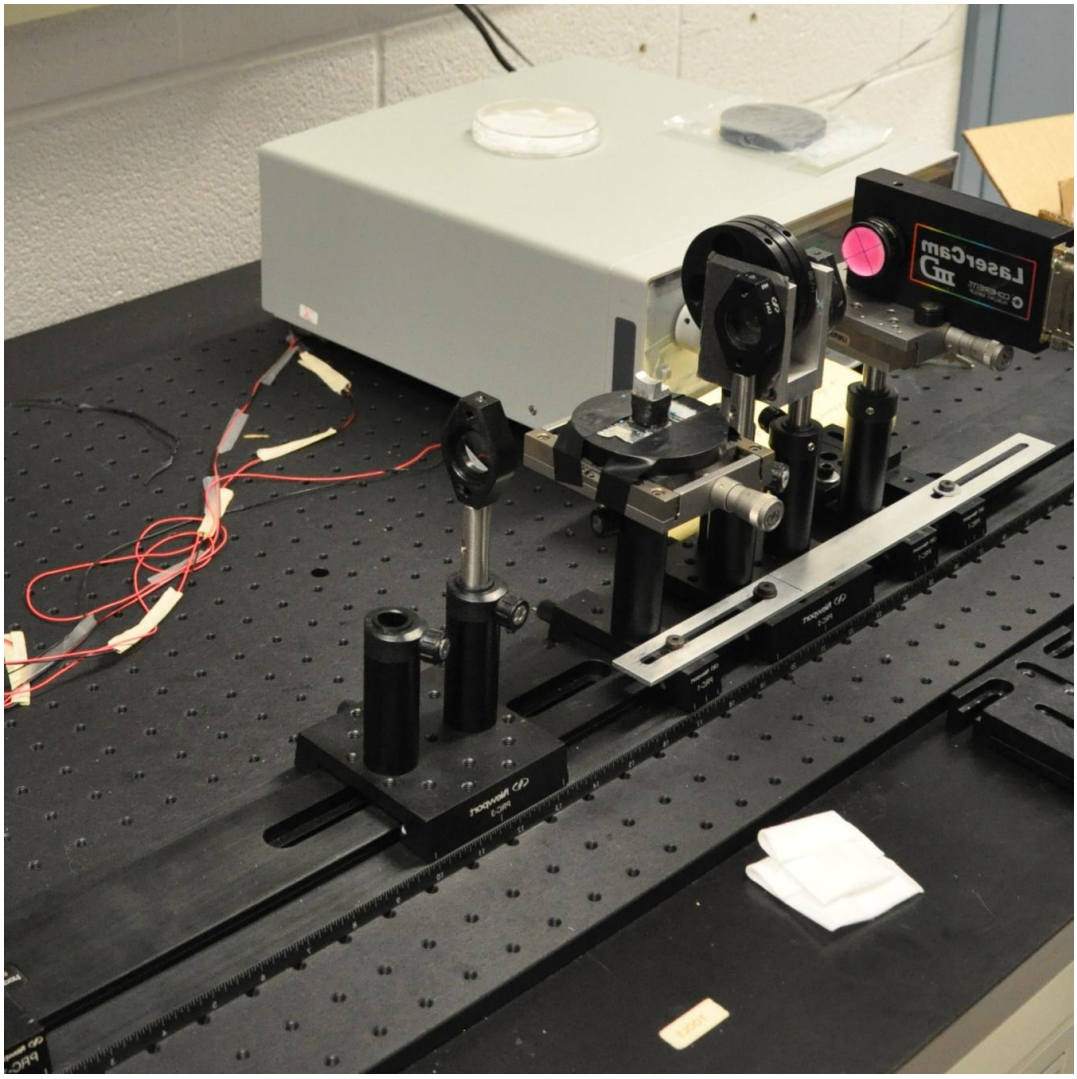

Figure 3.7 Photograph of the real optical set-up for one beam self-trapping experiment.

For the two beam interaction experiment, the optical set-up was very similar to the one beam experiment, except for the addition of a pinhole array before the planoconvex lens (L1). The pinhole array sets consisted of two pinholes of diameter 50 μm and spacing 200, 500 and 1500 μm between the two holes respectively. A

schematic for the optical set-up for two-beam interaction experiment is given in Fig 3.8 and a photograph of the set-up is given in Fig 3.9.

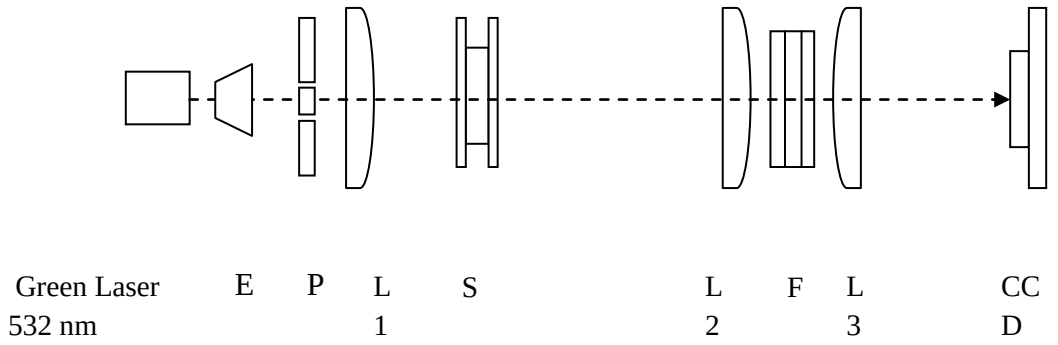

Figure 3.8 Optical Set-up of the two beam interaction study in the organosiloxane.

The miniature green laser emitted a 532 nm beam which was expanded by a beam expander (E). The beam was split at the pinhole array (P), the beams were focused with a lens (L1) onto the organosiloxane sample (S) and imaged at the exit face into a CCD camera with two planoconvex lens (L2 and L3) and a set of neutral density filters (F) which was positioned between them.

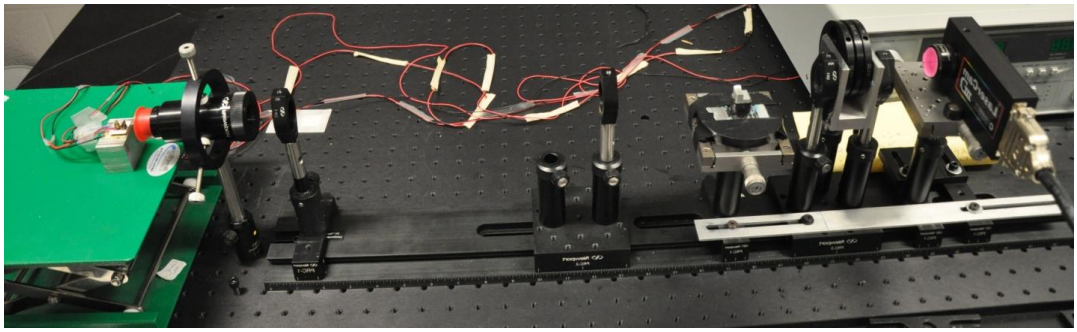

Figure 3.9 Photograph of the optical set-up for the two-beam experiments

The study of the one beam self-trap within the organosiloxane material induced by the light of 532 nm required the adjustment of the input beam intensity. The laser was tuned to a large range of powers and measured after the planoconvex lens L1 immediately before the entrance face of the sample. A measurement was taken with a power meter (FieldMaster, Coherent Inc., CA, USA) with a silicon detector (LM-2-VIS, Coherent Inc., CA, USA), which had a measurement range of 10 nW to 50 mW in power and 0.4 μm to 1.06 μm in wavelength. The intensity of the focused beam before the entrance face of the sample is shown in Table 3.2, calculated with the equation of $4P/\pi d^2$, where d is the value of the diameter of the focused beam measured by the CCD camera.

Intensity ($W\ cm^{-2}$)	Power (W)	Absorption Filter No.1	Absorption Filter No.2	Absorption Filter No.3	CCD Filter (O.D.)
3.2×10^{-5}	1×10^{-10}	1.00	1.00	1.00	0.5
1.92×10^{-4}	6×10^{-10}	1.00	1.00	1.00	0.5
0.0032	1×10^{-8}	1.00	1.00	0.071	0.5
0.008	2.5×10^{-8}	0.001	1.00	0.084	0.5
0.0192	6×10^{-8}	1.00	1.00	1.00	3.47
0.192	6×10^{-7}	1.00	1.00	1.00	3.47
1.6	5×10^{-6}	1.00	0.021	0.06	3.47
16	5×10^{-5}	0.001	0.035	0.06	3.47
32	1×10^{-4}	0.001	0.035	0.084	1.3
64	2×10^{-4}	0.010	1.00	0.084	1.3
80	2.5×10^{-4}	0.001	0.021	0.084	1.3
95	3×10^{-4}	0.1	0.021	0.06	1.3
159	5×10^{-4}	0.001	0.035	0.06	3.47
1592	5×10^{-3}	0.1	0.021	0.071	3.47
6368	2×10^{-2}	0.1	0.06	0.06	3.47

Table 3.2 The intensity range of the focused beam at the entrance face of the sample with the corresponding filters and neutral density filter adopted to attenuate the light before it enters the CCD camera. The combination was made of three filters that are labeled with the value of transmittance and the CCD filter is labeled with the Optical Density (O.D.).

The experiments were performed under different regimes of intensity that can be classified into three categories: low intensity regime, medium intensity regime and high intensity regime.

The self-trapping structures within the organosiloxane sample were characterized by use of reflection optical microscopy (BX51, Olympus Corp, Tokyo, Japan) and transmission optical microscopy (SteREO Discovery. V12, maximum magnification 400x, Carl Zeiss Ltd. Germany). In order to prevent the sample from further polymerization which would damage the self-trapping structure, a red filter was adopted in the white light path.

Chapter 4 FORMATION AND EVOLUTION OF A SELF-TRAPPED BEAM OF LASER LIGHT IN A PHOTOPOLYMERIZABLE MEDIUM

4.1 Introduction

As introduced in chapter 1, based on the theoretical analysis of the self-trapping beams in photopolymerizable material (103-105), some phenomena are expected to be observed. These include: the formation of the multimode waveguide as the beam self-traps as it propagates through, the evolution of the refractive index change, and the excitation of the high-order modes. Previous research into self-trapping has mainly focused on the formation of the waveguides by the propagation of the beam in different types of media such as epoxy resins (106). Other studies have been done in specific fields including: the spectroscopic monitoring of the formation of the waveguide induced by visible light (107), the introduction of beam filamentation within the waveguide when the intensities reach a certain point (108-109), and interactions of the waveguides in photopolymerizable resins (110). Different types of applications for the self-trap waveguides have also been proposed. Sugihara et al have proposed the application of the single-mode interconnects (111); Yamashita et al have proposed multimode interconnects (112), Yamashita et al have proposed the fiber interconnects (113), and Yonemura et al have proposed wavelength division multiplexers (115). Research into complicated self-written structures has also attracted considerable interest. To date, studies on waveguide

arrays with VCSEL (116), high-order modes on fiber end (117), and artificial compound eyes (118) have been reported. In summary, the research mentioned here demonstrates the self-trapping of both (1+1)D and (2+1)D in photopolymerizable materials.

The main focus of this chapter is the temporal evolution of the self-trapped beam and the analysis of the dynamics over a broad range of the incident beam intensities over 8 orders of magnitude (from 3.2×10^{-5} W cm^{-2} to 6368 W cm^{-2}). By employing a high resolution CCD camera (738(H) × 484(V) pixels, pixel size 4.80 μm(H) × 5.58 μm(V)), it was possible to profile the beam characteristics with visual pictures and measure the change quantitatively at the exit face of the organosiloxane sample.

The chapter includes a detailed analysis of the formation of high-order modes as the beam self-traps at the intensity of 1.92×10^{-2} W cm^{-2}; the trends of the intensity-dependence of self-trapping based on the spatial profiles at the entire range of intensities; and the summary of the single-beam self-trapping in the photopolymerizable organosiloxane.

4.2 Self-Trapping

In this section, a typical self-trapping of one beam experiment is demonstrated. A Gaussian beam at 532 nm with the average intensity of 1.92×10^{-2} W cm^{-2} was focused at the entrance face of the custom-made cylindrical sample cell

containing the photopolymerizable organosiloxane. The refractive index of the organosiloxane is 1.47, with the linear situation, the beam diffracts along both of the transverse directions. As the beam was focused at the entrance face of the sample cell with a focal width of 20 μm, the beam width would diffract to 118 μm as it propagates 6 mm from the entrance face to the exit face of the medium if there's no refractive change in the organosiloxane. However, the organosiloxane is photosensitive due to the addition of photoinitiator, it can have a maximum refractive index change of Δn_s~0.006 (101). Due to the refractive index change induced by the incident beam, the beam self-traps as it propagates without diffracting in the medium.

The 2-D intensity profile of the beam at the exit face was monitored by the high resolution CCD camera, and a typical profile of the beam without going through the sample is shown in Fig. 4.1.

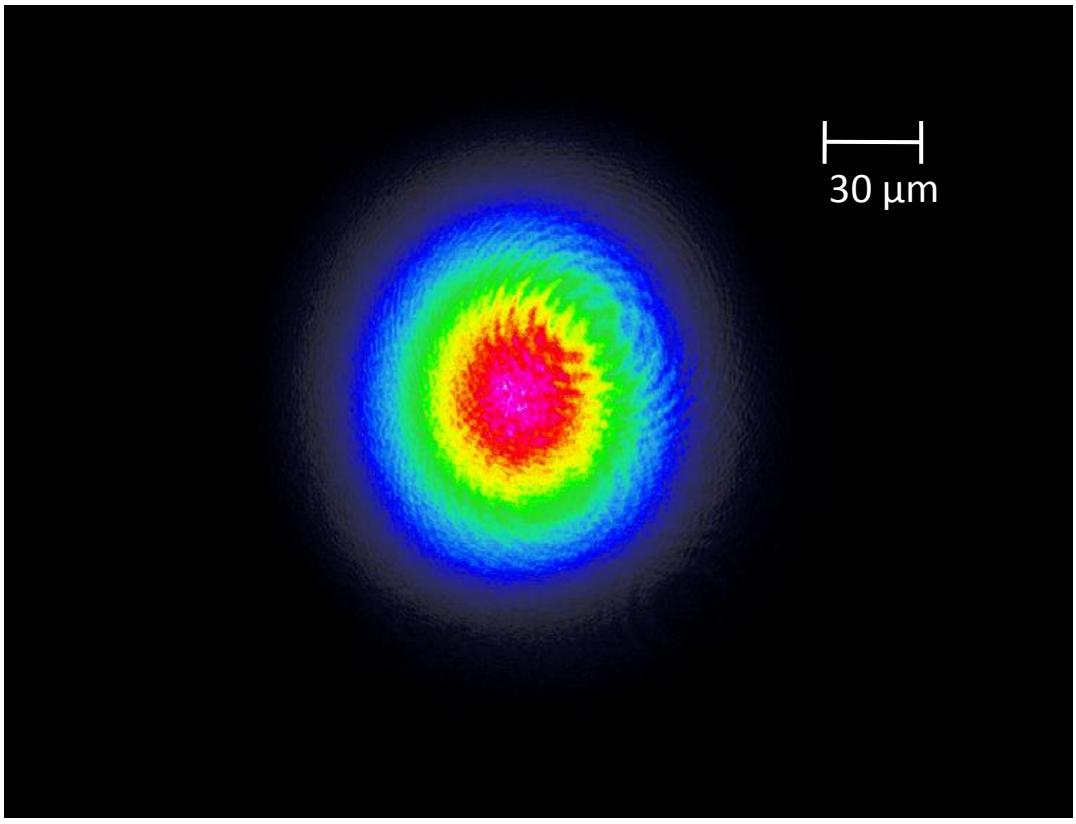

Figure 4.1 2-D beam profile at the exit face of the sample cell without going through the organosiloxane with the beam intensity of $1.92 \times \mathbf{10^{-2}}$ W cm^{-2}

The temporal evolution of 2-D intensity of the beam profile at the exit face is shown in Fig 4.2. The beam started to self-trap immediately after the organosiloxane was exposed to the green laser beam. The beam size at the exit face shrunk continually to an irregular form in 23 seconds with a core of high intensity, showed at Fig 4.2 (b). After 53 seconds (Fig 4.2 (c)) of self-trapping, the beam became as small as about one tenth of the size of the initial size, and it self-trapped to a single LP_{01} mode beam from 60 seconds (Fig 4.2 (d)) to 72 seconds (Fig 4.2 (e)). At 72 seconds, the beam had a minimal diameter of 15 µm, and the average

intensity became as high as 2.06 mW cm^{-2}. Compared to the diffracted beam with a diameter of 118 μm, the beam self-trapped to one eighth in its diameter which shrunk to as small as about 15 μm and remained in that size for about 15 seconds. High-order mode started to form after 87 seconds (Fig 4.2(f)), and as the complex multi-mode evolved from 96 seconds (Fig 4.2(g)), the diffraction rings started to form and were very clearly observed at 226 seconds (Fig 4.2(i)). The self-trap beam evolved till *ca.* 250 seconds after the beginning of the experiment, exhibiting complementary oscillations in relative peak intensity and effective beam diameter as shown in Fig 4.3. The modes observed during the self-trapping of the beam are identified by comparing to the linear polarized, high-order mode of passive cylindrical waveguides. After 96 seconds, the beam profile shows that the modes that are difficult to resolve, however, the beam remained self-trapped and did not change back to the diffracting form.

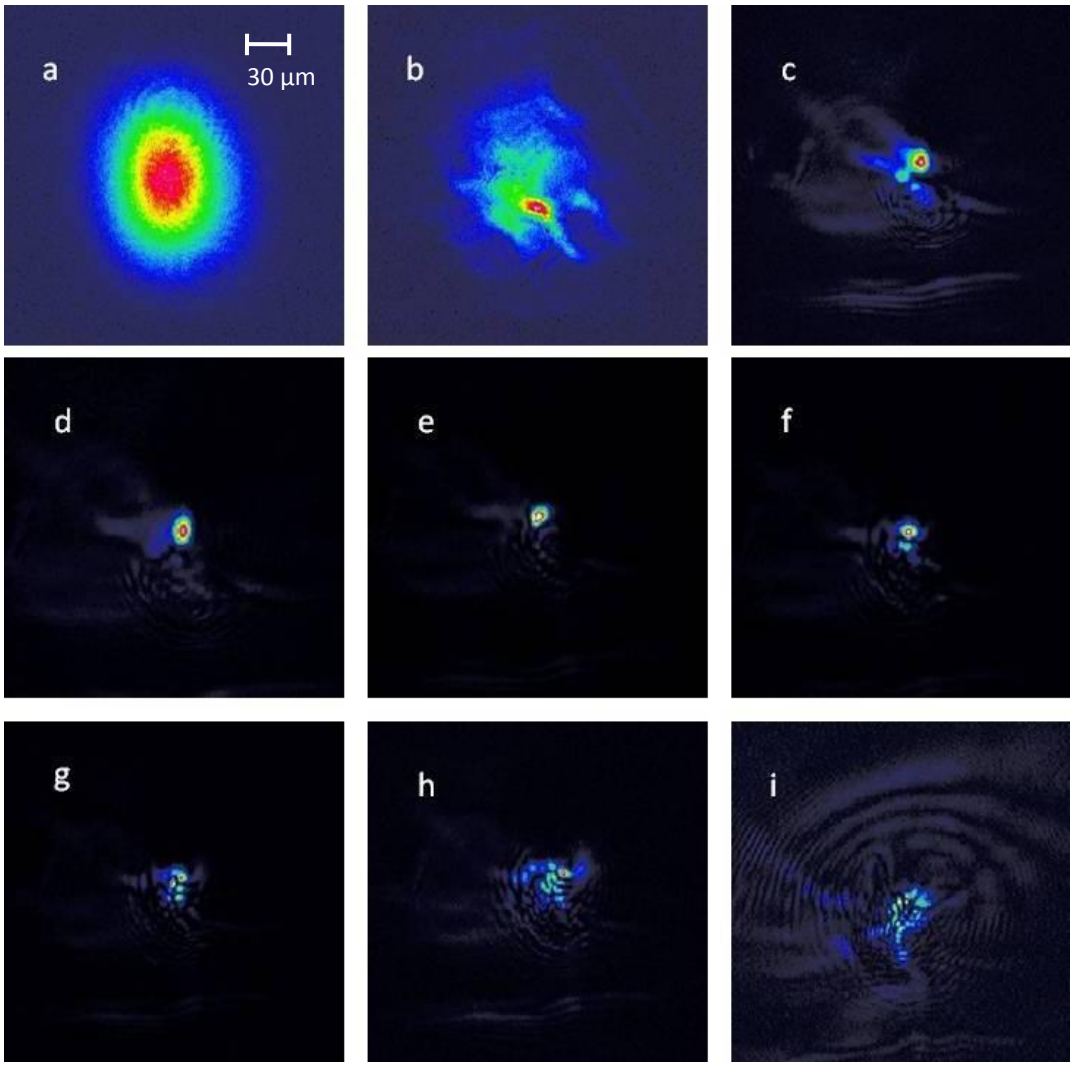

Figure 4.2 Temporal evolution of the 2-D (and 3-D) spatial intensity profiles of the beam at the exit face of the sample cell as the beam self-traps in the organosiloxane with the average intensity of $1.92\times\mathbf{10^{-2}}$ W cm^{-2}, profiles were acquired at (a) 0 s, (b) 23 s, (c) 53 s, (d) 60 s, (e) 72 s, (f) 87 s, (g) 96 s, (h) 104 s, (i) 226s.

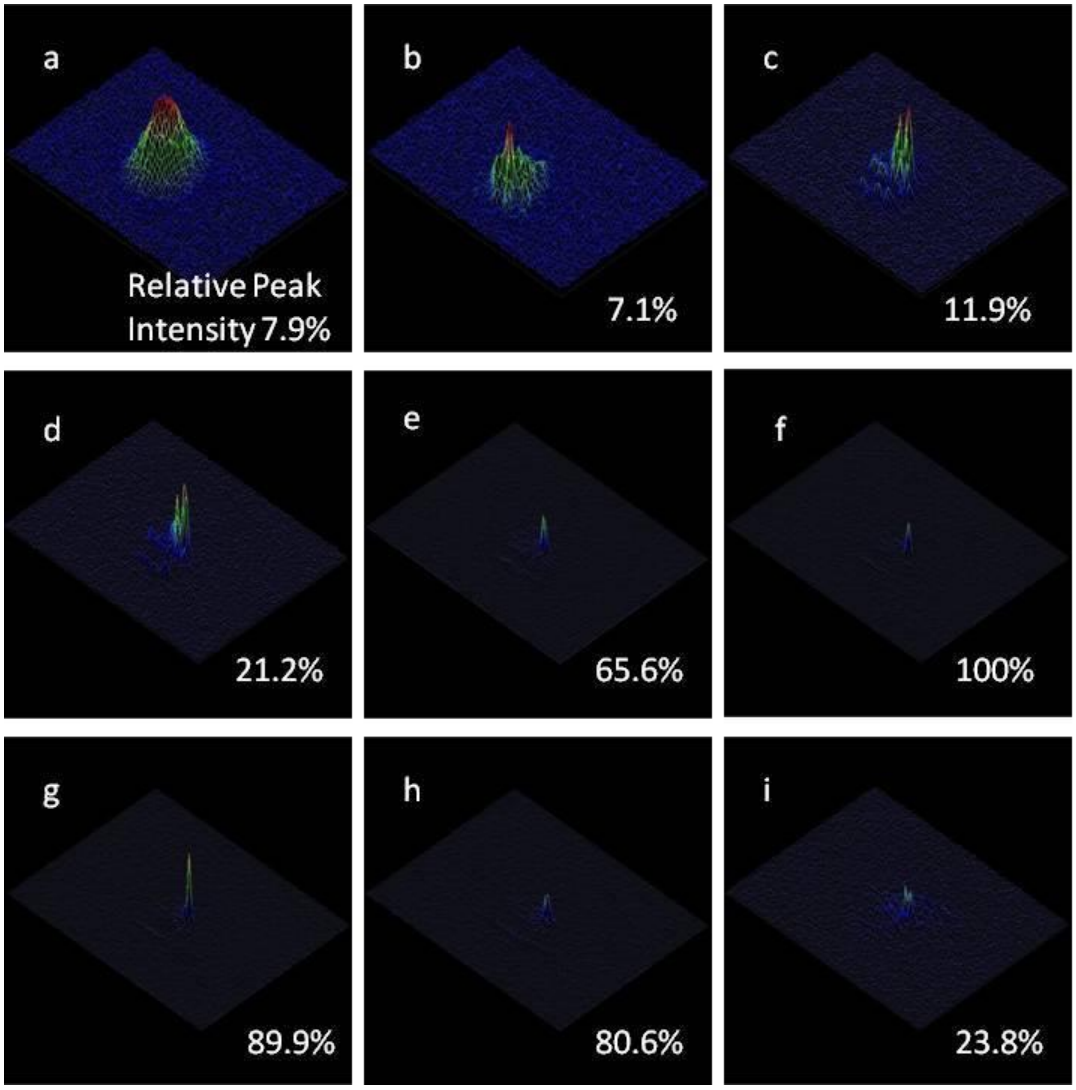

Figure 4.2 (Continues) Temporal evolution of the 2-D (and 3-D) spatial intensity profiles of the beam at the exit face of the sample cell as the beam self-traps in the organosiloxane with the average intensity of $1.92\times\mathbf{10^{-2}}$ W cm^{-2}, profiles were acquired at (a) 0 s, (b) 23 s, (c) 53 s, (d) 60 s, (e) 72 s, (f) 87 s, (g) 96 s, (h) 104 s, (i) 226s.

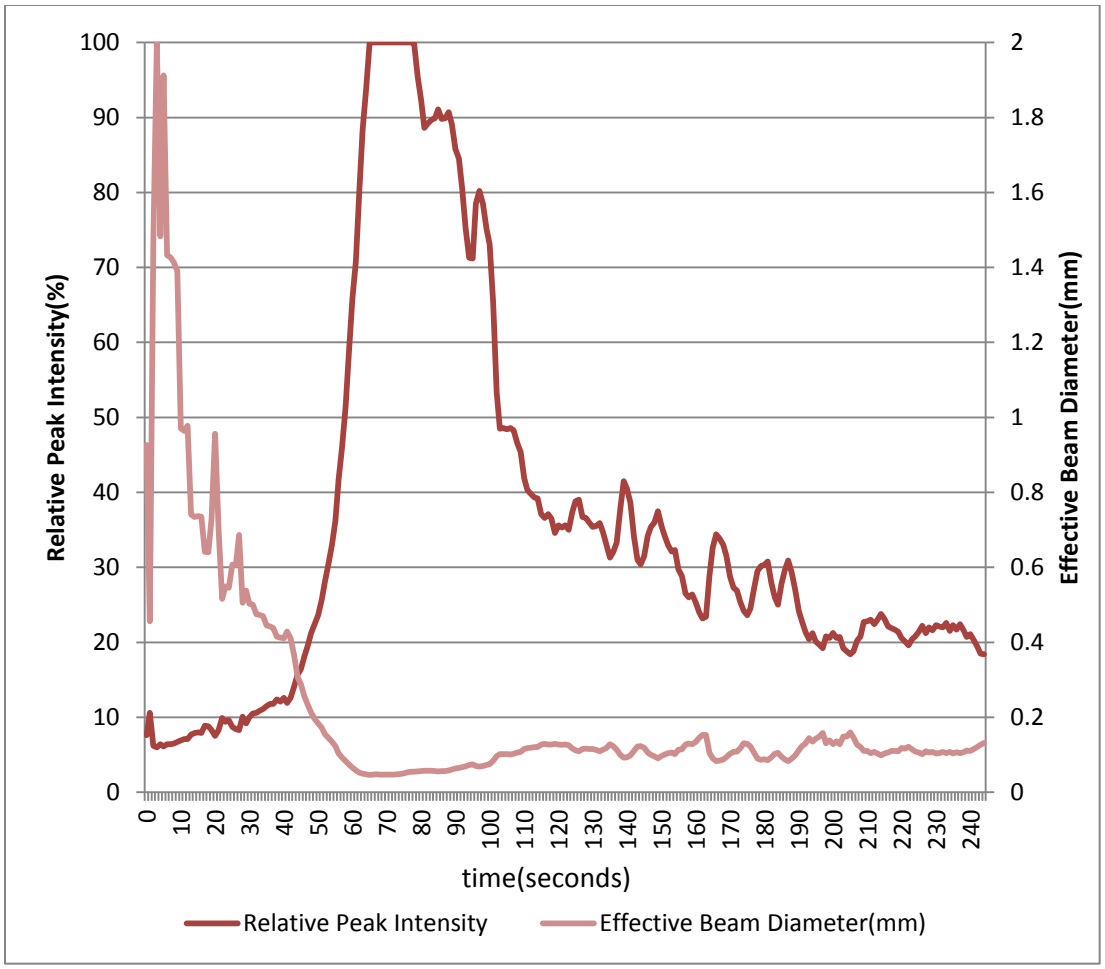

Figure 4.3 Temporal plots of the peak intensity (dark gray line) and effective beam diameter (light gray line) as the green laser beam self-traps in the organosiloxane medium with the intensity of $1.92 \times \mathbf{10^{-2}}$ W cm^{-2}.

The results above agreed with the predictions of theoretical models of self-trapping in photopolymerizable mediums (103), (104), (120), (121), (122). As discussed in chapter 1, the self-trapping phenomena can be understood as the solutions to the nonlinear Schrodinger equation. As a result, the majority of the simulations of light propagation are done based on the Schrodinger equation (70),

(122). According to the model introduced by Monro et al (104), the paraxial wave equation is used to describe the light propagation in the following form:

$$ik_0 n_0 \frac{\partial E}{\partial z} + \frac{1}{2} \nabla_t^2 E + {k_0}^2 n_0 \Delta n E + \frac{i}{2} k_0 n_0 \alpha E = 0 \quad (4.1)$$

Where$k_0 = \omega/c$, is the free space wave number, n_0 is the initial refractive index, and $\Delta n(x, y, z, t) = n - n_0$, while n is the current refractive index and $E(x, y, 0, t) = E_0(-(x^2 + y^2)/a^2)$ is the electric field envelope amplitude, α is the attenuation coefficient of the medium at wavelength λ.

In the Monro model, the simple phenomenological model is used which includes saturation effects, to describe the temporal evolution:

$$\frac{\partial \Delta n}{\partial t} = A(EE^*)(1 - \frac{\Delta n}{\Delta n_s}) \quad (4.2)$$

Where t is the time and Δn_s is the maximum (fixed saturation) value of the refractive index change, and A is a material-dependent parameter, which also changes with the wavelength of the light.

According to Equ. 4.1 and 4.2, the propagation rate is proportional to the intensity(EE^*) and decays as the $\frac{\Delta n}{\Delta n_s} \longrightarrow 1$, and the counterbalance between the natural diffraction (x, y) and the refractive index change (Δn(x, y, z, t)) induced by self-trapping is described as well.

The experimental results demonstrated in Fig 4.2 agreed with the numerical simulation of the beam propagation as it self-traps in the polymer demonstrated in Fig 4.4. (103). The increase of the relative peak intensity and decrease in the

effective beam diameter within the first 65 seconds indicated the self-focusing process and then self-trapping process afterwards in the channel waveguide (103).

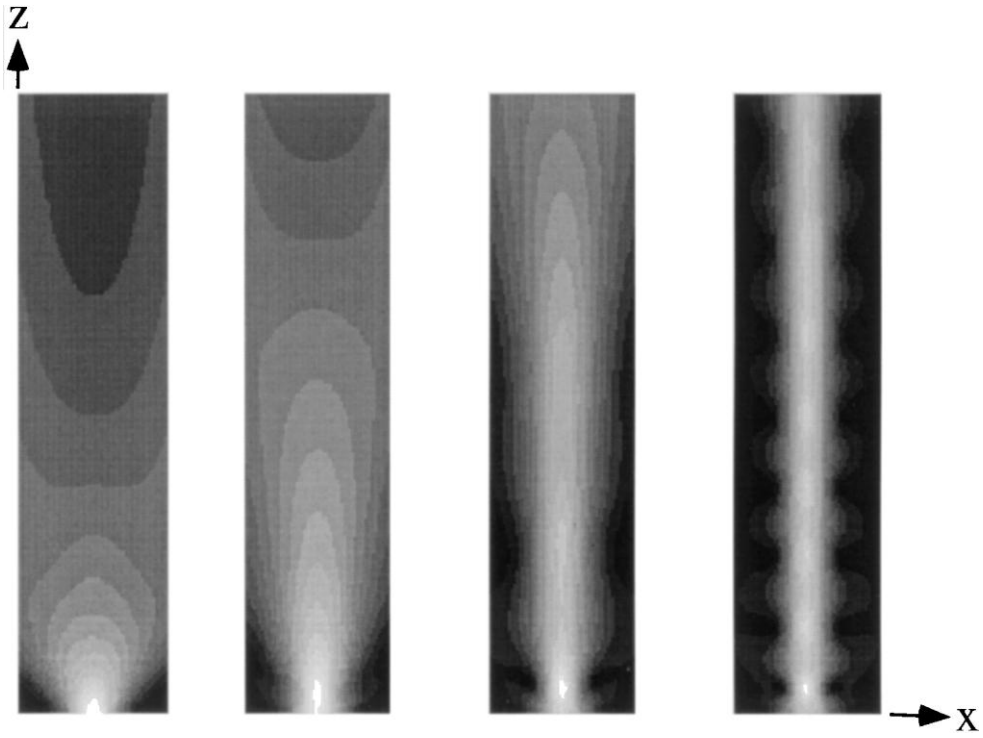

Figure 4.4 Numerical 2D Simulation of the intensity of the self-trapping Gaussian beam propagating in a photopolymerizable medium (103). Reproduced with permission.

In this typical experiment, the intensity of the green light is 60 nW. The average intensity is 1.92×10^{-2} W cm^{-2}. When the beam self-trapped as it propagated through the organosiloxane, different kinds of high-order modes were observed at the exit face of the sample cell (Fig 4.2). There was very clear formation of fundamental LP_{01} mode and superpositions of high-order modes in comparison with the linearly polarized, high-order optical modes of passive

cylindrical waveguides. The results indicated that the beam behaves in correspondence to the linearly-polarized modes in cylindrical waveguides such as in optical fibers (123-125). In both experimental and simulation results, the profiles along the propagation direction (z) did not remain Gaussian but demonstrated multiple lobes. This can be explained as the superpositions of the high-order modes. Unlike other experiments, this experimental design enables the visualization of the spatial intensity and beam shape at the exit face and in situ monitoring of temporal evolution of the beam within the waveguide.

4.3 Intensity Dependence of Self-Trapping

As we discussed in previous section, a typical self-trapping experiment in organosiloxane involved a beam at 532 nm of wavelength and 1.92×10^{-2} W cm^{-2} average intensity. Experiments with a wider range of the beam intensity were examined as well, and as the intensity spanned over 8 orders of magnitude, the average intensities were categorized into three regimes, as indicated in Table 4.1

Intensity Regime	Intensity ($W\ cm^{-2}$)	Power (W)
Low-intensity regime	3.2×10^{-5}	1×10^{-10}
	0.0032	1×10^{-8}
	0.0192	6×10^{-8}
Mid-intensity regime	0.192	6×10^{-7}
	1.6	5×10^{-6}
	16	5×10^{-5}
High-intensity regime	159	5×10^{-4}
	1592	5×10^{-3}
	6368	2×10^{-2}

Table 4.1Category of different regimes of intensity covering 8 orders of magnitude. The left column describes three different regimes, the mid-column describes the average intensity, and the right column describes the magnitude of the power of the beam.

The dynamics of self-trapping within photopolymerizable medium is dependent on the average intensity of the beam according to the theoretical prediction. The change of phenomena include the formation of the diffraction rings

and filamentation at the high intensity regimes, and the change is caused by the change of refractive index which can be described in the following equation (103):

$$\Delta n(x,y,z,t) = \Delta n_s\{1\text{-}\exp[-\frac{1}{U_0}\int_0^{t-\tau}|E(t)|^2 dt]\} \quad (4.3)$$

Where τ is the monomer radical lifetime, Δn_s is the maximum refractive index change, U_0 is the critical exposure required to initiate the photopolymerization, t is time, and $|E(t)|^2$ is the intensity of the incident beam.

Based on Equ. 4.3, the refractive index change increases as the light exposure goes up, until saturation, where the refractive index change reaches to its maximum, namelyΔn_s. No matter in what regime of intensity the beam is, the maximum refractive index change can be achieved at different exposure time. The trend of Equ 4.3 was proposed by Villafranca et al and the illustration of the formation of the lenses at intensities in the low, mid and high-intensity regime was given. (127)

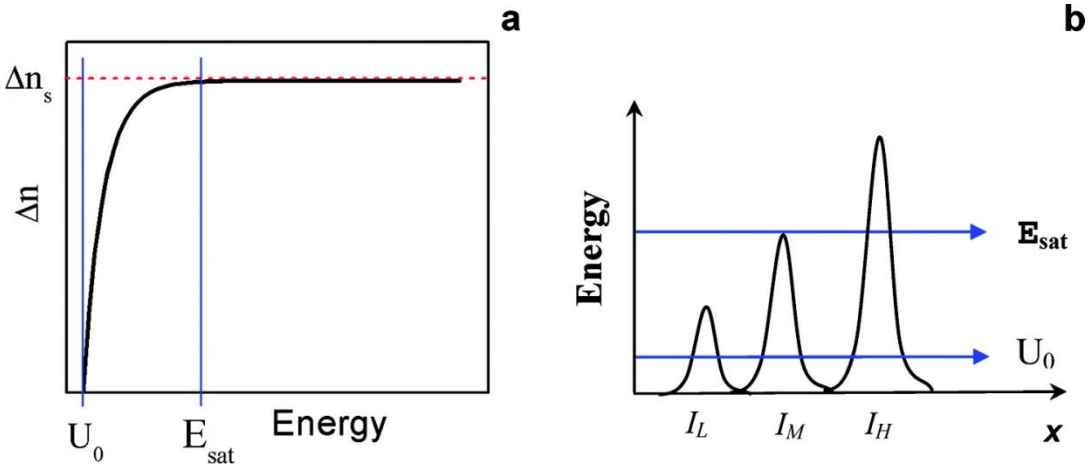

Figure 4.5 (a) Refractive index change as a function to energy. (b) Spatial profile of the Gaussian beam and the optical after 1 second of exposure. U_0 is the critical

exposure required for photoinitiation, E_{sat} is the energy required to achieve maximum refractive index change, and Δn_s is the refractive index change at saturation (127). Reproduced with permission.

Because of the intensity dependence of the difference in self-trapping phenomena caused by the difference of refractive index changes, different parameters were examined with different intensity, the parameters include: self-focusing time, self-trapped beam diameter and beam profile.

The self-focusing time is defined as the time from the start of the exposure of light to the first exhibition of significant narrowing of the beam. As shown in Fig 4.3, the beam profile exhibits the steep decrease in its size and the peak intensity increases as a result during the self-trapping. A plot of the self-focusing time against initial intensity is shown in Fig. 4.8. The plot is approximately parabolic in its shape, with the minimum of 15 seconds at the average power of 0.008 W cm^{-2}.

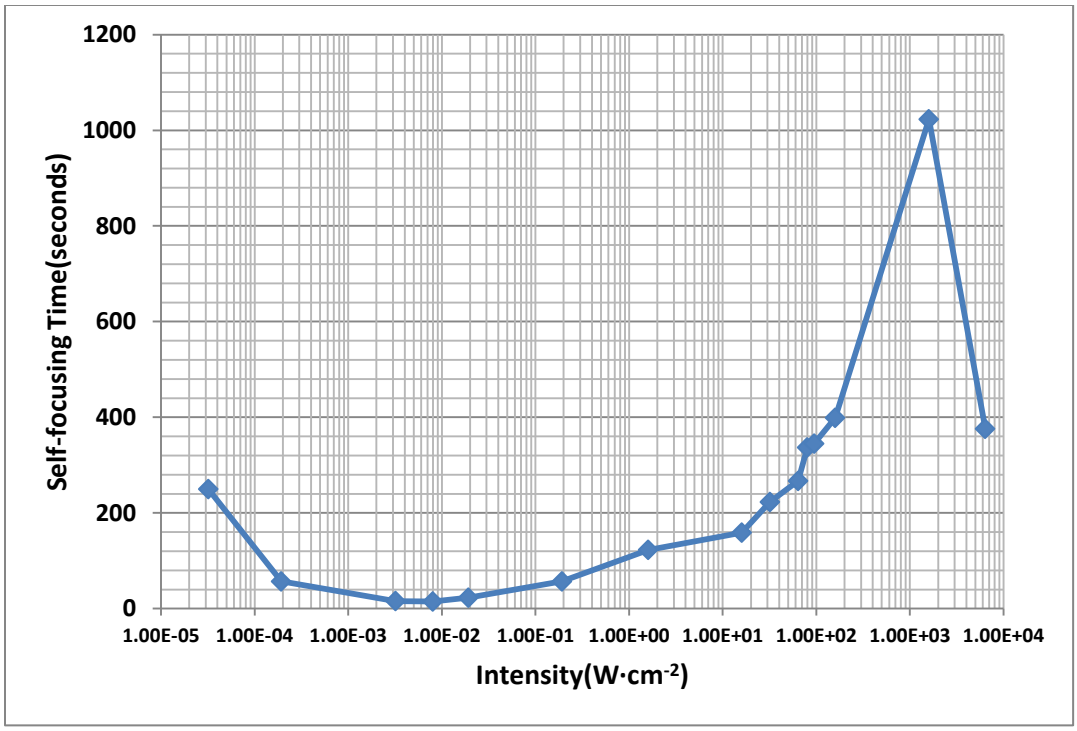

Figure 4.6 Plot of the self-focusing time against the average intensity of the incident beam

As indicated Fig 4.6, the self-trapping time decreases as the average intensity of the incident beam goes up in the low-intensity regime. After reaching the minimum value at 0.008 W cm^{-2}, the self-trapping time increases along with the increase of the average intensity, and the time decreases again at the maximum average power of 6368 W cm^{-2}. Due to the refractive index change induced by the self-focusing beam at the entrance of the medium, the refractive index change has its own Gaussian profile. The lens would have the maximum possible refractive index (Δn_s) at the axial region of the lens, and a symmetric decay in the refractive index till the end. For low intensity light exposure, it takes longer ($t >> \tau$) to achieve

Δn_s at the axial region of the beam according to Equ 4.3. Because the larger the intensity of the light is, the less time it takes to induce a lens, and the self-focusing time decreases as the beam intensity goes up in the low intensity regime. The trend is the opposite in the mid intensity and high intensity regimes. The reason behind this phenomenon is that the large section of the beam simultaneously achieves saturation, as a result, the maximum refractive index change Δn_s is achieved in a large region, and the lens is not as strong as one with the steep gradient in the low intensity case. Consequently, it takes longer to for the beam to self-focus at high intensity.

A plot of the self-trap beam diameter against the intensity of incident beam is given in Fig 4.8. The plot follows the similar pattern as the self-focusing time plot in Fig 4.7. The self-trap beam diameter decreases from 35 ± 5 μm to 12 ± 4 μm when the intensity of the incident beam increases from 3.2×10^{-5} W cm^{-2} to 0.008 W cm^{-2}. The smallest beam is one tenth the width compared to the diffracted beam. Similarly to the intensity dependence self-focusing time plot, the trend is the opposite in the mid intensity and high intensity regimes, the self-trap beam diameter increases when the intensity of the incident beam goes up. As the intensity reached the maximum of 6368 W cm^{-2} in this experiment, the beam width is 79 ± 40 μm, which is over half of the diffracted diameter. The cause of the above phenomena is the same as that for the trend in the self-focusing time. Due to the mechanism of forming the lens with different index gradients, the focused beam diameter is consequently different.

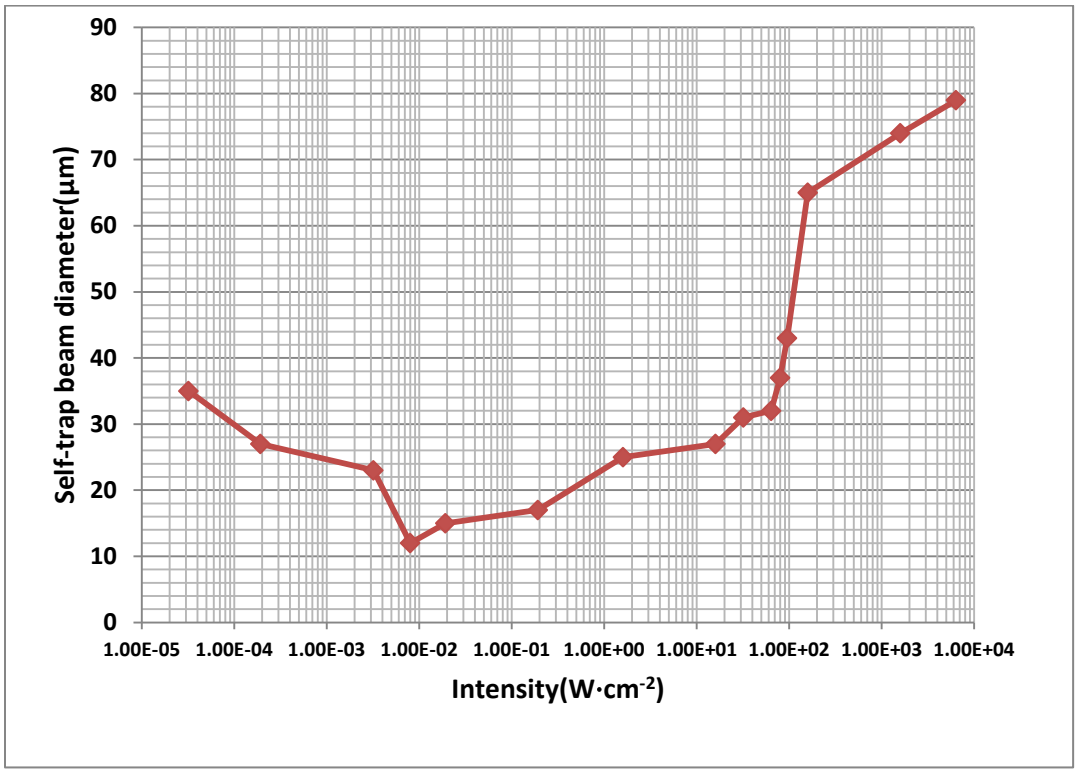

Figure 4.7 Plot of the self-trap beam diameter against the average intensity of the incident beam

The beam profile is different due to the different refractive profile induced in the organosiloxane at different intensities of the incident beam. With the difference in refractive index change (Δn) saturation, different phenomena were observed at the exit face of the sample cell. Different 2-D profiles are presented within different intensity regime.

In the low-intensity regime, the dynamics of self-trapping can be concluded as the sequence of refractive index change, self-focusing, waveguide formation and excitation of high-order modes. Because of the low intensity the

photopolymerizable organosiloxane is exposed to, the refractive index change has a very small value and therefore the waveguides supports fewer modes, compared to the mid-intensity and high-intensity exposed waveguides that support more complicated modes superpositions.

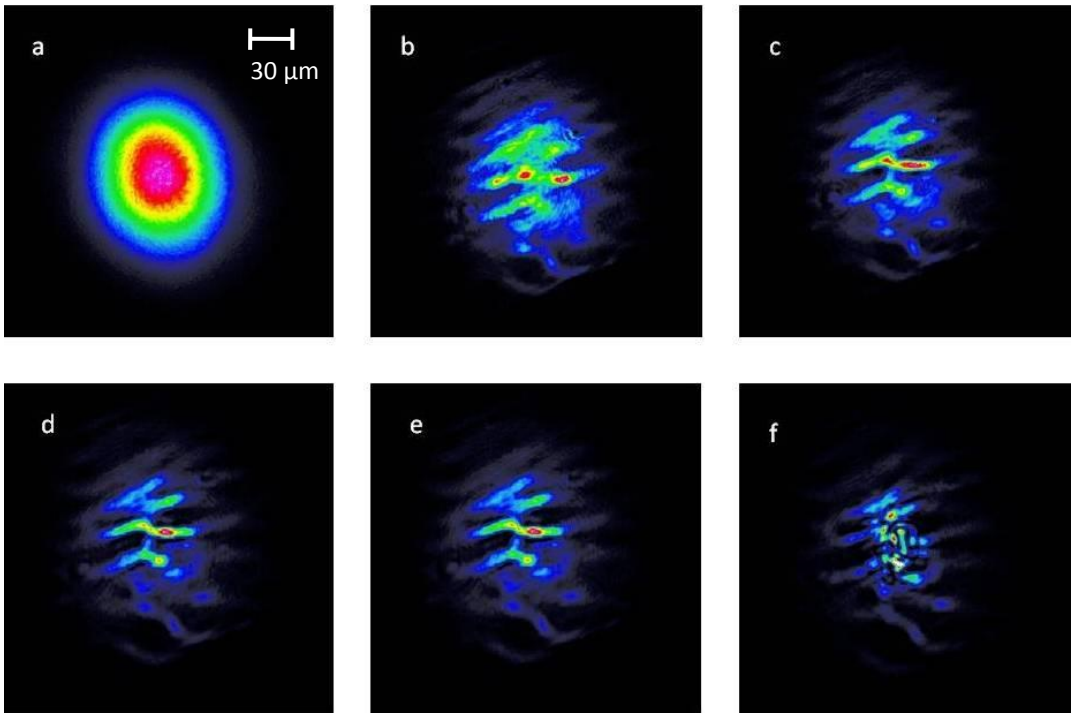

Figure 4.8 Temporal evolution of the 2-D (and 3-D) spatial intensity profiles of the beam at the exit face of the sample cell as the beam self-traps in the organosiloxane with the average intensity of $1.92 \times \mathbf{10^{-1}}$ W cm^{-2}, profiles were acquired at (a) 0 s, (b) 25 s, (c) 57 s, (d) 90 s, (e) 134 s, (f) 243 s

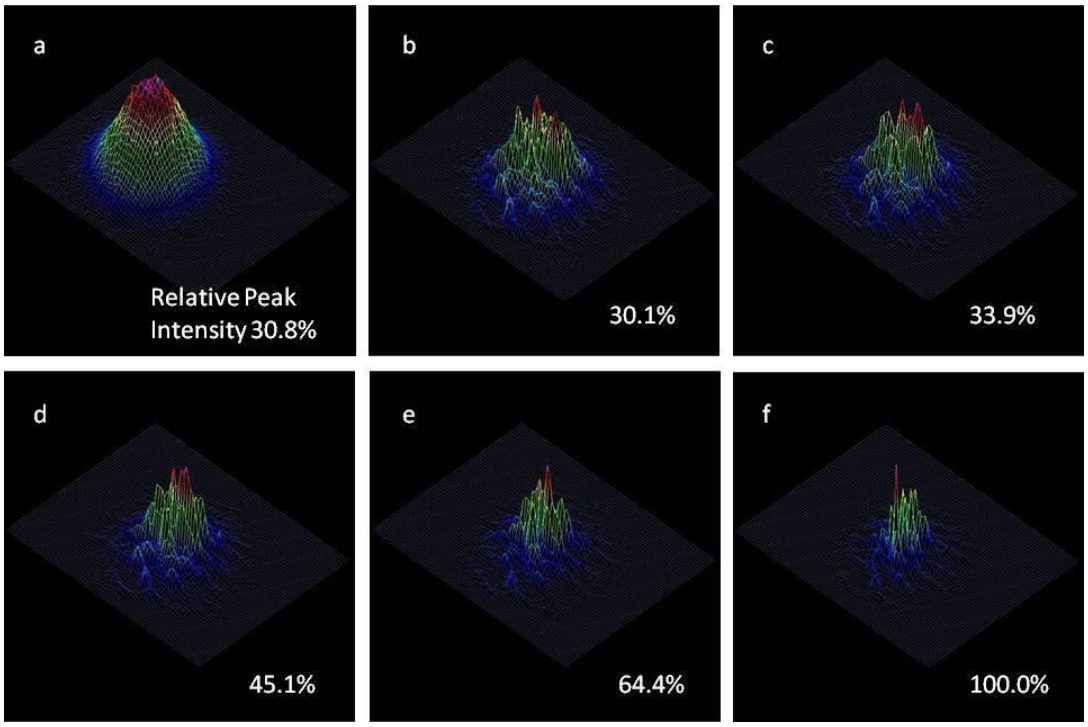

Figure 4.8 (Continues) Temporal evolution of the 2-D (and 3-D) spatial intensity profiles of the beam at the exit face of the sample cell as the beam self-traps in the organosiloxane with the average intensity of $1.92\times\mathbf{10^{-1}}$ W cm^{-2}, profiles were acquired at (a) 0 s, (b) 25 s, (c) 57 s, (d) 90 s, (e) 134 s, (f) 243 s

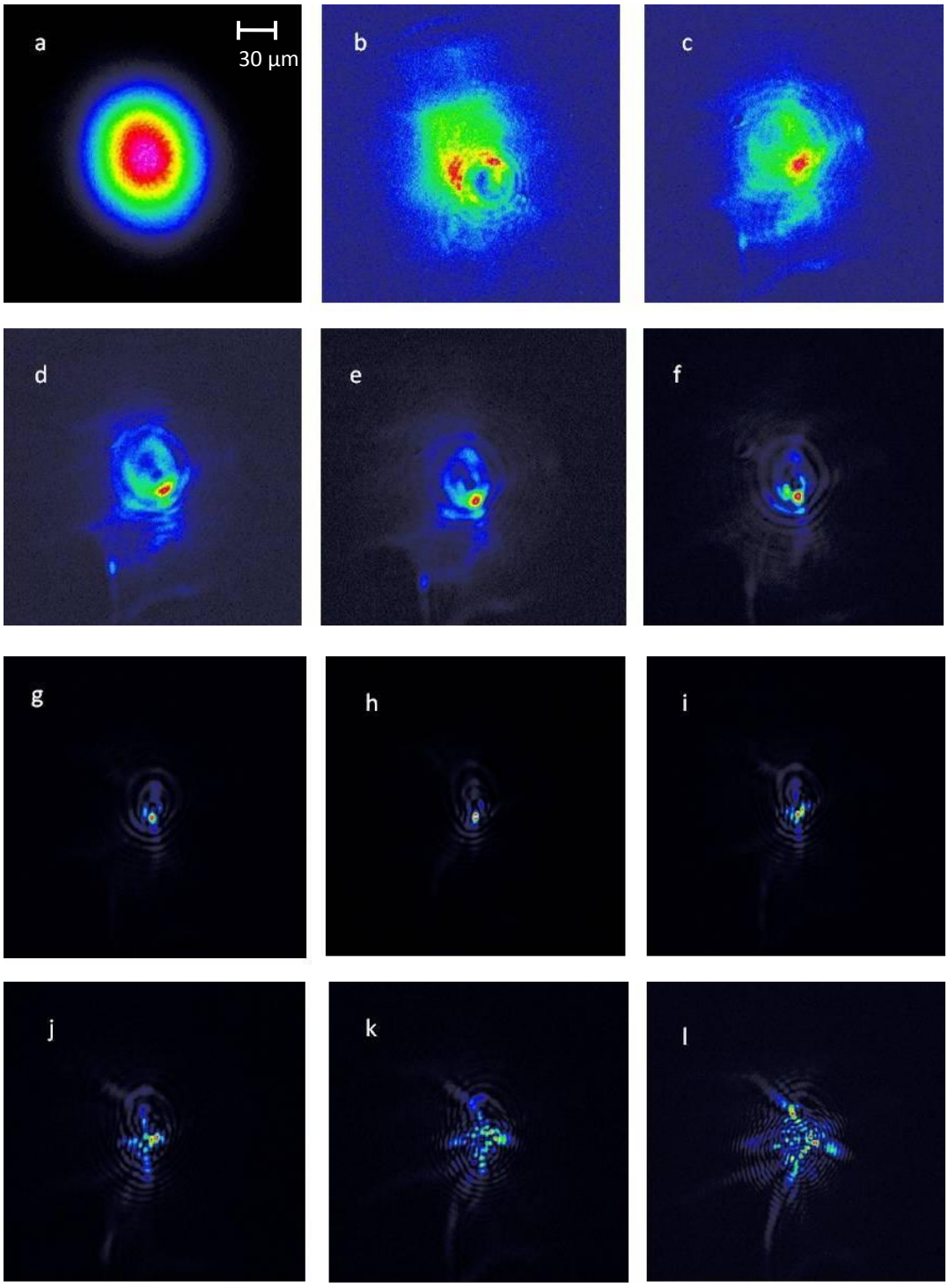

Figure 4.9 Temporal evolution of the 2-D (and 3-D) spatial intensity profiles of the beam at the exit face of the sample cell as the beam self-traps in the organosiloxane

with the average intensity of 1.6 W cm^{-2}, profiles were acquired at (a) 0 s, (b) 9 s, (c) 137 s, (d) 162 s, (e) 197 s, (f) 255 s, (g) 284 s, (h) 309 s, (i) 343s, (j) 377s, (k) 444s, (l) 522 s

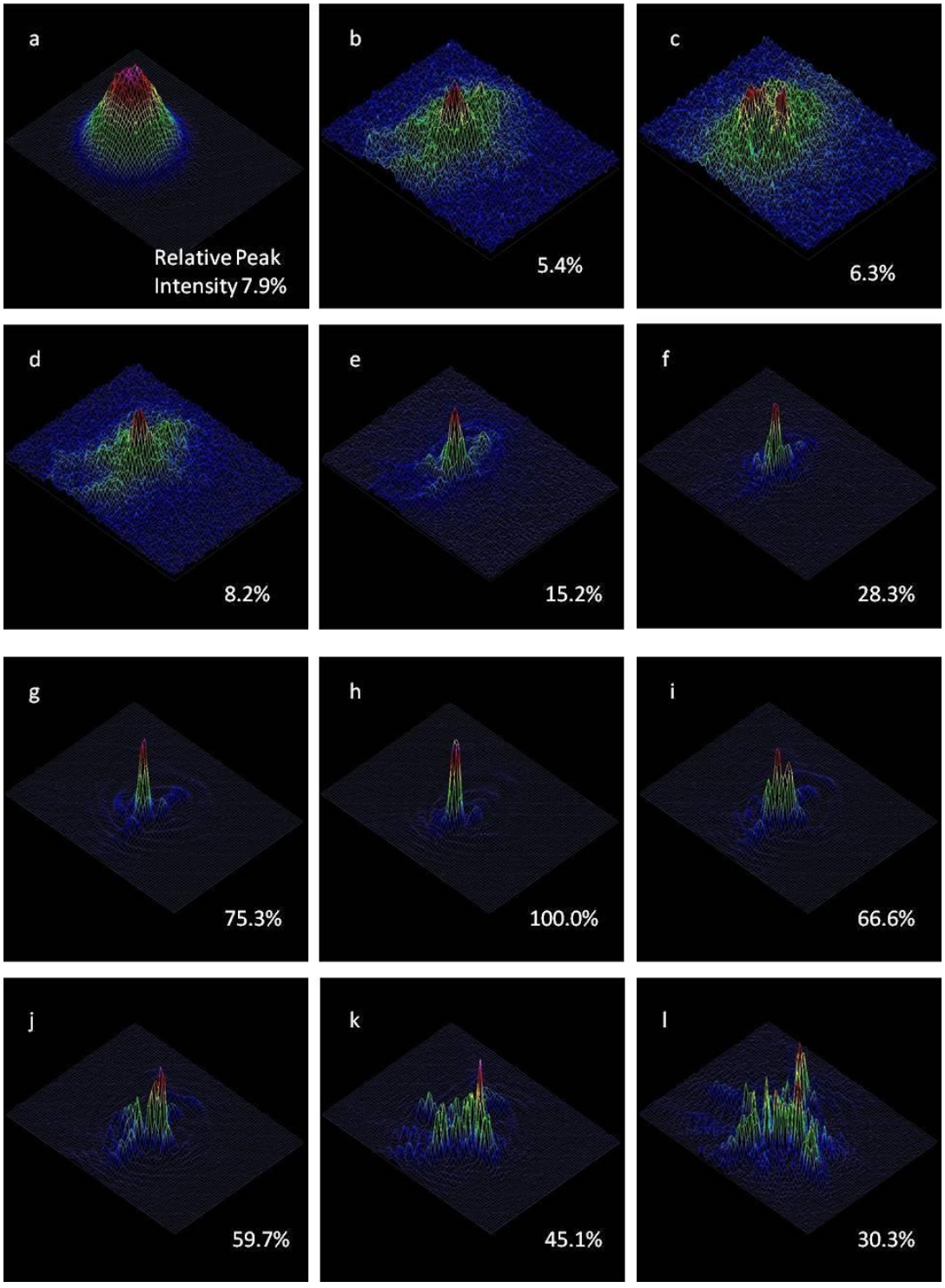

Figure 4.9 (Continues) Temporal evolution of the 2-D (and 3-D) spatial intensity profiles of the beam at the exit face of the sample cell as the beam self-traps in the

organosiloxane with the average intensity of 1.6 W cm^{-2}, profiles were acquired at (a) 0 s, (b) 9 s, (c) 137 s, (d) 162 s, (e) 197 s, (f) 255 s, (g) 284 s, (h) 309 s, (i) 343s, (j) 377s, (k) 444s, (l) 522 s

In the mid-intensity regime, the refractive index changes at a much greater rate, and as a result, the high-order modes are not clearly observable, and the self-trapping time of the beam is noticeably less than that of the low-intensity regime. Essentially, the self-induced waveguides achieve saturation faster in the mid-intensity regime compared to low-intensity regime, and the superpositions of high-order modes can be observed during the process of self-trapping. As shown in Fig 4.8, the temporal plot of the beam profile at the exit face of the sample cell when the incident beam average intensity is 1.92×10^{-1} W cm^{-2}.

When the incident beam intensity increases to 1.6 W/cm^2, a very different phenomenon were observed. The concentric diffraction rings were formed around the self-focused beams as shown in Fig 4.9. The beam developed into concentric rings in 9 seconds after the self-trapping experiment starts, and up to 10 rings were observed during the experiment. The highest intensity examined in this mid-intensity regime was 16 W cm^{-2}, as shown in Fig 4.10. The beam self-focused to superpositions of multiple high-order modes, and no discernible diffraction rings were observed with this intensity.

The concentric rings that have been observed in other nonlinear mediums (such as Kerr media and photorefractive crystals) as the Gaussian beam propagates through, the phenomenon is considered to be self-diffracting effects. The reason the

self-diffracting happens is the spatial self-phase modulation and the as dispersive spatial shock waves that is similar to shock waves in superfluids according to Wan et al from Princeton University (126).

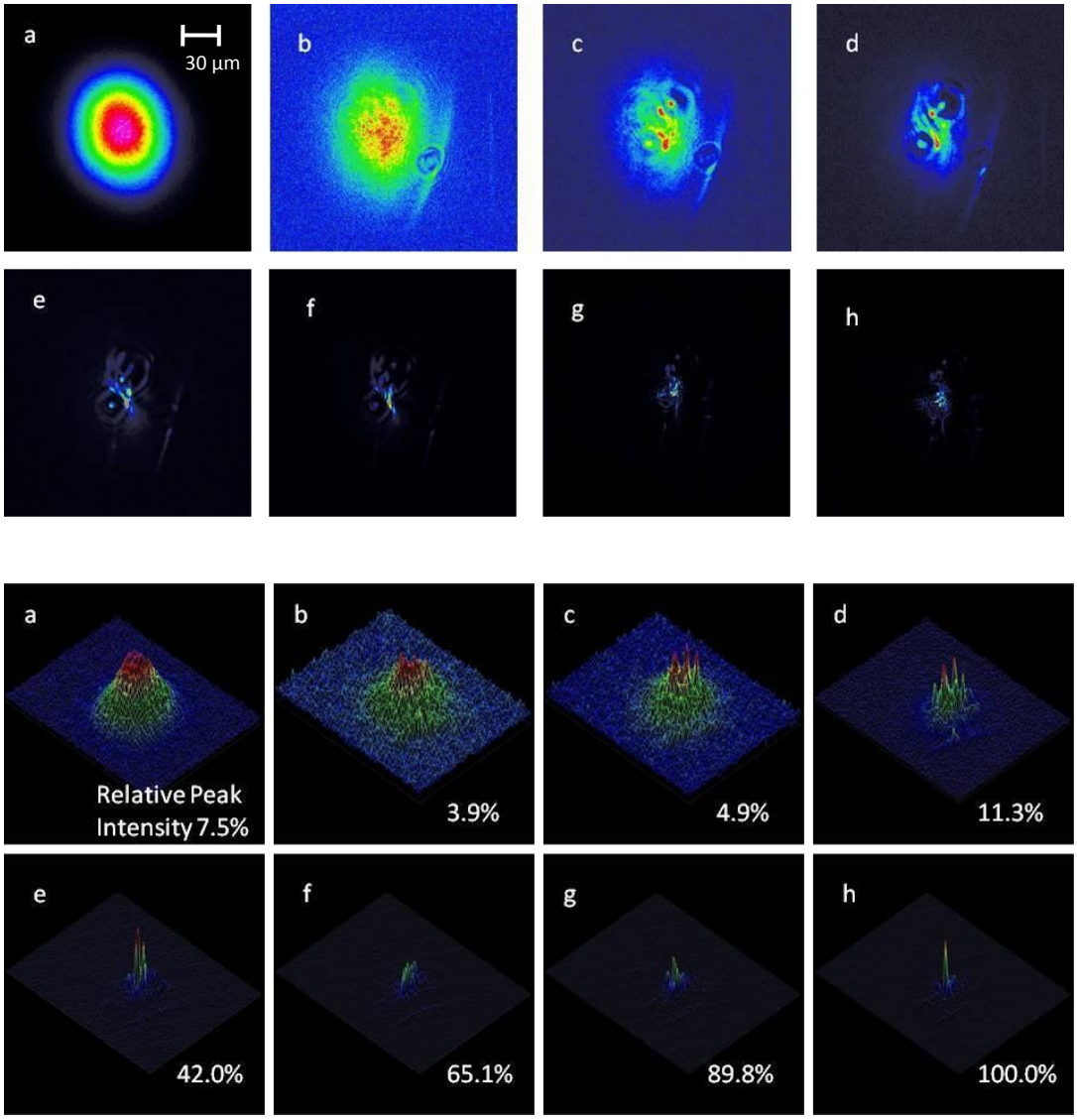

Figure 4.10 Temporal evolution of the 2-D (and 3-D) spatial intensity profiles of the beam at the exit face of the sample cell as the beam self-traps in the organosiloxane

with the average intensity of 16 W cm^{-2}, profiles were acquired at (a) 0 s, (b) 37 s, (c) 54 s, (d) 88 s, (e) 129 s, (f) 172 s, (g) 222 s, (h) 254 s

In the high-intensity regime, the evolution of the 2-D beam profile is very different from that of low-intensity and mid-intensity regime. There is no sharp increase in peak intensity or sudden decrease in effective beam diameter during the self-trapping in the photopolymerizable organosiloxane.

The results of the experiments with high-intensity regime beams are shown in Fig 4.11 and Fig 4.12, with the average intensity of 160 W cm^{-2}, and 1592 W cm^{-2} respectively. As with the 160 W cm^{-2} experiment, the beam self-trapped in an irregular form, resulting in multiple maximum focused dots. As with the 1592 W cm^{-2} experiment, the beam divided into two segments and each later self-trapped respectively at different times. Beam filamentation takes place through a mechanism very similar to the modulation instability in photopolymerizable material. Theoretically, in high-intensity regime, the induced refractive index gradient is not sufficient to support the self-trap of the Gaussian beam, and the noise in the beam becomes filaments after being amplified.

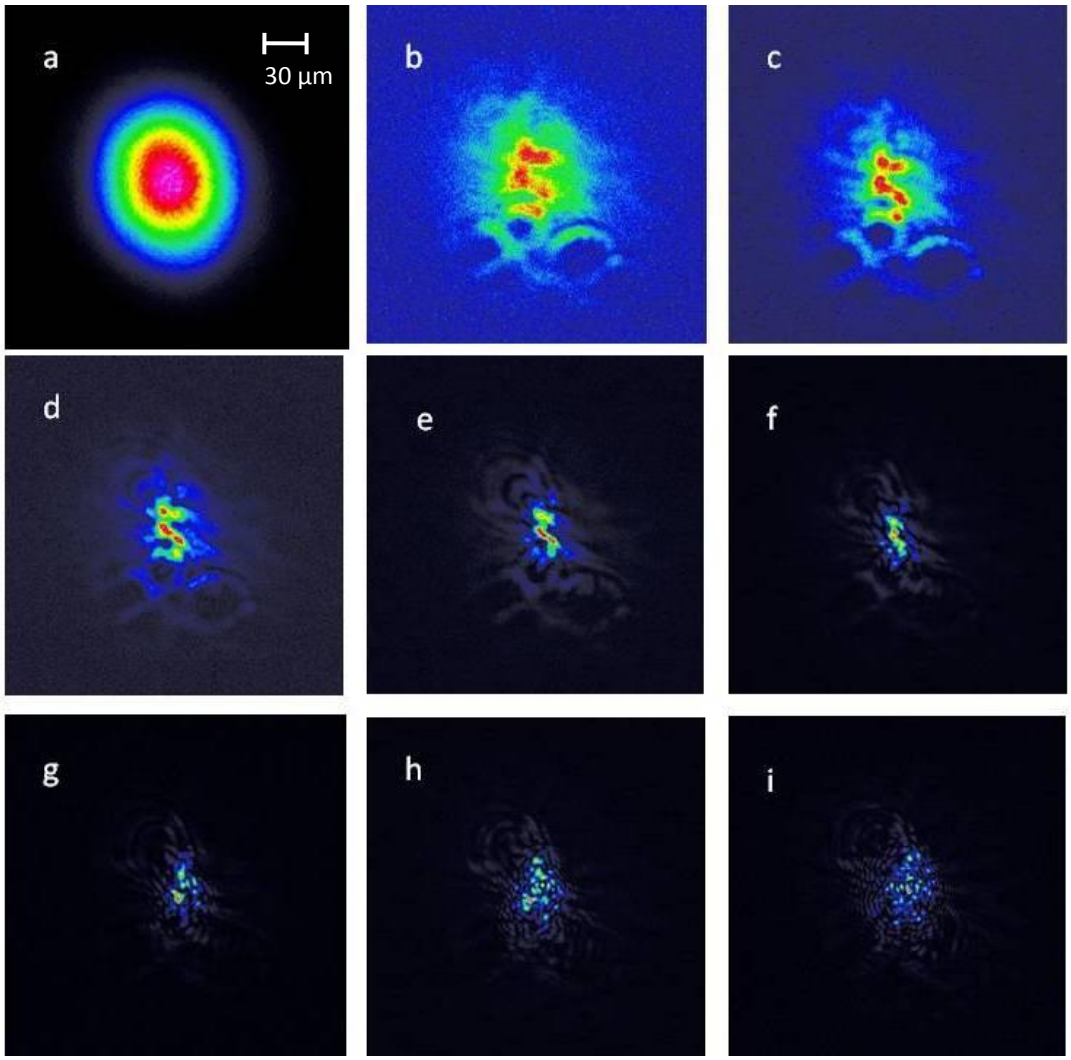

Figure 4.11 Temporal evolution of the 2-D (and 3-D) spatial intensity profiles of the beam at the exit face of the sample cell as the beam self-traps in the organosiloxane with the average intensity of 160 W cm^{-2}, profiles were acquired at (a) 0 s, (b) 36 s, (c) 60 s, (d) 85 s, (e) 112 s, (f) 133 s, (g) 173 s, (h) 204 s, (i) 255s

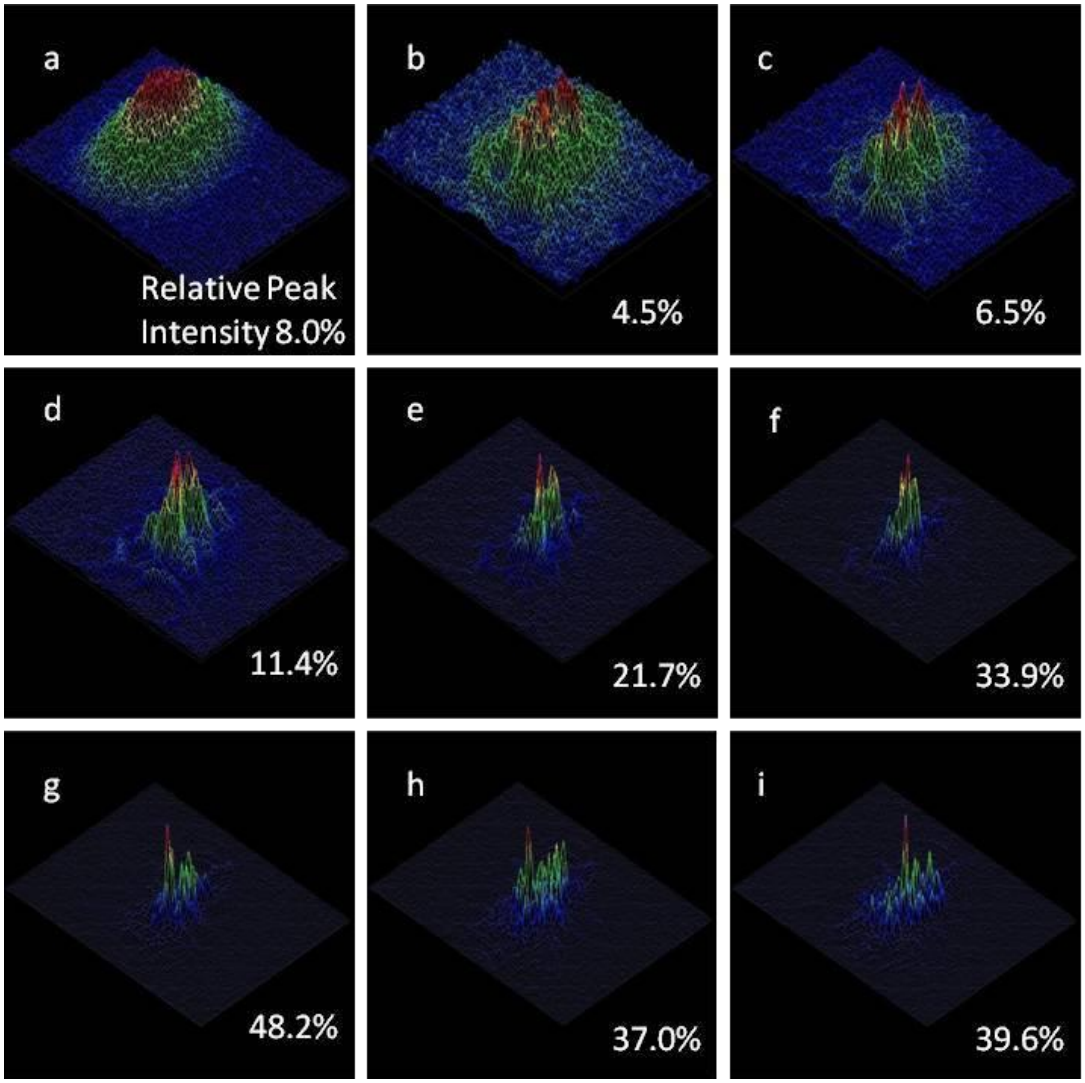

Figure 4.11 (Continues) Temporal evolution of the 2-D (and 3-D) spatial intensity profiles of the beam at the exit face of the sample cell as the beam self-traps in the organosiloxane with the average intensity of 160 W cm^{-2}, profiles were acquired at (a) 0 s, (b) 36 s, (c) 60 s, (d) 85 s, (e) 112 s, (f) 133 s, (g) 173 s, (h) 204 s, (i) 255s

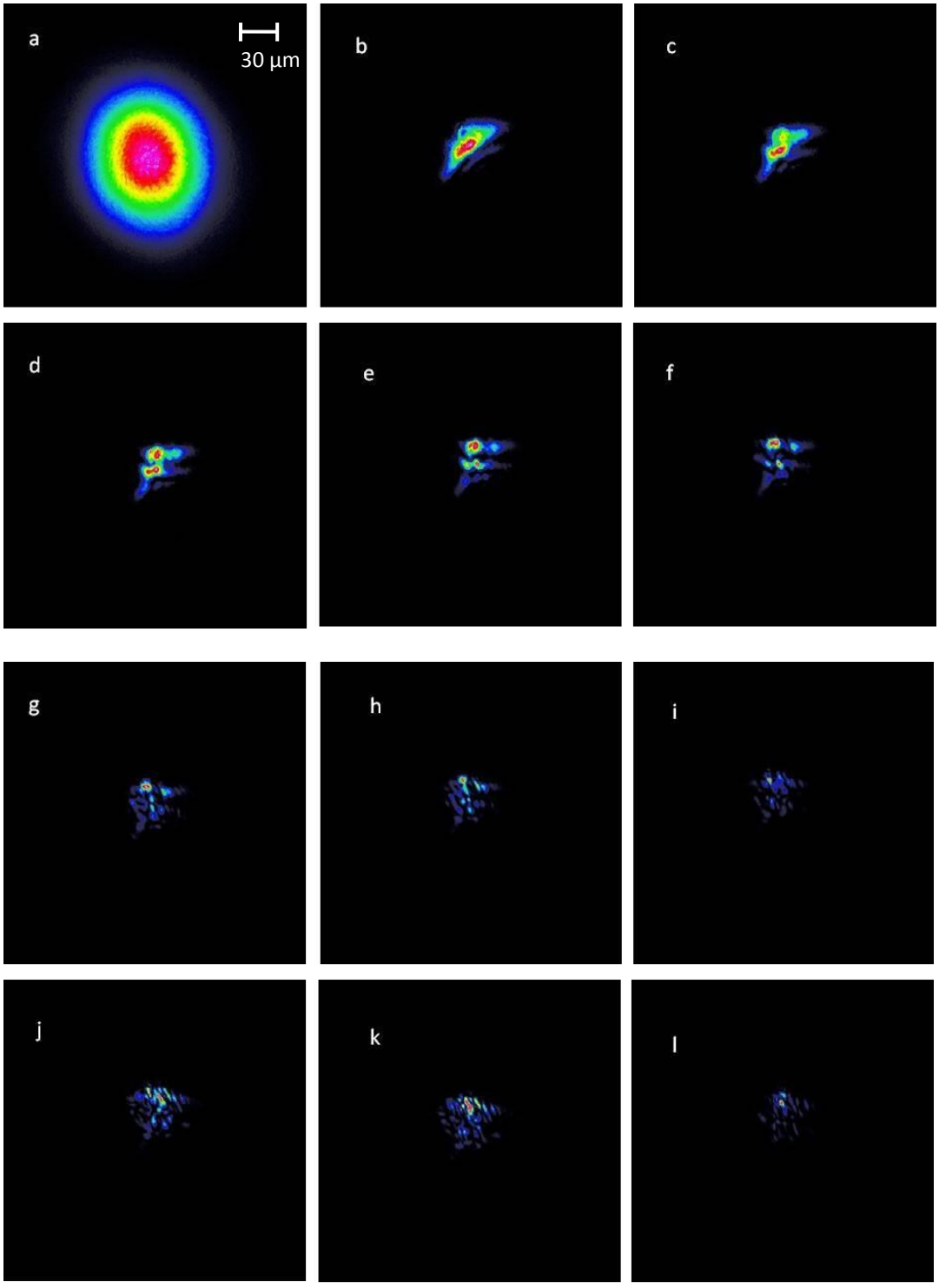
a
30 µm
b
c
d
e
f
g
h
i
j
k
l

Figure 4.12 Temporal evolution of the 2-D (and 3-D) spatial intensity profiles of the beam at the exit face of the sample cell as the beam self-traps in the organosiloxane with the average intensity of 1592 W cm^{-2}, profiles were acquired at (a) 0 s, (b) 4 s, (c) 35 s, (d) 51 s, (e) 73 s, (f) 96 s, (g) 115 s, (h) 131 s, (i) 165 s, (j) 181 s, (k) 197 s, (l) 218 s

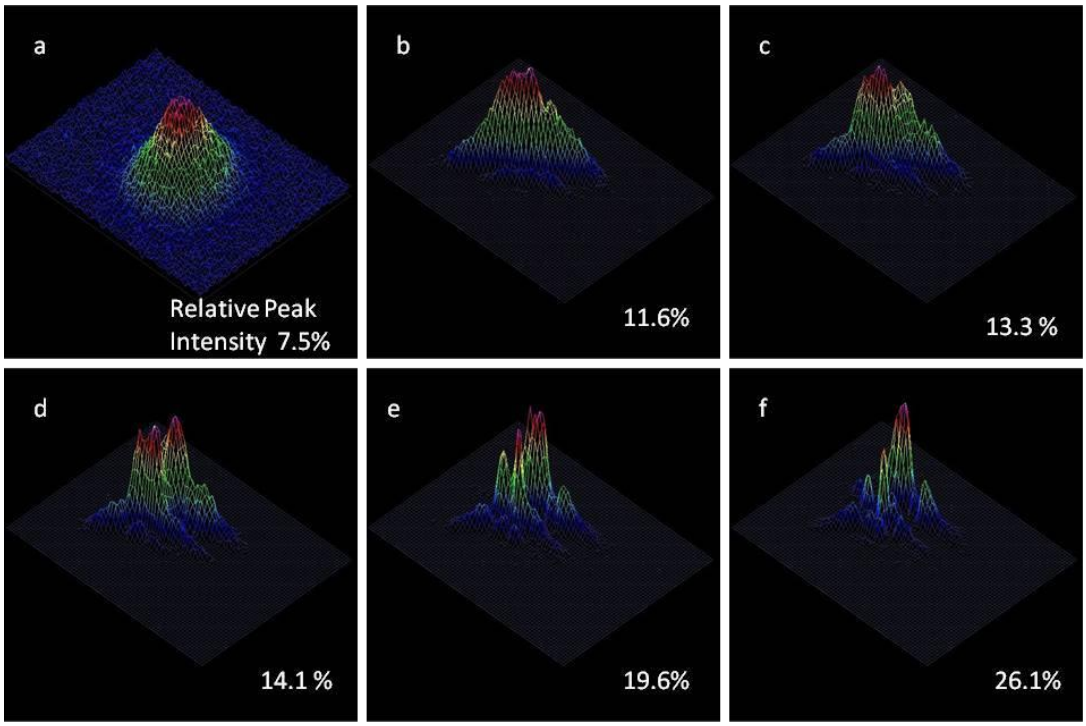

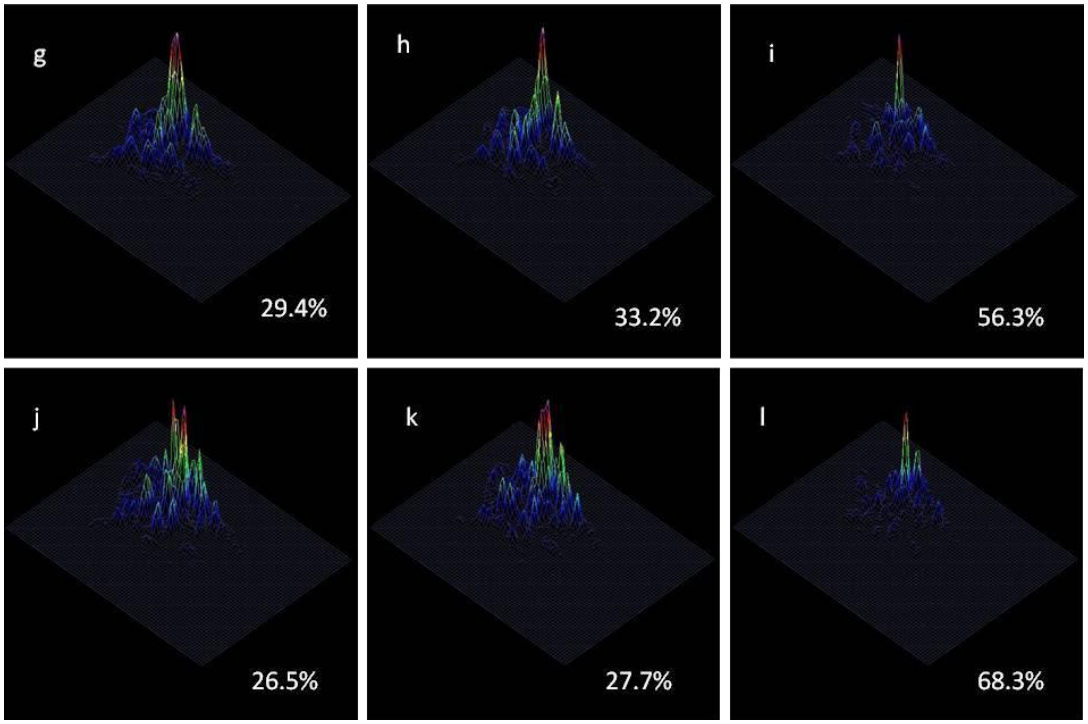

Figure 4.12 (Continues) Temporal evolution of the 2-D (and 3-D) spatial intensity profiles of the beam at the exit face of the sample cell as the beam self-traps in the organosiloxane with the average intensity of 1592 W cm^{-2}, profiles were acquired at (a) 0 s, (b) 4 s, (c) 35 s, (d) 51 s, (e) 73 s, (f) 96 s, (g) 115 s, (h) 131 s, (i) 165 s, (j) 181 s, (k) 197 s, (l) 218 s

4.4 Conclusions

In this chapter, an examination was made of the phenomena of self-trapping continuous-wave Gaussian beam of 532 nm of wavelength as it propagated through the photopolymerizable organosiloxane over 8 orders of magnitude in intensity. As the intensity increased, different beam profiles at the exit face of the sample cell

were able to be observed (Figs 4.2, 4.8, 4.9, 4.10, 4.11, 4.12), and a trend in the self-focusing time against the beam intensity (Fig 4.6), and a trend in the effective beam diameter against the beam intensity (Fig 4.7) were noted. Both trends have its lowest point at the average power of 0.008 W cm^{-2}.

The results confirmed the predictions of the theoretical models developed in the past decades. These included the formation of high-order modes, the appearance of diffraction rings, and the existence of multimode waveguides. The utility of this experiment makes it possible to observe all these phenomena with a CCD camera focused at the exit face of the sample cell. Data for the temporal evolution of the beam has been recorded for further study. The broad range of the output intensity of the IC-FD Nd: YVO_4/ MgO: PPLN green laser made it possible to initiate the experiment with the intensity of 8 orders of magnitude, and the quantitative analysis indicated the significance of the gradient of the self-induced refractive index change, with the conclusion that the most effective self-trapping at the low-intensity regime was where the strongest gradient are formed. Diffraction rings and the beam filamentation could clearly be observed at the mid-intensity and the high-intensity regime respectively.

Chapter 5 INTERACTIONS OF A PAIR OF MUTUALLY COHERENT SELF-TRAPPED BEAMS IN A PHOTOPOLYMERIZABLE MEDIUM

5.1 Introduction

When a typical Gaussian beam propagates through the photopolymerizable material, the refractive index of the medium is modified as the beam shines through. Different gradients can also be formed with incident beams of various intensities. Self-trapping occurs with both coherent laser light (127) and incoherent white light (128). However, different from what was observed with the two-beam interactions of self-trapped white light (129), the phenomena were observed with the coherent two-beam interaction with a light source of IC-FD Nd: YVO_4/ MgO: PPLN green laser split into two coherent beams with a pinhole array were presented.

In this chapter, a focus has been put on the interactions of the two parallel beams with different distances in between them. The pinhole array sets that were used to split the laser beam possessed two pinholes of the diameter of 50 μm and spacing of 200, 500 and 1500 μm between the two holes respectively. Each pinhole set gave two parallel beams a different separation. With a high-resolution CCD camera focused at the exit face of the sample cell, the profile of the beam characteristics could be examined with visual pictures and it was possible to measure the change quantitatively at the exit face. This chapter consists of detailed

analysis of the progression of the beam profiles as the distance between the beams was alterred.

5.2 Generation of a Pair of Parallel-Propagating Self-Trapped Beams

A Gaussian beam of 532 nm was expanded with a $10\times$ beam expander and was split by a pinhole array, after which the average intensity was approximately 2×10^{-2} W cm^{-2} at the entrance face of the custom-made cylindrical sample cell containing the photopolymerizable organosiloxane. The refractive index of the organosiloxane is 1.47. The beams were focused at the entrance face of the sample cell with a focal width of around 500 μm depending on the separation of the pinholes. The 2-D intensity profile of the beams going through a 500, 200, 1500 μm pinhole array at the exit face was monitored by the high resolution CCD camera, and a typical profile of the beams without going through the sample is shown in Figs 5.1, 5.2, 5.3.

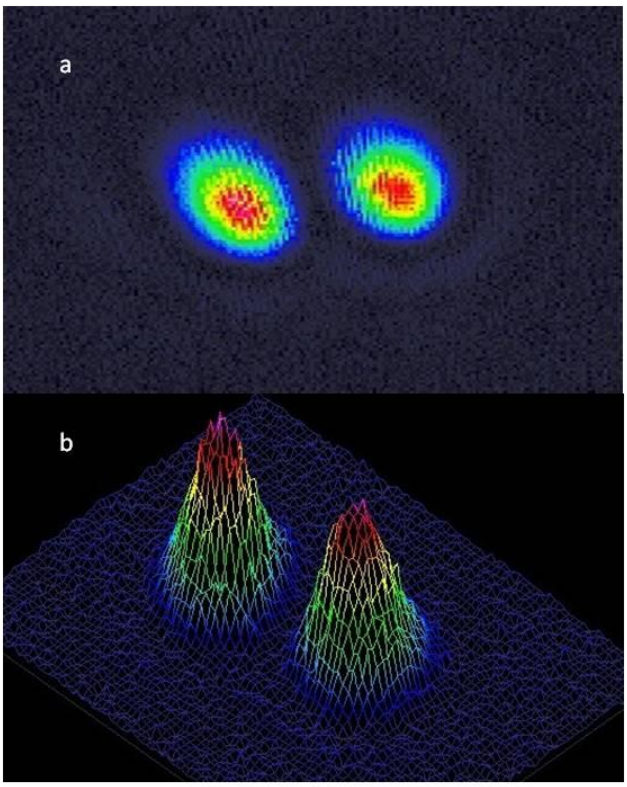

Figure 5.1 2-D (and 3-D) profile at the exit face of the sample cell without going through the organosiloxane, with a pinhole array of 500 μm distance between the two pinholes employed to split the beam, the focused beam diameter is 70 μm and the distance between the two beams is 589 μm, the average intensity is approximately $2\times\mathbf{10^{-2}}$ W cm^{-2}.

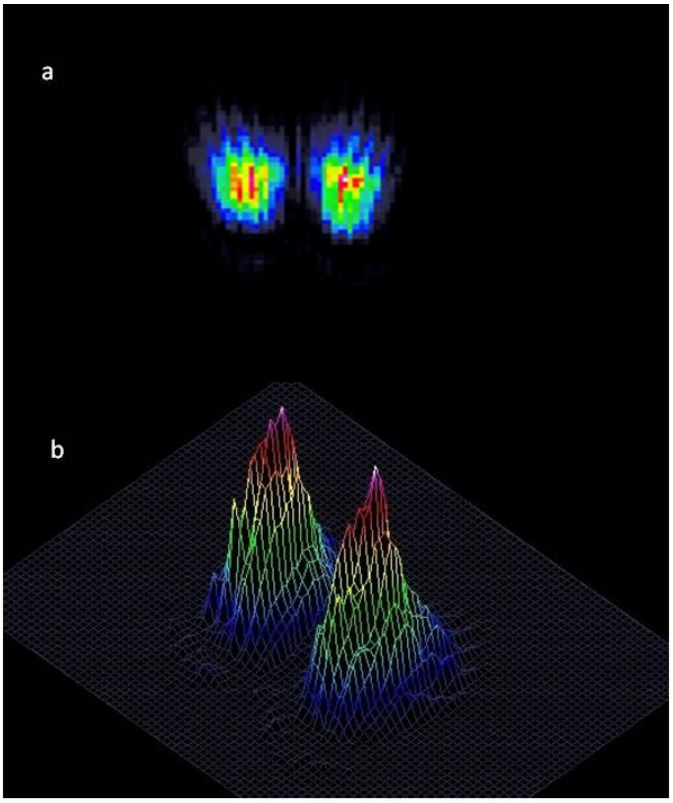

Figure 5.2 2-D (and 3-D) profile at the exit face of the sample cell without going through the organosiloxane, with a pinhole array of 200 μm distance between the two pinholes employed to split the beam, the focused beam diameter is 31 μm and the distance between the two beams is 222 μm, the average intensity is approximately $2\times\mathbf{10^{-2}}$ W cm^{-2}.

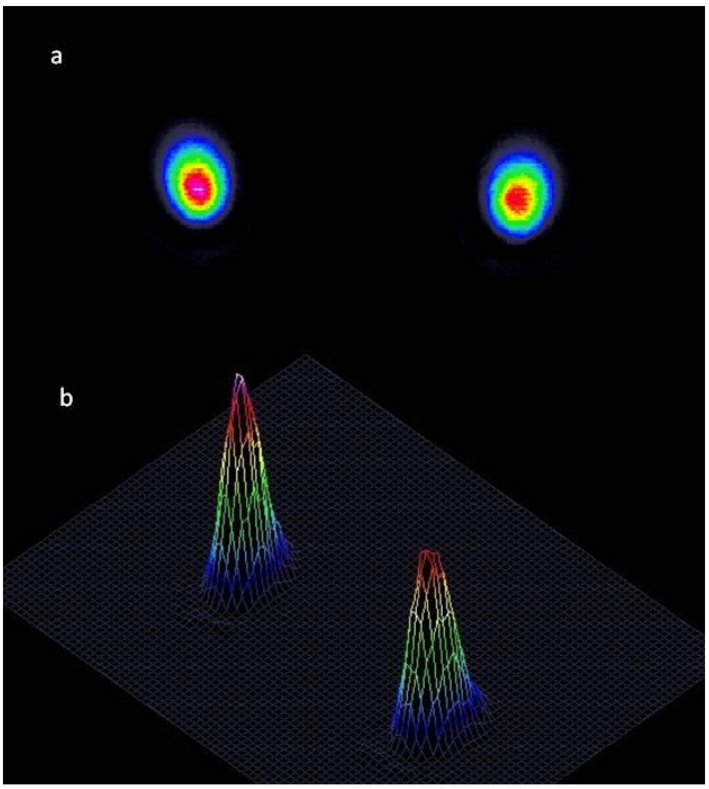

Figure 5.3 2-D (and 3-D) profile at the exit face of the sample cell without going through the organosiloxane, with a pinhole array of 1500 μm distance between the two pinholes employed to split the beam, the focused beam diameter is 60 μm and the distance between the two beams is 1722 μm, the average intensity is approximately $2 \times \mathbf{10^{-2}}$ W cm^{-2}.

5.3 Two-Beam interactions with variable distances

The temporal evolution of the 2-D intensity of the beam profile at the exit face is shown in Fig 5.4

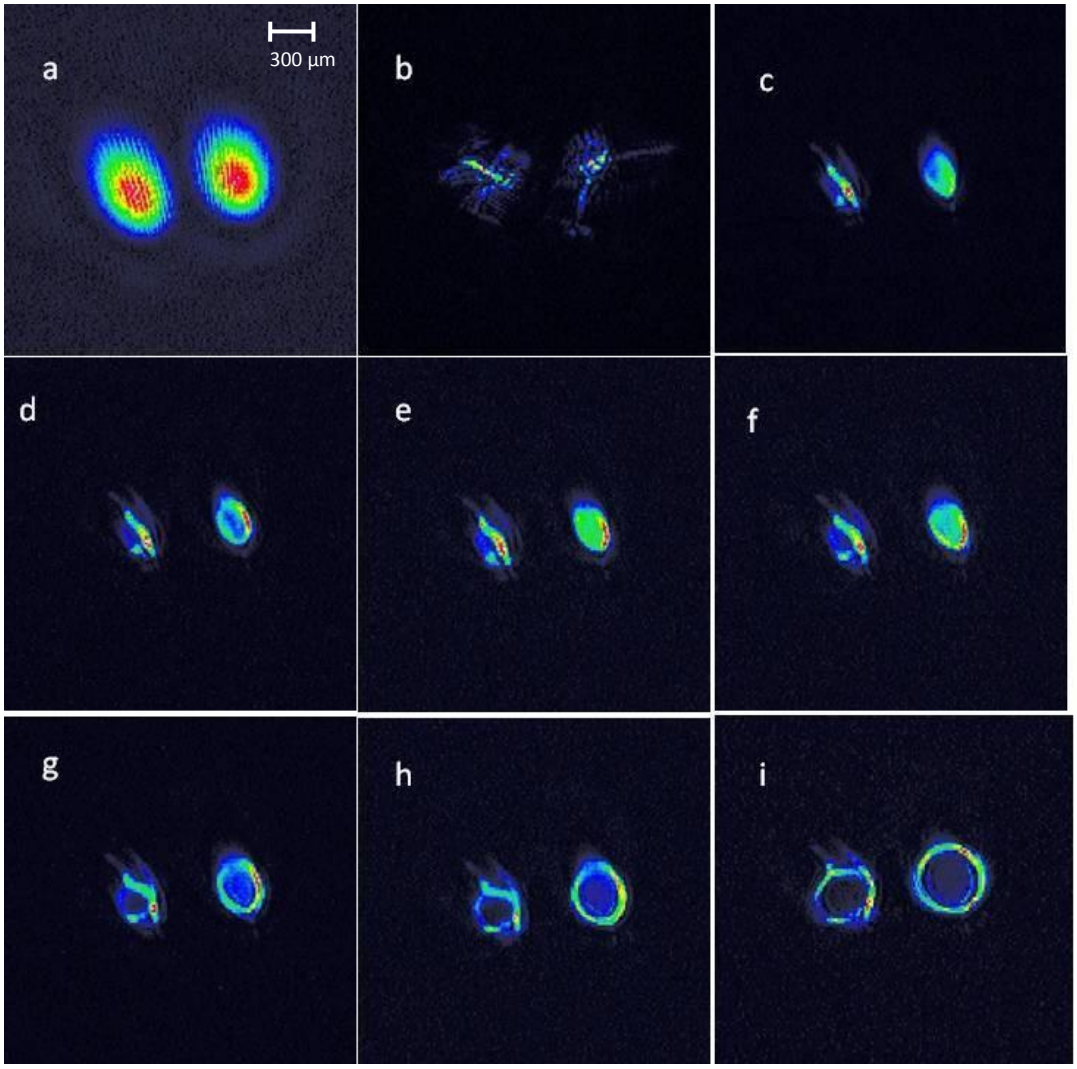

Figure 5.4 Temporal evolution of the 2-D (and 3-D) spatial intensity profiles of the beams (500 μm pinhole) at the exit face of the sample cell as the beams self-traps in the organosiloxane with the average intensity of $2\times\mathbf{10^{-2}}$ W cm^{-2}, profiles were acquired at (a) 0 s, (b) 22 s, (c) 267 s, (d) 367 s, (e) 409 s, (f) 499 s, (g) 745 s, (h) 788 s, (i) 1054 s.

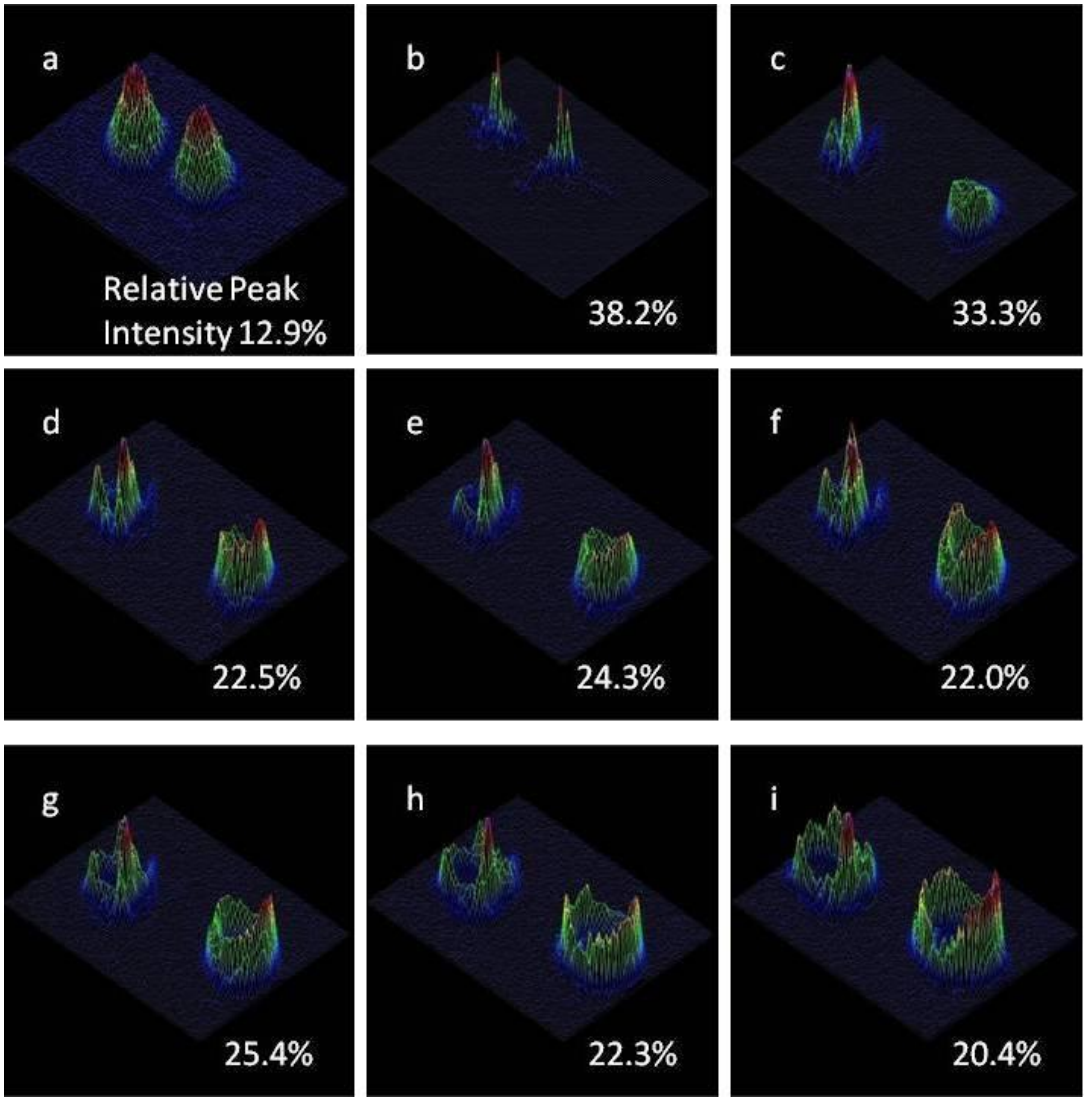

Figure 5.4 (Continues) Temporal evolution of the 2-D (and 3-D) spatial intensity profiles of the beams (500 μm pinhole) at the exit face of the sample cell as the beams self-traps in the organosiloxane with the average intensity of $2\times\mathbf{10^{-2}}$ W cm^{-2}, profiles were acquired at (a) 0 s, (b) 22 s, (c) 267 s, (d) 367 s, (e) 409 s, (f) 499 s, (g) 745 s, (h) 788 s, (i) 1054 s.

The beam started to self-trap immediately after the organosiloxane was exposed to the green laser. The superspostions of the high-order modes appeared at 22 seconds into the experiment (Fig 5.4(b)), and single ring filamentation started to form separately. The ring on the right side formed at 745 seconds (Fig 5.4(g)), and the ring on the left side formed at 788 seconds (Fig 5.4(h)), and the two rings were fully formed at 1054 seconds (Fig 5.4(i)).

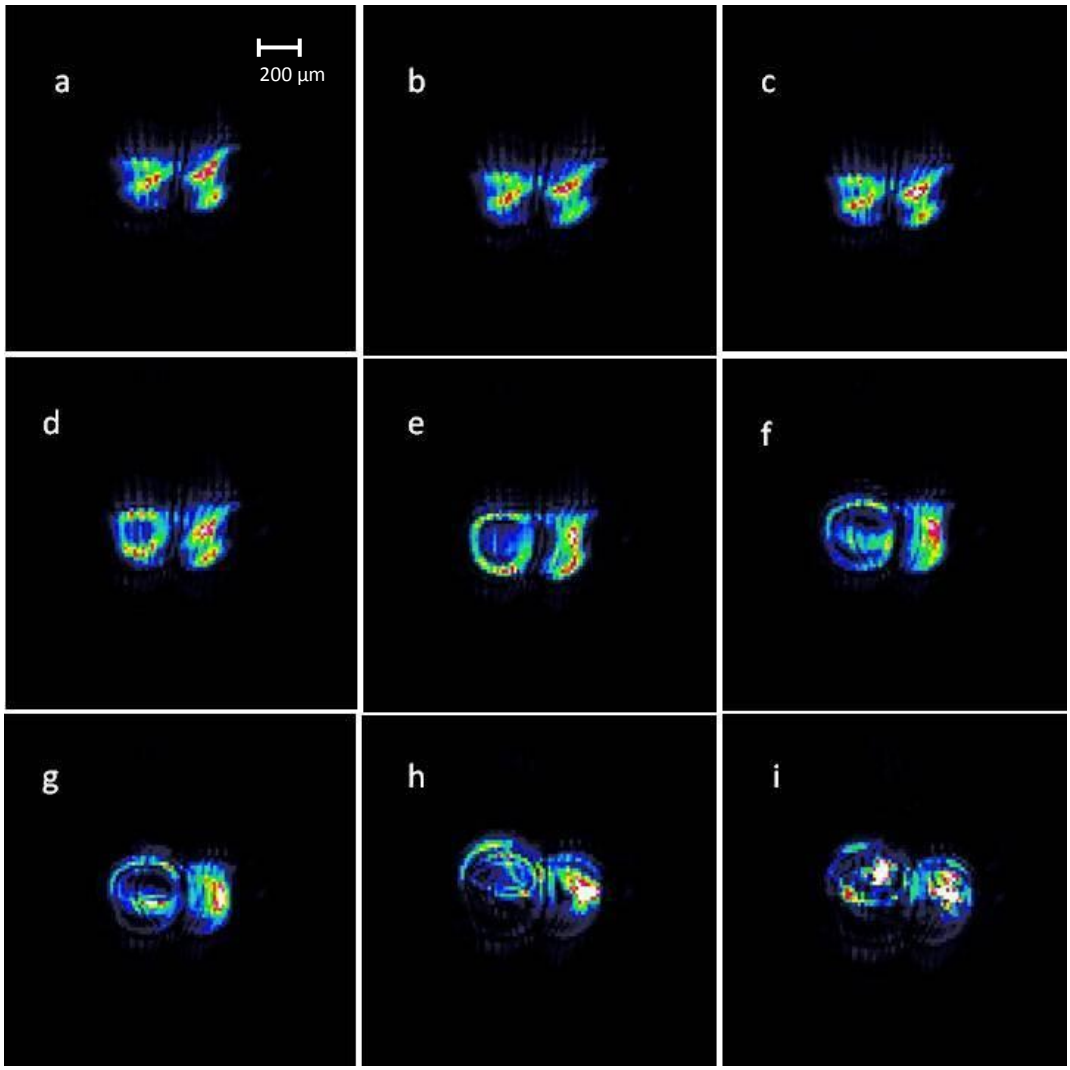

Figure 5.5 Temporal evolution of the 2-D (and 3-D) spatial intensity profiles of the beams (200 μm pinhole) at the exit face of the sample cell as the beams self-traps in the organosiloxane with the average intensity of $2\times\mathbf{10^{-2}}$ W cm^{-2}, profiles were acquired at (a) 10 s, (b) 32 s, (c) 116 s, (d) 252 s, (e) 514 s, (f) 662 s, (g) 788 s, (h) 1054 s, (i) 1862 s.

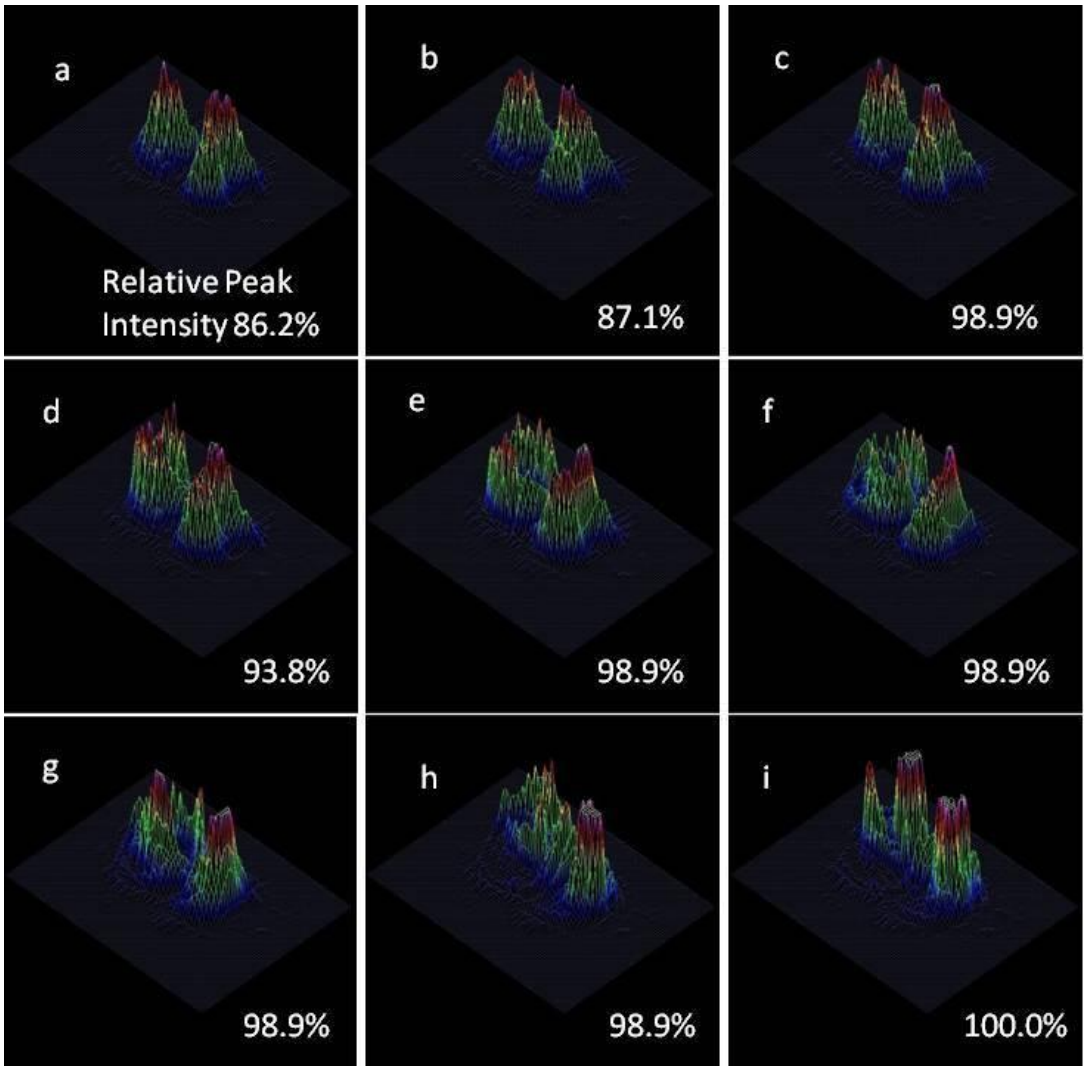

Figure 5.5 (Continues) Temporal evolution of the 2-D (and 3-D) spatial intensity profiles of the beams (200 μm pinhole) at the exit face of the sample cell as the beams self-traps in the organosiloxane with the average intensity of $2\times\mathbf{10^{-2}}$ W cm^{-2}, profiles were acquired at (a) 10 s, (b) 32 s, (c) 116 s, (d) 252 s, (e) 514 s, (f) 662 s, (g) 788 s, (h) 1054 s, (i) 1862 s.

As the experiment was switched to pinhole array with 200 μm distance between the two beams, the focused beam diameter was 31 μm at the entrance face of the sample cell, and the distance between the beams was 222 μm. The intensity profile of the beams is shown in Fig 5.5. The high-order modes came into formation at 10 seconds (Fig 5.5 (a)) into the experiment, and seemingly LP11 modes were formed with both beams as the time elapsed, as shown in Figs 5.5 (b) and 5.5 (c). At approximately 252 seconds, the single diffraction ring started to form with one of the beams (Fig 5.5 (d)), and the self-trapping resulted as multiple filaments after 1000 seconds (Figs 5.5 (h) and 5.5 (i)).

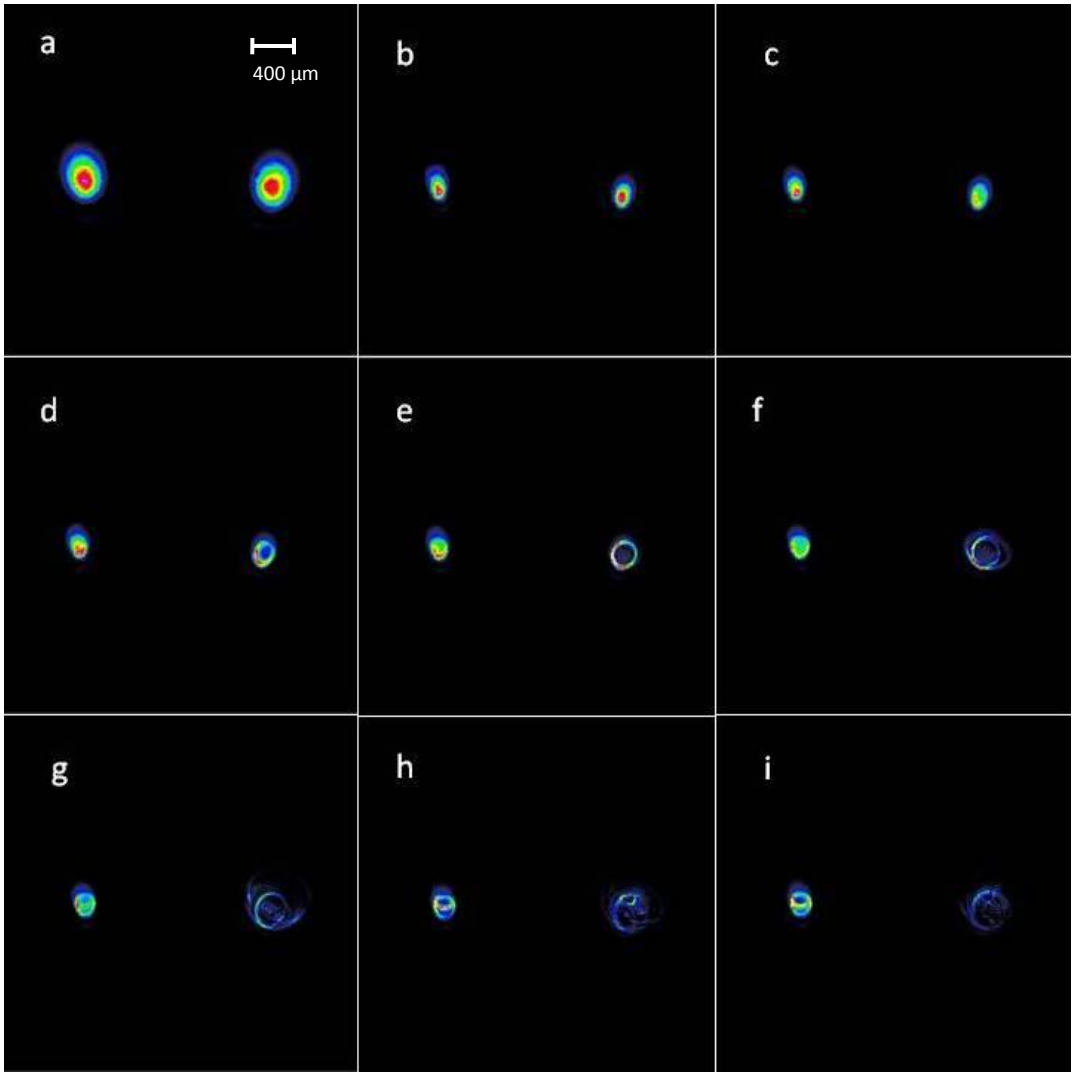

Figure 5.6 Temporal evolution of the 2-D (and 3-D) spatial intensity profiles of the beams (1500 μm pinhole) at the exit face of the sample cell as the beams self-traps in the organosiloxane with the average intensity of $2\times\mathbf{10^{-2}}$ W cm^{-2}, profiles were acquired at (a) 0 s, (b) 34 s, (c) 256 s, (d) 391 s, (e) 500 s, (f) 588 s, (g) 736 s, (h) 1054 s, (i) 1564 s.

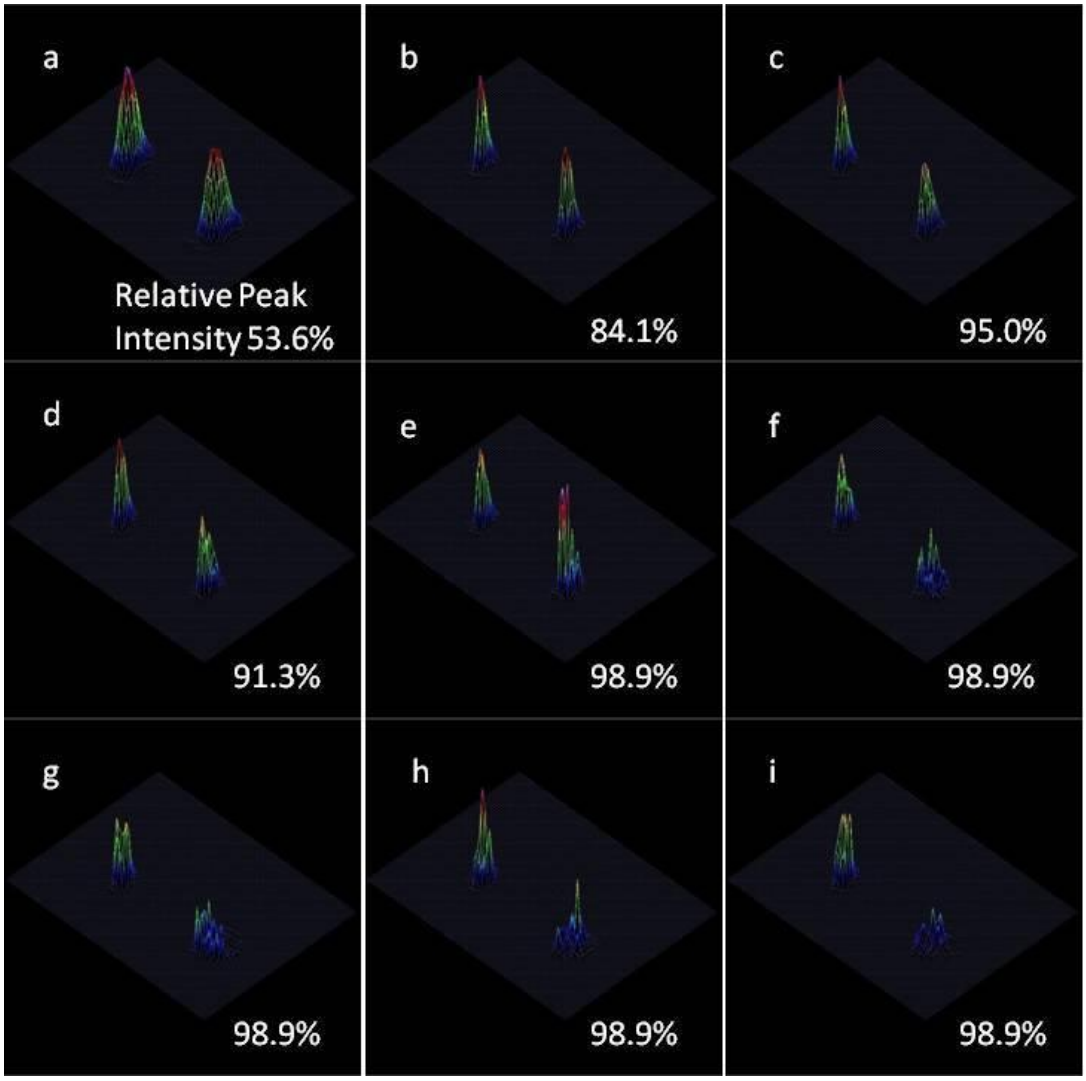

Figure 5.6 (Continues) Temporal evolution of the 2-D (and 3-D) spatial intensity profiles of the beams (1500 μm pinhole) at the exit face of the sample cell as the beams self-traps in the organosiloxane with the average intensity of $2\times\mathbf{10^{-2}}$ W cm^{-2}, profiles were acquired at (a) 0 s, (b) 34 s, (c) 256 s, (d) 391 s, (e) 500 s, (f) 588 s, (g) 736 s, (h) 1054 s, (i) 1564 s.

As the experiment was switched to a pinhole array with 1500 μm distance between the two beams, the focused beam diameter was 60 μm at the entrance face of the sample cell, and the distance between the beams was 1722 μm. The intensity profile of the beams is shown in Fig 5.6. The beams started to decrease in their size at 34 seconds (Fig 5.6 (a)) into the experiment, and the high-order modes came into formation in both of the beams, as shown in Figs 5.6 (b) and 5.6 (c). At approximately 391 seconds, the single diffraction ring started to form with one of the beams (Fig 5.6 (d)), and the other beam became like a ring shape diffraction pattern at around 736 seconds, as shown in Fig 5.6 (g). At the end of the experiment, the self-trapping resulted as multiple filaments after 1000 seconds (Figs 5.6 (h) and 5.6 (i)).

The single diffraction ring formed as a result of the flattened refractive index profile. As indicated in Fig 5.7, the Gaussian index profile flattened over time. The beam encountering the flattened Gaussian index profile was focused into a ring under nonlinear conditions (130).

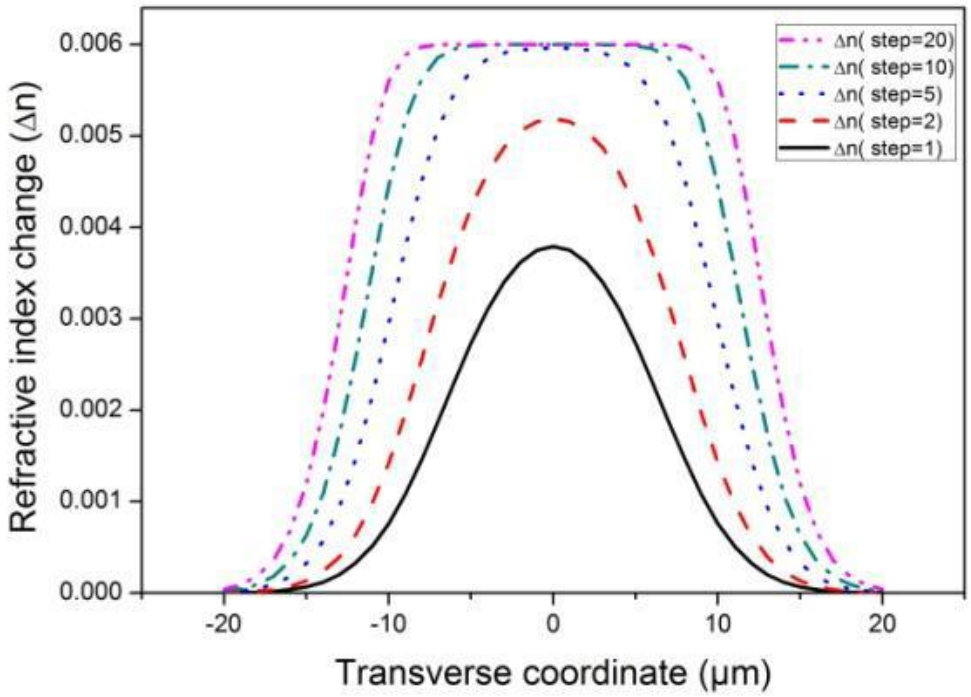

Figure 5.7 Calculated temporal variation of refractive index profiles induced by a Gaussian beam in a photopolymer, time is represented by steps (130). Reproduced with permission.

5.4 Conclusions

The parallel-propagating and mutually coherent 532 nm green laser beams self-trapped as they traveled though the photopolymerizable organosiloxane. Single diffraction ring formed as a result of the flattened refractive index profile. There

was a competition between the beams and one of them exhibited the phenomenon of single-ring diffraction as discussed in Chapter 4.3. The intensity of one of the beams became dominantly higher than the other when the diffraction ring was forming, while the other suffered from the decrease of the intensity after the self-trapping began. As the two-beam self-trapping was taking place, there was no significant change in the distance between the two beams.

Chapter 6 CONCLUSIONS AND FUTURE WORK

6.1 Conclusion

The main motivation of this thesis was to experimentally investigate the self-action phenomena in a photopolymer material with a miniature green laser. The design and fabrication of the intra-cavity frequency doubling (IC-FD) Nd: YVO_4/MgO: PPLN laser was accomplished as the coherent light source. The dynamics of self-trapping and nonlinear propagation phenomena were examined with the incident beam intensity ranging over eight orders of magnitude. The studies involved detailed analysis of the self-action effects in the photopolymer induced by the miniature green laser; preliminary experiments on two-beam interaction experiments were also performed. The results of this thesis contributed to the understanding of the spatial nonlinear phenomena in photopolymer, and due to the introduction of miniature green laser, the set-up of the experiments was much simpler than previous attempts, particularly as only very few optical components were required. Possible future applications were proposed.

Different methods to achieve green light of 532 nm were reviewed, and from theoretical consideration it was possible to design the green laser by adopting a proper method and material. The actual laser was made using the IC-FD method

employing optical contact Nd:YVO_4 and periodically poled 5% doped MgO: $LiNbO_3$ crystal. The laser could achieve over 40 mW green light output power with the electrical-to-optical efficiency of approximately 10%. The crystals microchip was made up of a 0.5 mm long Nd doped Nd: YVO_4 and 1 mm long MgO: PPLN with 7 μm period, with coatings on both sides. The thermal control ensured the stable light output of the laser. The output was a single mode green light of 532 nm and the fluctuation was less than 2 %.

By employing this miniature green laser as the light source, the design of the optical set-up allowed the in-situ monitoring of the beam profile as it self-trapped in photopolymers. Temporal evolution of the laser beams in the photopolymer was studied over a span of intensities across 8 orders of magnitude (from 3.2×10^{-5} W cm^{-2} to 6368 W cm^{-2}). Different forms of nonlinear propagation were identified: the self-trapping at low-intensity regime, the formation of the diffraction rings at the mid-intensity regime and the beam filamentation at the high-intensity regime.

The design of the experiment allowed the quantitative monitoring of the parameters of the self-trapping process. By examining the self-trapping parameters such as the self-trapping time and the effective beam diameters, it was observed that an optimum self trapping intensity (0.008W $cm^{-2)}$, at which the beam has the shortest self-trapping time and the smallest effective beam diameter.

The two beam experiment was performed with a pinhole array that split the light into two parallel beams. Three sets of arrays were employed with 50 μm diameter pinholes and spacings of 200, 500 and 1500 μm between the two holes.

The experiment was carried out with the same average beam intensity of approximately 2×10^{-2} W cm^{-2}. In addition to the phenomena observed in the one beam experiment, such as the formation of the diffraction ring, the filamentation of the beam, a competition was observed between the beams. One of them had dominantly higher intensity while forming the diffraction ring, as the other suffered from the decrease of the intensity after the self-trapping began.

6.2 Future Work

The work presented in this thesis provides a strong foundation for future work. A detailed intensity dependence study could be carried out in the two-beam interaction experiments. By comparing the different nonlinear actions in the two-beam experiment, a better understanding of the interaction of self-trapping beams in organosiloxane could be achieved. Besides parallel beams, perpendicular beams or beams of different angles could also be investigated.

Because of the simple design of the experiment set-up and the existence of the optimum self-trapping parameters, permanent structures induced through the self-action effects in the photopolymers can be adopted for different optical applications. In order to solidify the feasibility of the application, new types of photopolymer with better stability after photopolymerization need to be examined.

References

1. T. H. Maiman, “Stimulated optical radiation in Ruby,” Nature, vol.187, no.4736, pp. 493-494, 1960.
2. R. N. Hall, G. E. Fenner, J. D. Kingsley, T. J. Soltys, and R. O. Carlson, “Coherent Light Emission From GaAs Junctions,” Phys. Rev. Lett., vol. 9, pp. 366–368, 1962.
3. M. I. Nathan, W. P. Dumke, G. Burns, F. H. Dill, and G. Lasher, “Stimulated Emission of Radiation from GaAs p-n Junctions,” Appl. Phys. Lett., vo1.1, pp. 62-64, 1962.
4. S. Nakamura, N. Iwasa, M. Senoh and T. Mukai, “Hole Compensation Mechanism of P-Type GaN Films,” Jpn. J. Appl. Phys, vol. 31, pp. 1258-1266, 1992.
5. S. Nakamura, M. Senoh, S. Nagahama, N. Iwasa, T. Yamada, T. Matsushita, H. Kiyoku and Y. Sugimoto, “InGaN-Based Multi-Quantum-Well-Structure Laser Diodes,” Jpn. J. Appl. Phys., vol. 35, L74-L76, 1996.
6. Y.-D. Lin, M. T. Hardy, P. S. Hsu, K. M. Kelchner, C.-Y. Huang, D. A. Haeger, R. M. Farrell, K. Fujito, A. Chakraborty, H. Ohta, J. S. Speck, S. P. DenBaars and S. Nakamura, “Blue-Green InGaN/GaN Laser Diodes on Miscut m-Plane GaN Substrate,” Appl. Phys. Exp., vol. 2, pp. 082102, 2009.

7. Y. Enya, Y. Yoshizumi, T. Kyono, K. Akita, M. Ueno, M. Adachi, T. Sumitomo, S. Tokuyama, T. Ikegami, K. Katayama, and T. Nakamura, "531nm green lasing of InGaN based laser diodes on semi-polar {2021} free-standing GaN substrates," Appl. Phys. Exp., vol. 2, no. 8, pp. 082101, Aug. 2009.
8. A. Avramescu, T. Lermer, J. Müller, S. Tautz, D. Queren, S. Lutgen, and U. Strauß, "InGaN laser diodes with 50 mW output power emitting at 515 nm," Appl. Phys. Lett., vol. 95, no. 7, pp. 071103, Aug. 2009.
9. S. Takagi et al, "High-Power (over 100 mW) Green Laser Diodes on Semipolar{20$\bar{2}$1} GaN Substrates Operating at Wavelengths beyond 530 nm," Appl. Phys. Exp., vol. 5, pp082102, 2012.
10. P.A. Franken A. E. Hill, C. W. Peters, and G. Weinreich, "Generation of optical harmonics," Phys. Rev. Lett., vol.7, p. 118 Aug. 1961.
11. J. E. Geusie, H. J. Levenstein, S. Sigh, R.G. Smith, and L. G. Van Uitert, "Continuous 0.532-μ solid-state source using $Ba_2NaNb_5O_{15}$," Appl. Phys. Lett., vol.12 no.9, pp.306-309, 1968.
12. R. G. Smith, "Theory of intracavity optical second harmonic generation," IEEE J. Quantum Electron., vol.6, no.4, pp. 215-130, Apr. 1970.
13. Y. Q. Zheng, H. Y. Zhu, L. X. Huang, H. B. Chen, Y. M. Duan, R. B. Su, C. H. Huang, Y. Wei, J. Zhuang, and G. Zhang, "Efficient 532 nm laser using high gray-tracking resistance KTP crystal," Laser Physics, vol. 20, no. 4, pp. 756-760, 2010.

14. N. Pavel, T. Taira, Y. Tamaoki, and H. Kan, " Continuous-wave high-power intracavity frequency-doubled Nd:$GdVO_4$-LBO green laser, ” in Nonlinear Optics: Materials, Fundamentals and Applications, Technical Digest (CD) (Optical Society of America, 2004), paper WD6.
15. Y. Hirano, T. Sasagawa, T. Yanagisawa, S.Yamamoto, A. Nakamura, T. Yagi, and H. Sugiura, “Solid-state SHG green laser for laser TV,” CLEO/QELS, 1-2, 2009.
16. M. Zhou, B. X. Yan, G. Bao, Y. Zhang, C. Gawith, D. D. Wang, Y. Qi, and Y. Bi, “52% optical-to-optical conversion efficiency in a compact 1.5 W 532 nm second harmonic generation laser with intracavity periodically-poled MgO:LiNbO3,” Laser Physics, vol. 20, no. 7, pp. 1568-1571, 2010.
17. Y. Qi, B. Yan, S. Chu, Y. Wang, T. Fang, Y. Bi, W. Yan, H. Min, and Y. Liu, “High Power green laser with PPMgLN intracavity doubled,” in CLEO Pacific Rim, 2009.
18. T. Yokoyama, K. Mizuuchi, K. Nakayama, A. Kurozuka, T. Sugita, A. Morikawa, and K. Yamamoto, “Compact intracavity green light source with wide operation temperature range using periodically poled Mg:LiNbO3,” Jan. J. Appl. Phys., vol. 47, no. 8, pp. 6787-6789, Aug. 2008.
19. Y. Hirano, T. Sasagawa, T. Yanagisawa, S.Yamamoto, A. Nakamura, T. Yagi, and H. Sugiura, “Solid-state SHG green laser for laser TV,” CLEO/QELS, 1-2, 2009.

20. Y. Qi, B. Yan, S. Chu, Y. Wang, T. Fang, Y. Bi, W. Yan, H. Min, and Y. Liu, "High Power green laser with PPMgLN intracavity doubled," in CLEO Pacific Rim, 2009.
21. M. Zhou, B. X. Yan, G. Bao, Y. Zhang, C. Gawith, D. D. Wang, Y. Qi, and Y. Bi, "52% optical-to-optical conversion efficiency in a compact 1.5 W 532 nm second harmonic generation laser with intracavity periodically-poled MgO:LiNbO3," Laser Physics, vol. 20, no. 7, pp. 1568-1571, 2010.
22. A.Jechow, R. Menzel, K. Paschke, and G. Erbert, "Blue-green light generation using high brilliance edge emitting diode lasers," Laser Photon. Rev., vol. 4, no. 5, pp. 633–655, 2010.
23. V. G. Dmitriev, G. G. Gurzadyan, and D. N. Nikogosyan, "Handbook of Nonlinear Optical Crystals," 3rd Rev. Ed., Springer Series in Optical Sciences, Vol. 64, 1999.
24. O. B. Jensen, P. E. Andersen, B. Sumpf, K.-H. Hasler, G. Erbert, and P. M. Petersen, "1.5 W green light generation by single-pass second harmonic generation of a single-frequency tapered diode laser," Opt. Expr., vol. 17, no.8, pp. 6532–6539, Apr. 2009.
25. C. Fiebig, G. Blume, M. Uebernickel, D. Feise, C. Kaspari, K. Paschke, J. Fricke, H. Wenzel, and G. Erbert, "High-power DBR-tapered laser at 980 nm for single-path second harmonic generation," IEEE J. Sel. Top. Quantum Electron., vol. 15, no. 3, pp. 978–983, May-June 2009.

26. H. K. Nguyen, M. H. Hu, Y. Li, K. Song, N. J. Visovsky, S. Coleman, and C.-E. Zah, “304 mW green light emission by frequency doubling of a high-power 1060-nm DBR semiconductor laser diode,” in Proc. of SPIE, vol. 6890, pp. 6890I, 2008.

27. M. Kuznetsov, F. Hakimi, R. Sprague, A. Mooradian, "High-power (>0.5-W CW) diode-pumped vertical-external-cavity surface-emitting semiconductor lasers with circular TEM00 beams," IEEE Photon. Technol. Lett., vol.9, no.8, pp.1063-1065, Aug. 1997.

28. M. Kuznetsov, F. Hakimi, R. Sprague, A. Mooradian, “Design and characteristics of high-power (>0.5-W CW) diode-pumped vertical-external-cavity surface-emitting semiconductor lasers with circular TEM_{00} beams," *IEEE Selected Top. in Quantum Electron.*, vol.5, no.3, pp.561-573, May/Jun 1999.

29. L.E. Hunziker, C. Ihli, D.S. Steingrube, “Miniaturization and Power Scaling of Fundamental Mode Optically Pumped Semiconductor Lasers,” IEEE Selected Topics in Quantum Electron., vol.13, no.3, pp.610-618, May-june 2007.

30. J. Lee , S. Lee , T. Kim and Y. Park, "7 W high-efficiency continuous-wave green light generation by intracavity frequency doubling of an end-pumped vertical external-cavity surface emitting semiconductor laser", Appl. Phys. Lett., vol. 89, pp. 241107 2006.

31. M. Fallahi, F. Li Y. Kaneda, C. Hessenius, J. Hader, Li H. J.V. Moloney, B. Kunert, W. Stolz, S.W. Koch, J. Murray, and R. Bedford, "5-W Yellow Laser by Intracavity Frequency Doubling of High-Power Vertical-External-Cavity Surface-Emitting Laser," IEEE Photon. Technol. Lett., vol.20, no.20, pp.1700-1702, Oct.15, 2008.

32. E. U. Rafailov, W. Sibbett, A. Mooradian, J. G. McInerney, H. Karlsson, S. Wang, and F. Laurell, "Efficient frequency doubling of a vertical-extended-cavity surface-emitting laser diode by use of a periodically poled KTP crystal," Opt. Lett., vol.28, no.21, pp.2091-2093 2003.

33. F. Laurell, "Stable blue second-harmonic generation in a KTP waveguide with a diode laser in an external cavity," *Electron. Lett.*, vol.29, no.18, pp.1629-1630, 2 Sept. 1993.

34. J. Zimmermann, Jens Struckmeier, Martin R. Hofmann, and Jan-Peter Meyn, "Tunable blue laser based on intracavity frequency doubling with a fan-structured periodically poled $LiTaO_3$ crystal," *Opt. Lett.*, vol. 27, no.8, pp. 604-606, 2002.

35. K. Li, A. Yao, N. J. Copner, C. B. E. Gawith, I. G. Knight, H.-U. Pfeiffer, and B. Musk, "Compact 1.3 W green laser by intracavity frequency doubling of a multi-edge-emitter laser bar using a MgO: PPLN crystal," *Opt. Lett.*, vol. 34, no. 22, pp. 3472–3474, Nov. 2009.

36. B. T. Matthias, J. P. Remeika, "Ferroelectricity in the Ilmenite Structure," Phys. Rev. 76, 1886–1887, 1949.

37. K. Nassau, H.J. Levinstein, G.M. Loiacono, “Ferroelectric lithium niobate. 1. Growth, domain structure, dislocations and etching,” J. Chem. Phys. Solids 27, 983-988, 1966.

38. R. S. Wies and T. K. Gaylord, “Lithium niobate: Summary of physical properties and crystal structure,” Appl. Phys. A 37, 191-203, 1985.

39. http://www.photonik.uni-bonn.de/Papers/talks/080624_Buse.pdf

40. N. Iyi, K. Kitamura, F. Izymi, K. Kimura, J.K.Yamamoto, J. Solid State Chem. vol.101, p.340, 1992.

41. D. A. Bryan, R. Gerson, and H. E. Tomaschke, “Increased optical damage resistance in lithium niobate,” Appl. Phys. Lett., vol. 44, no. 9, pp. 847–849, 1984.

42. A. L. Schwlow and C.H. Townes. Infrared and optical masers. Physical Review, 112(6), 1958.

43. J. S. Aitchison, A. M Weiner, Y. Silberberg, M. K Oliver, J. L Jackel, D. E Leaird, E. M Vogel, and P. W.E Smith. “Observation of spatial optical solitons in a nonlinear glass waveguide,” Optics Letters, 15(9):471-473, 1990.

44. S. D. Durbin, S. M. Arakelian, and Y. R Shen. “Laser-induced diffraction rings from a nematic-liquid-crystal film,” Optics letters, 6(9):411-413, 1981.

45. J. S. Aitchison, K. Al-Hemyari, C. N Ironside, R. S Grant, and W. Sibbett, “Observation of spatial solitons in AlGaAs waveguides,” Electronics Letters , vol.28, no.20, pp.1879-1880, 24 Sept. 1992.

46. R. W. Boyd. “Nonlinear optics,” Academic Press, San Diego, second edition, 2003.

47. S. Russell. Report on waves. 14th Meeting of the British Association for the Advancement of Science, pages 311-390, 1844.

48. J. Z. Wilcox and T.J. Wilcox. “Stability of localized plasma model in two and three dimensions,” Physical Review Letters, 34:1160, 1975.

49. E. K. Zeise, E. Polturak, P. G. N. deVegvar and D. M. Lee. “Soliton propagation of zero sound in superuid 3he,” Physical Review Letters, 46:1588, 1981.

50. A. Hasegawa and F. Tappert. “Transmission of stationary nonlinear optical pulses in dispersive dielectric fibers,” Applied Physics Letters, 23:142, 1973.

51. Y. S. Kivshar and G. P. Agrawal. “Optical solitons,” Academic Press, USA, first edition, 2003.

52. M. Hercher. “Laser-induced damage in transparent media,” Journal of the Optical Society of America, 54:563, 1964.

53. R. Y Chiao, E. Garmire, and C. H Townes. “Self-Trapping of optical beams,” Physical Review Letters, 13(15):479 LP - 482, 1964.

54. V. E. Zakharov and A. B. Shabat. “An exact theory of two-dimensional self-focusing and of one-dimensional self-modulation of waves in nonlinear media,” Soviet Physics JETP, 34:62, 1972.

55. P. L. Kelley. “Self-focusing of optical beams,” Physical Review Letters, 15(26):1005 LP - 1008, 1965.

56. A. Barthelemy and C. Froehly, “Propagation soliton et auto-confinement de faisceaux laser par non linearite optique de kerr,” Optics Communications, 55(3):201-206, 1985.

57. J. S Aitchison, A. M Weiner, Y. Silberberg, M. K Oliver, J. L Jackel, D. E Leaird, E. M Vogel, and P. W.E Smith. “Observation of spatial optical solitons in a nonlinear glass waveguide,” Optics Letters, 15(9):471-473, 1990.

58. J. E. Bjorkholm and A. A. Ashkin. “cw self-focusing and self-trapping of light in sodium vapor,” Physical Review Letters, 32(4):129 LP - 132, 1974.

59. L. Poladian A.W. Snyder, D. J. Mitchell and F. Ladouceur. “Self-induced optical fibers: spatial solitary waves,” Optics Letters, 16(1):21-23, 1991.

60. P. Yeh, “Introduction to Photorefractive Nonlinear Optics,” Wiley, New York, 1993.

61. M. Segev, B. Crosignani, A. Yariv, and B. Fischer. “Spatial solitons in photorefractive media,” Physical Review Letters, 68(7):923-926, 1992.

62. G. C. Duree, J. L. Shultz, G. J. Salamo, M. Segev, A. Yariv, B. Crosignani, P. Di Porto, E. J. Sharp, and R. R. Neurgaonkar. “Observation of self-trapping of an optical beam due to the photorefractive effect,” Physical Review Letters, 71(4):533 LP - 536, 1993.

63. D. E. Pelinovsky, A. V. Buryak and Y. S. Kivshar, “Instability of Solitons Governed by Quadratic Nonlinearities,” Phys. Rev. Lett. 75 pp. 591, 1995.

64. W. E. Torruellas, Z. Wang, D. J. Hagan, E. W. Van Stryland, G. I. Stegeman, L. Torner and C. R. Menyuk, "Observation of two-dimensional Spatial Solitary Waves in a Quadratic Medium" Phys. Rev. Lett. 74 pp. 5036, 1995.

65. R. Schiek, Y. Baek and G. I. Stegeman, "One-Dimensional Spatial Solitary waves due to Cascaded Second-Order Nonlinearities in Planar Waveguides" Phys. Rev. E 53 pp. 1138, 1996.

66. C. Etrich, U. Peschel and F. Lederer, "Solitary Waves in Quadratically Nonlinear Resonators," Phys. Rev. Lett. 79 pp. 2454, 1997.

67. G. Leo, G. Assanto and W. E. Torruellas, "Beam pointing control with spatial solitary waves in quadratic nonlinear media," Opt. Commun. 134 pp. 223, 1997.

68. G. Leo, G. Assanto and W. E. Torruellas, "Bidimensional spatial solitary waves in quadratically nonlinear bulk media," J. Opt. Soc. Am. B 14 pp. 3134 1997.

69. M. Segev, "Optical spatial solitons," Optical and Quantum Electronics, 30:503-533, 1998.

70. G. I. Stegeman and M. Segev, "Optical spatial solitons and their interactions: Universality and diversity," Science, 286(5444):1518-1523, 1999.

71. M-F. Shih, M. Segev, and G. Salamo. "Three-dimensional spiraling of interacting spatial solitons," Physical Review Letters, 78(13):2551, 1997.

72. M-F. Shih, M. Segev, and G. Salamo. “Three-dimensional spiraling of interacting spatial solitons,” Physical Review Letters, 78(13):2551, 1997.

73. J. A. Armstrong, N. Bloembergen, J. Ducuing and P.S. Pershan, “Interactions between Light Waves in a Nonlinear Dielectric,” 1962. Phys. Rev. 127, 1918.

74. H. Ito, C. Takyu, and H. Inaba, “Fabrication of periodic domain grating in LiNbO3 by electron beam writing for application of nonlinear optical processes,” Electron. Lett., vol. 27, pp. 1221–1222, 1991.

75. A. Harada and Y. Nihei, “Bulk periodically poled MgO-LiNbO3 by corona discharge method,” Appl. Phys. Lett., vol. 69, no. 18, pp. 2629–2631, 1996.

76. M. Yamada, N. Nada, M. Saitoh, and K. Watanabe, “First-order quasi-phase matched LiNbO3 waveguide periodically poled by applying an external field for efficient blue second-harmonic generation,” Appl. Phys. Lett., vol. 62, no. 5, pp. 435–436, 1993.

77. K. Nakamura, J. Kurz, K. Parameswaran, and M. M. Fejer, “Periodic poling of magnesium-oxide-doped lithium niobate,” J. Appl. Phys., vol. 91, no. 7, pp. 4528–4534, 2002.

78. K. Kintaka, M. Fujimura, T. Suhara, and H. Nishihara, “High-efficiency LiNbO3 waveguide second-harmonic generation devices with ferroelectric-domain-inverted gratings fabricated by applying voltage,” J. Lightwave Technol., vol. 14, no. 3, pp. 462–468, 1996.

79. J. E. Geusie, H. J. Levenstein, S. Sigh, R.G. Smith, and L. G. Van Uitert, "Continuous 0.532-μ solid-state source using Ba2NaNb5O15," Appl. Phys. Lett., vol.12 no.9, pp.306-309, 1968.

80. R. G. Smith, "Theory of intracavity optical second harmonic generation," IEEE J. Quantum Electron., vol.6, no.4, pp. 215-130, Apr. 1970.

81. T. Miyoshi, S. Masui, T. Okada, T. Yanamoto, T. Kozaki, S. Nagahama, T.Mukai, "InGaN-based 518 and 488 nm laser diodes on *c*-plane GaN substrate," Physica Status Solidi (a), vol. 207, no. 6, pp. 1389–1392, June 2010.

82. Y. Lu, Q. Xu, Y. Gan, and CQ. Xu, "Field-Sequential Operation of Laser Diode Pumped Nd: YVO_4/PPMgLN Microchip Green Laser," IEEE Photon. Technol. Lett., vol. 22, no. 13, pp.990-992, July 2010.

83. J. Khaydarov, A. Shchegrov, S. Essaian, G. Nemet, S. Soghomonyan, M. Simonyan, H. Danielyan, and G. Gabrielyan, "High-efficiency green laser source for compact projectors," Proc. SID, San Antonio, June 2 - 5, paper 20.2, 2009.

84. M. H. Hu, H. K. Nguyen, K. Song, Y. Li, N. J. Visovsky, X. Liu, N. Nishiyama, S. Coleman, L. C. Hughes, J. Gollier, W. Miller, R. Bhat, and C.-E. Zah, "High-power high-modulation-speed 1060-nm DBR lasers for green-light emission," IEEE Photon. Technol. Lett., vol. 18, no. 4, pp. 616–618, Feb. 2006.

85. H. K. Nguyen, M. H. Hu, N. Nishiyama, N. J. Visovsky, Y. Li, K. Song, X. Liu, J. Gollier, L. C. Hughes, R. Bhat, and C.-E. Zah, "107-mW low-noise green-light emission by frequency doubling of a reliable 1060-nm DFB semiconductor laser diode," IEEE Photon. Technol. Lett., vol. 18, no. 5, pp. 682–684, Mar. 2006.

86. C.-E. Zah, Y. Li, R. Bhat, K. Song, N. visovsky, H. K. Nguyen, X. Liu, M. Hu, and N. Nishiyama, "High power 1060-nm raised-ridge strained single-quantum-well lasers," in IEEE Int. Semiconductor Laser Conf., Matsue, Japan, ThA3, pp. 39–40, Sep. 2004.

87. H. K. Nguyen, M. H. Hu, Y. Li, K. Song, N. J. Visovsky, S. Coleman, and C.-E. Zah, "304 mW green light emission by frequency doubling of a high-power 1060-nm DBR semiconductor laser diode," in Proc. of SPIE, vol. 6890, pp. 6890I, 2008.

88. M. H. Hu, H. K. Nguyen, K. Song, Y. Li, N. J. Visovsky, X. Liu, N. Nishiyama, S. Coleman, L. C. Hughes, J. Gollier, W. Miller, R. Bhat, and C.-E. Zah, "High-power distributed Bragg reflector lasers for green-light generation," in Proc. SPIE, vol. 6116, pp. 61160M, 2006.

89. U. Steegmuller, M. Kuhnelt, H. Unold, T. Schwarz, R. Schulz, K. Auen, C. Walter, and M. Schmitt, "Visible lasers for mobile projection," in Proc. SPIE, vol. 7001, pp. 70010D, 2008.

90. K. Ito, K. Kawamoto, and H. Momiji, “Theoretical study on intra-cavity distributed-Bragg-reflection quasi-phase-matched second-harmonic lasers,” Opt. Rev., vol. 2 no. 5, pp. 371–376, Sept. 1995.

91. Q-Y. Xu, Yi. Gan, Y. Lu, X. Li, and C-Q. Xu, “Theoretical Analysis of Intra-Cavity Second-Harmonic Generation of Semiconductor Lasers by a Periodically Poled Nonlinear Crystal Waveguide,” IEEE Journal of Quantum Electronics, vol. 47, issue 4, pp. 462-470, 04/2011.

92. Y. Lu, Q. Xu, Y. Gan, C. Xu, “Compact High Power Modulated Green Laser for Laser Display,” SID 2010, pp.1170-1172, 2010.

93. Y. Lu, Q. Xu, Y. Gan, C.Xu, “Over 500 mW Laser-Diode Pumped Green Laser Using Optical Contact Nd:YVO_4/Periodically Poled MgO:$LiNbO_3$ Crystal in Conference on Lasers and Electro-Optics, OSA Technical Digest (CD) (Optical Society of America, 2010), paper JTuD110.

94. T. Harimoto and J. Watanabe, “Efficient and stable 532 nm microchip laser pumped by single-longitudinal-mode laser-diode,” Electron. Lett., vol.41, no.12, pp.702-704. June 2005.

95. C. Jung, B.-A. Yu, I.-S. Kim, Y. L. Lee, N. E. Yu, and D.-K. Ko, "A linearly-polarized Nd:YVO_4/KTP microchip green laser," Opt. Exp., vol. 17, no.12, pp. 19611-19616, 2009.

96. C. Jung, B.-A. Yu, K. Lee, Y. L. Lee, N. E. Yu, D.-K. Ko, and J. Lee, “A compact diode-pumped microchip green light source with a built-in thermoelectric element,” Appl. Phys. Exp., vol. 1, pp. 062005, 2008.

97. B.-A. Yu, C. Jung, I.-S. Kim, Y. L. Lee, N. E. Yu, and D.-K. Ko, "Temperature-controlled efficient microchip green laser for mobile projection displays," Electron. Lett.,. vol. 45, no. 18, pp.943–945, 2009.

98. C. Q. Xu, et al, "MgO:PPLN frequency doubling optical chips for green light generation: from lab research to mass production", Photonics West 2012, paper 8280-4, 2012.

99. S. Trillo and W. Torruelas, "Spatial solitons," Springer, New York, 2001.

100. M. Mitchell and M. Segev, "Self-trapping of incoherent white light," Nature, 387:880-883, 1997.

101. K. Saravanamuttu, X. M Du, S. I Najafi, and M. P Andrews. "Photoinduced structural relaxation and densification in sol-gel-derived nanocomposite thin films: implications for integrated optics device fabrication," Canadian Journal of Chemistry-Revue Canadienne De Chimie, 76(11):1717-1729, 1998.

102. C. Decker, "The use of UV irradiation in polymerization," Polymer International, 45:133-141, 1998.

103. A. S. Kewitsch and A. Yariv, "Self-focusing and self-trapping of optical beams upon photopolymerization," Optics Letters, 21(1):24-26, 1996.

104. Tanya M Monro, L. Poladian, and C. Martijn de Sterke, "Analysis of self-written waveguides in photopolymers and photosensitive materials," Physical Review E, 57(1):1104-1113, 1998.

105. A. S. Kewitsch and A. Yariv, “Nonlinear optical properties of photoresists for projection lithography,” Applied Physics Letters, 68(4):455-457, 1996.

106. S. J. Frisken, “Light-induced optical waveguide uptapers,” Optics letters, 18(13):1035-1037, 1993.

107. K. Saravanamuttu and M. P. Andrews. “Visible laser self-focusing in hybrid glass planar waveguides,” Optics Letters, 27(15):1342-1344, 2002.

108. K. Dorkenoo, O. Cregut, L. Mager, F. Gillot, C. Carre, and A. Fort, “Quasisolitonic behavior of self-written waveguides created by photopolymerization,” Optics Letters, 27(20):1782-1784, 2002.

109. K. D Dorkenoo, F. Gillot, O. Cregut, Y. Sonnefraud, A. Fort, and H. Leblond, “Control of the refractive index in photopolymerizable materials for (2+1)D solitary wave guide formation,” Physical Review Letters, 93(14), 2004.

110. S. Shoji, S. Kawata, A. A. Sukhorukov, and Y. S. Kivshar, “Selfwritten waveguides in photopolymerizable resins,” Optics Letters, 27(3):185-187, 2002.

111. O. Sugihara, H. Tsuchie, H. Endo, N. Okamoto, T. Yamashita, M. Kagami, and T. Kaino, “Light-induced self-written polymeric optical waveguides for single-mode propagation and for optical interconnections,” Ieee Photonics Technology Letters, 16(3):804-806, 2004.

112. K. Yamashita, T. Hashimoto, K. Oe, K. Mune, R. Naitou, and A. Mochizuki, “Self-written waveguide structure in photosensitive polyimide resin

fabricated by exposure and thermosetting process," Ieee Photonics Technology Letters, 16(3):801-803, 2004.

113. T. Yamashita, M. Kagami, and H. Ito, "Waveguide shape control and loss properties of light-induced self-written (LISW) optical waveguides," Journal of Lightwave Technology, 20(8):1556-1562, 2002.
114. T. Yamashita, M. Kagami, and H. Ito, "Waveguide shape control and loss properties of light-induced self-written (LISW) optical waveguides," Journal of Lightwave Technology, 20(8):1556-1562, 2002.
115. M. Yonemura, A. Kawasaki, S. Kato, M. Kagami, and Y. Inui, "Polymer waveguide module for visible wavelength division multiplexing plastic optical fiber communication," Optics Letters, 30(17):2206-2208, 2005.
116. Y. Obata, M. Kanda, and O. Mikami, "Self-written waveguide on a VCSEL-emitting window using a photomask transfer method," Ieee Photonics Technology Letters, 18(9-12):1308-1310, 2006.
117. R. Bachelot, C. Ecoffet, D. Deloeil, P. Royer, and D. J Lougnot, "Integration of micrometer-sized polymer elements at the end of optical fibers by freeradical photopolymerization," Applied Optics, 40(32):5860-5871, 2001.
118. K. H. Jeong, J. Kim, and L. P. Lee, "Biologically inspired artificial compound eyes," Science, 312(5773):557-561, 2006.
119. http://www.fiberoptics4sale.com/wordpress/basic-optics-for-optical-fiber/

120. Tanya M Monro, C. Martijn de Sterke, and L. Poladian, "Investigation of waveguide growth in photosensitive germanosilicate glass," Journal of the Optical Society of America B: Optical Physics, 13(12):2824, 1996.
121. T. M Monro, C. M De Sterke, and L. Poladian, "Topical review - catching light in its own trap," Journal of Modern Optics, 48(2):191-238, 2001.
122. T. M Monro, P. D Miller, L. Poladian, and C. M de Sterke, "Self-similar evolution of self-written waveguides," Optics Letters, 23(4):268-270, 1998.
123. T. Okoshi, "Optical fibers," Academic Press, New York, 1982.
124. J.A. Buck, "Fundamentals of optical fibers," Wiley and Sons, 2004.
125. P. A. Belanger. optical fiber theory, "A supplement to applied electromagnetism," World Scientific Publishing Co. Pte. Ltd., 1993.
126. W. Wan, S. Jia, and J. W. Fleischer, "Dispersive supefluid-like shock waves in nonlinear optics," Nature, 3:46-51, 2007.
127. A. B Villafranca and K. Saravanamuttu, "An experimental study of the dynamics and temporal evolution of Self-Trapped laser beams in a photopolymerizable organosiloxane," Journal of Physical Chemistry C, 112(44):17388-17396, 2008.
128. J. Zhang, K. Kasala, A. Rewari, and K. Saravanamuttu, "Self-Trapping of spatially and temporally incoherent white light in a photochemical medium," Journal of the American Chemical Society, 128:406-407, 2006.

129. K. Kasala and K. Saravanamuttu, “An experimental study of the interactions of self-trapped white light beams in a photopolymer,” Applied Physics Letters, 93(5), 2008.

130. A. B Villafranca and K. Saravanamuttu, “Spontaneous and sequential transitions of a Gaussian beam into diffraction rings, single ring and circular array of filaments in a photopolymer,” Optics Express, Vol. 19 Issue 16, pp.15560-15573, 2011.